Investigation of Real-Time Optical Scanning Holography

by

Bradley Dean Duncan

Dissertation submitted to the Faculty of the

Virginia Polytechnic Institute and State University

in partial fulfillment of the requirements for the degree of

Doctor of Philosophy

in

Electrical Engineering

APPROVED:

Dr. Ting-Chung Poon, Chairman

Dr. Richard O. Claus

Dr. Guy J. Indebetouw

Dr. Ahmad Safaai-Jazi

Dr. Richard W. Conners

June 4, 1991

Blacksburg, Virginia

LD
5655
V856
1991
D863
c.2

Investigation of Real-Time Optical Scanning Holography

by

Bradley Dean Duncan

Dr. Ting-Chung Poon, Chairman

Electrical Engineering

(ABSTRACT)

Real-time holographic recording using an optical heterodyne scanning technique was proposed by Poon in 1985. The first part of this dissertation provides a detailed theoretical treatment of the technique, based on a Gaussian beam analysis. Topics to be addressed include the derivations of the optical transfer function (OTF) and impulse response of the scanning holographic recording system, reconstructed image resolution and magnification, methods of carrier frequency hologram generation and experimental verification of the recording technique based on careful measurements of a hologram corresponding to a simple transmissive slit. Furthermore, computer simulations are presented pertaining to the incoherent nature of the scanning holographic process and it is shown that this new technique can be used to reduce the effects of bias buildup common in conventional incoherent holographic methods.

The reconstruction of holograms generated by the heterodyne scanning technique is then considered in the second part of the dissertation. The primary concentration is on real-time reconstruction using an electron beam addressed spatial light modulator (EBSLM). For comparison, experimental coherent reconstruction methods are presented as well. Additional topics to be addressed are the spatial frequency limitations of the EBSLM and the derivation of the overall incoherent point spread function (PSF) for the holographic imaging (recording/reconstruction) system. Based upon the derived overall PSF, the reconstructed real image of a simple slit object is formulated, compared to, and shown to be consistent with experimental observations.

Acknowledgements

I would like to express my sincere gratitude to Dr. Ting-Chung Poon, my Ph.D. graduate advisor, for his dedicated guidance, assistance and patience while this dissertation was being prepared. Special thanks also to Dr. R.O. Claus for his lasting support of my graduate studies and research. Thanks also goes to Dr. Guy Indebetouw, Dr. Ahmad Safaai-Jazi and Dr. R.W. Conners for graciously serving on my Ph.D advisory committee.

Many thanks to my fellow graduate students at the Fiber & Electro-Optics Research Center, Virginia Tech, for their advice, consultation and lasting friendship. Thanks also to Bob Lineberry for his assistance in resolving many practical issues associated with my work, to Mrs. Marion Via for her selfless gift culminating in my being financially supported on a Bradley Department of Electrical Engineering Fellowship these past three years, and to Dr. Ming H. Wu (Hamamatsu Corporation, NJ), Mr. K. Shinoda and Dr. Y Suzuki (Hamamatsu Photonics K.K., Japan) for their valvable comments and discussions on the proper operation of the electron beam addressed spatial light modulator. And finally, sincere thanks to my parents for their unending support and encouragement, to Mrs. Shirley Raines for introducing me to the beauty of science, to Glenn C. Cooper and Fr. Richard Mooney for "showing me the light,"

to my grandfather, Roy Lane Proffitt, for just being a great guy (so long, pal), and to all my Blacksburg buddies for the many roof climbing fandangos at the House of Decadence!

This work was sponsored in part by the National Science Foundation through grant # ECS-8813115. Material support was also provided in the form of an equiptment loan (EBSLM, model X3636; EBSLM Controller, model C3637; and DVS-3010/SS electronic image processor) by Hamamatusu Corporation (New Jersey) and Hamamatsu Photonics K.K. (Japan).

Table of Contents

1.0 INTRODUCTION **1**

2.0 OPTICAL TRANSFER FUNCTION SYNTHESIS **5**

2.1 One-Pupil OTF Synthesis by Scanning 6

2.2 Equivalence Between Scanning and Incoherent Image Processing 8

2.3 In-Focus Two-Pupil OTF Synthesis by Acousto-Optics 11

2.4 Defocused Two-Pupil OTF Synthesis by Acousto-Optics 13

3.0 OPTICAL SCANNING HOLOGRAPHY **18**

3.1 Basic Concepts 18

3.1.1 Heterodyne scanning image processor 19

3.1.2 Fundamentals of optical scanning holography 20

3.1.3 Reconstruction of incoherent 3-D surfaces 25

3.1.4 Compatibility with real-time spatial light modulators 29

3.1.5 Heuristic description 30

3.2 Gaussian Beam Theory 31

3.2.1 Gaussian beam analysis 31

3.2.2 Scaling, magnification, resolution and distortion 38

3.2.3 Experimental verification 45

3.2.4 Bias reduction 48

4.0 RECONSTRUCTION OF SCANNED OPTICAL HOLOGRAMS 75

4.1 Principles of Real-Time Optical Scanning Holography 75

4.1.1 Electron beam addressed spatial light modulator 76

4.1.2 The overall point spread function 78

4.2 Size Of The Reconstructed Slit: Experimental Verification 85

5.0 CONCLUSION 101

5.1 Present Research Directions and Goals 103

5.2 Summary of Original Contributions 104

REFERENCES 105

Vita 108

List of Illustrations

Figure 1. One-pupil optical scanner [4]. 15

Figure 2. Conventional coherent optical image processing system. 16

Figure 3. Idealized acousto-optic heterodyne image processor [4]. 17

Figure 4. The optical scanning holography system 50

Figure 5. Construction of the composite scanning beam. 51

Figure 6. Holographic recording of a three dimensional object. 52

Figure 7. Point source hologram simulation. 53

Figure 8. Cross section of a point source hologram $(\omega_u = 3.526\mu m,\ f_{xo} = 0)$ 54

Figure 9. Cross section of a point source hologram $(\omega_u = 3.526\mu m,\ f_{xo} = 3.2\ mm^{-1})$ 55

Figure 10. Cross section of a point source hologram $(\omega_u = 40\mu m,\ f_{xo} = 0)$ 56

Figure 11. Cross section of a point source hologram $(\omega_u = 40\mu m,\ f_{xo} = 3.2\ mm^{-1})$ 57

Figure 12. Point source hologram width $(\omega_u << \omega_v)$ 58

Figure 13. Number of fringes in a point source hologram $(\omega_u << \omega_v)$ 59

Figure 14. Point source hologram width $(\omega_u \simeq \omega_v)$ 60

Figure 15. Number of fringes in a point source hologram $(\omega_u \simeq \omega_v)$ 61

Figure 16. Spatial carrier frequency 62

Figure 17. Relative OTF amplitude 63

Figure 18. Point source hologram reconstruction 64

Figure 19. Overlay of input and reconstructed objects 65

Figure 20. Lateral resolution 66
Figure 21. Longitudinal resolution (S=1) 67
Figure 22. Longitudinal resolution (S=5) 68
Figure 23. Longitudinal resolution (S=0.2) 69
Figure 24. Simulated hologram cross section of a 50 micrometer slit. 70
Figure 25. Simulated and experimentally measured hologram 71
Figure 26. Simulated hologram cross section of a 200 micrometer slit 72
Figure 27. Experimentally measured slit hologram cross sections 73
Figure 28. Simulated hologram cross section of a 200 micrometer slit 74
Figure 29. Schematic diagram of the EBSLM 93
Figure 30. Intermediate display technique 94
Figure 31. Point spread function of the holographic system 95
Figure 32. FWHM of the overall PSF 96
Figure 33. Hologram recorded for a 50 micrometer slit. 97
Figure 34. Lens configuration used in the reconstruction process 98
Figure 35. Simulation of the reconstructed slit image 99
Figure 36. Reconstructed real slit images 100

1.0 INTRODUCTION

Scanned holographic recordings of spatial information have traditionally been achieved only with long wavelength sources (such as in scanned acoustical holography [1], or as in standard microwave holography [2,3]). This is because detectors capable of measuring the amplitude oscillations of low frequency radiation are commonly available, allowing amplitude and phase information to be directly extracted from long wavelength signals. Recently, scanning techniques to generate optical holograms have also been proposed and studied [4,5].

In 1985, Poon [4] first proposed a technique by which holography by optical heterodyne scanning could be achieved as a direct application of a defocused incoherent image processing arrangement employing acousto-optic heterodyning and two-pupil optical transfer function (OTF) synthesis [6,7]. In this presentation, the original analysis is extended to include calculations based on Gaussian beam theory [5]. This is accompanied by detailed presentations of the scanning image processor, its associated OTF and the experiments performed to verify and evaluate the optical scanning holographic method.

Among the advantages/motivations of the optical scanning holographic technique is the potential capability of producing holograms of large scale objects without the need for large

optical elements. Another advantage is that holographic information recorded by the scanning technique manifests itself as a modulated electrical signal capable of being directly displayed on a device such as an intensity modulated oscilloscope or an electron beam addressed spatial light modulator (EBSLM) [4,5,8,9]. In fact, as has been previously reported [8,10], real-time recording and reconstruction of optically scanned holographic data can be achieved with the technique by using an EBSLM and coherent readout methods.

It is also interesting to note that though this technique of optical scanning holography is incoherent in nature, many shortcomings of previously described incoherent holographic techniques can be alleviated. In 1961, Mertz and Young pointed out that coherent illumination is not a necessary condition for the production of a hologram [11]. They showed that it was only necessary for each source point to produce a unique two-dimensional intensity pattern which encodes the position and intensity of the source. Throughout the late 1960's several methods of incoherent holography were proposed [12,13,14,15], though, by the early 1970's most research in the area had died out. This was likely due to several severe limitations inherent to incoherent holographic techniques of the time. Among the most serious limitations was the loss of fringe contrast in incoherent holograms of continuous objects through the rapid accumulation of background light [15]. Kozma and Massey [16], however, proposed a clever technique using a narrow band phase modulation in one arm of a modified Linnik interferometer to reduce this bias build-up by imposing a temporal carrier which separated the background light from the spatially varying fringe information. Other limitations were the difficulties of producing holograms of other than two dimensional objects (i.e., depth information was often severely distorted [15]) and the fact that it was often difficult to produce carrier frequency holograms except by indirect methods [17]. As will be shown in chapter three, however, the heterodyne optical scanning technique allows active and selective bias buildup reduction, thereby yielding increased fringe contrast. It will also be shown that the technique can be used to generate carrier frequency holograms of 3-D objects. It is felt that these advantages, combined with the possibilities for real-time holographic recording and

reconstruction [8,10] make the scanning heterodyne technique for optical holography quite attractive.

Before proceeding, it should be mentioned that in conventional (single-pupil) incoherent scanning or imaging systems, limitations exist on the potential image processing capabilities due to the resulting nonnegative intensity spread function [incoherent point spread function (PSF)], which in turn imposes severe constraints on both the amplitude and the phase of the optical transfer function (OTF) - essentially allowing only low-pass spatial filtering operations to be performed [18]. Such limitations are avoided by introducing a two-pupil system [6,19], as is done in the work described within, which allows flexibility in pupil-function specification for a desired synthesized PSF. As a result, any bipolar point spread function can be synthesized by using two-pupil methods, as long as the pupil functions can be arbitrarily specified and the interactive (bipolar) and noninteractive (unipolar) PSF terms can be separated on the basis of either spatial [20,21] or temporal [22,7] carriers. In addition, as we will see in chapter 3, when two-pupil processing systems are operated under defocused conditions [4,7], their applications include the production of optical holograms - a process clearly requiring that an input image be processed by a bipolar PSF.

It should also be mentioned that in the contexts of either real-time holography through the use of spatial light modulators or, possibly, the transmission of holographic data for television applications, the spatial resolution of holographic data presented on real-time display devices must be reduced. The problem of holographic information reduction has previously been addressed [23,24]. As will be evident later, the technique of optical heterodyne scanning holography suggests a practical method for reducing the information content to be recorded in holograms, somewhat reminiscent to the heterodyne scanning technique by Enlow [24].

To begin, chapter 2 provides a general review of one and two-pupil scanning image processing and discusses the equivalence between scanning and other incoherent image processing methods. The defocused two-pupil OTF used extensively in subsequent work is

then developed. In chapter 3 an introduction to optical scanning holography is provided, after which a detailed description of the OTF and impulse response of the heterodyne scanning holography system, formulated on the basis of interacting Gaussian beams is presented. This is followed by a discussion of the resolution and holographic magnification properties of the technique. Chapter 3 then ends with a description of experiments performed to verify the theoretical expectations of the scanning holographic recording technique, and some simulations which emphasize the bias reduction capabilities of the method. Chapter 4 subsequently provides additional details on the work performed on the real-time reconstruction of scanned holographic images using an EBSLM, and a comparison is made for a slit object reconstructed by both real-time and coherent methods. To conclude, chapter 5 provides a summary of relevant achievements and results as well as a discussion of present research directions and goals.

2.0 OPTICAL TRANSFER FUNCTION SYNTHESIS

In this chapter the defocused optical transfer function (OTF) for the two-pupil scanning image processor used in optical scanning holography is developed according to reference [4]. As detailed analyses leading to the results of this chapter are presented in reference [4], only the general framework leading to the results relevant to the optical scanning holography technique will be presented here.

To begin, the OTF for a single pupil scanning image processor is developed. The equivalence between the scanning image processor and an incoherent imaging system is then shown. Next, the in-focus two-pupil OTF for a scanning system employing acousto-optic Bragg diffraction is developed, and subsequently the chapter concludes by extending this analysis to the defocused case.

2.1 One-Pupil OTF Synthesis by Scanning

Refering to the system of Figure 1, where coherent illumination is assumed, we see that lens ℓ_1 forms, in plane 1, the Fourier transform U_1' of the optical field U_0. A beam shaping transparency Γ_1 then multiplies U_1' to create the pupil function U_1, and lens ℓ_2 forms the Fourier transform U_2 of U_1 in plane 2. Subsequently, the field U_2 is used to scan the transparency Γ_2. The photodiode (PD), which responds to the intensity of the incident optical wave, then accepts the entire field $\Gamma_2 U_2$ and generates a DC signal, written here in voltage form as

$$V(x,y) = \int_{-\infty}^{\infty}\int_{-\infty}^{\infty} |\Gamma_2(x_2, y_2)|^2 \, |U_2(x_2 - x, y_2 - y)|^2 \, dx_2 \, dy_2 \quad , \tag{2.1.1}$$

where the (x_2, y_2) coordinate system is defined in Figure 1 and x and y are delay variables introduced by scanning U_2 about Γ_2.

Equation (2.1.1) is readily recognized as the correlation of the two functions $|\Gamma_2|^2$ and $|U_2|^2$ [25]. By taking the Fourier transform of equation (2.1.1), the result

$$\mathcal{F}\{V(x,y)\} = \mathcal{F}\left\{|\Gamma_2|^2\right\} \mathcal{F}^*\left\{|U_2|^2\right\} \tag{2.1.2}$$

is obtained, where $*$ denotes the complex conjugate, $\mathcal{F}$ denotes the Fourier transform operation given as

$$\mathcal{F}\{g(x,y)\} = \int_{-\infty}^{\infty}\int_{-\infty}^{\infty} g(x,y) \, exp(-j\,2\pi\,(f_x\,x + f_y\,y)) \, dx\,dy \quad , \tag{2.1.3}$$

and where f_x and f_y denote the spatial frequencies. The OTF of the scanning system is then simply defined as

$$OTF(f_x, f_y) = \frac{\mathcal{F}\{V(x,y)\}}{\mathcal{F}\left\{|\Gamma_2|^2\right\}} = \mathcal{F}^*\left\{|U_2|^2\right\} = \mathcal{F}^*\left\{U_2^* U_2\right\} \quad , \tag{2.1.4}$$

or

$$OTF(f_x, f_y) = \mathcal{F}^*\left\{|\mathcal{F}\{U_1\}|^2\right\} \quad , \tag{2.1.5}$$

where

$$\mathcal{F}\{U_1(x_1, y_1)\} = U_2\left(\frac{x_2}{\lambda f_2}, \frac{y_2}{\lambda f_2}\right) \tag{2.1.6}$$

and λ is the source wavelength [25]. One then finds, after performing the necessary simplifications [4], that

$$\begin{aligned} OTF(f_x, f_y) &= \int_{-\infty}^{\infty}\int_{-\infty}^{\infty} U_1(x_1, y_1)\, U_1^*(x_1 - \lambda f_2 f_x, y - \lambda f_2 f_y)\, dx_1\, dy_1 \\ &= U_1 \circledast U_1 \end{aligned} \quad , \tag{2.1.7}$$

where $\circledast$ denotes a correlation. We thus see that the OTF of the single pupil scanning system is the autocorrelation of the pupil function of the scanning field. Equation (2.1.7) is, of course, well known; it is presented here only to establish the context for the acousto-optic scanning system to be discussed later.

2.2 Equivalence Between Scanning and Incoherent Image Processing

For a conventional coherent optical system, as shown in Figure 2, the complex field in the image plane $U_i(x_i, y_i)$ is found by convolving the field in the object plane $U_o(x_o, y_o)$ with the impulse response $h(x_i, y_i\,;\, x_o, y_o)$, or the coherent point spread function (PSF). For a spatially invariant system, we have

$$\begin{aligned} U_i(x_i, y_i) &= \int_{-\infty}^{\infty}\int_{-\infty}^{\infty} U_o(x_o, y_o)\, h(x_i - x_o, y_i - y_o)\, dx_o\, dy_o \\ &= U_o * h \end{aligned} \quad , \tag{2.2.1}$$

where h is the complex amplitude at image coordinates (x_i, y_i) in response to a point source object at (x_o, y_o) and $*$ denotes the convolution operation.

Fourier transforming equation (2.2.1), we have

$$\mathcal{F}\{U_i\} = \mathcal{F}\{U_o\}\,\mathcal{F}\{h\} \quad . \tag{2.2.2}$$

The coherent transfer function of the imaging system is defined then, under properly focused conditions, as

$$H(k_x, k_y) = \frac{\mathcal{F}\{U_i\}}{\mathcal{F}\{U_o\}} = \mathcal{F}\{h\} \quad . \tag{2.2.3}$$

However, since

$$h(x,y) = \mathcal{F}\{p(x,y)\}\Big|_{k_{x,y} = -\frac{2\pi}{\lambda f}x,y} = P\left(-\frac{2\pi}{\lambda f}x\,,\, -\frac{2\pi}{\lambda f}y\right) \quad , \tag{2.2.4}$$

where p(x,y) is the pupil function of the imaging system, $\mathcal{F}\{p(x,y)\} = P(k_x, k_y)$ and $k_{x,y} = 2\pi f_{x,y}$, equation (2.2.3) becomes [25]

$$H(k_x, k_y) = p\left(\frac{\lambda f}{2\pi} k_x, \frac{\lambda f}{2\pi} k_y\right) \quad . \tag{2.2.5}$$

Notice that $H(k_x, k_y)$, which is specified according to the pupil function p(x,y), characterizes the performance of the coherent imaging system.

For the case of a spatially incoherent source illuminating the system of Figure 2, the image intensity is given as

$$\mathrm{I}_i(x_i, y_i) = \int_{-\infty}^{\infty}\int_{-\infty}^{\infty} \mathrm{I}_o(x_o, y_o)\,|h(x_i - x_o,\ y_i - y_o)|^2\, dx_o\, dy_o \quad , \tag{2.2.6}$$

where $|h|^2$ is the unipolar (i.e., positive and real) intensity PSF [25]. Expressing equation (2.2.6) in the frequency domain yields

$$\mathcal{F}\{\mathrm{I}_i\} = \mathcal{F}\{\mathrm{I}_o\}\mathcal{F}\left\{|h|^2\right\} \quad . \tag{2.2.7}$$

The optical transfer function (OTF) of the incoherent imaging system is then defined as

$$OTF = \frac{\mathcal{F}\{\mathrm{I}_i\}}{\mathcal{F}\{\mathrm{I}_o\}} = \mathcal{F}\left\{|h|^2\right\} \quad . \tag{2.2.8}$$

Using equations (2.1.3), (2.2.3) and the inverse Fourier transform, defined as

$$\mathcal{F}^{-1}\{G(k_x, k_y)\} = \int_{-\infty}^{\infty}\int_{-\infty}^{\infty} G(k_x, k_y)\ \exp(+j(k_x x + k_y y))\, dk_x\, dk_y \quad , \tag{2.2.9}$$

where $k_x = 2\pi f_x$ and $k_y = 2\pi f_y$, we find from equation (2.2.8) that

$$
\begin{aligned}
OTF &= \iint h\, h^{*} \exp(-j(k_x x + k_y y))\, dx\, dy \\
&= \iiiint\!\!\iint H(k_x', k_y')\, H^{*}(k_x'', k_y'') \exp(j(k_x' x + k_y' y)) \\
&\qquad \times \exp(-j(k_x'' x + k_y'' y)) \exp(-j(k_x x + k_y y)) \\
&\qquad \times dk_x'\, dk_y'\, dk_x''\, dk_x''\, dx\, dy \qquad (2.2.10) \\
&= \iiiint H(k_x', k_y')\, H^{*}(k_x'', k_y'')\, \delta(k_x' - k_x'' - k_x)\, \delta(k_y' - k_y'' - k_y) \\
&\qquad \times dk_x'\, dk_y'\, dk_x''\, dk_y'' \\
&= \iint H(k_x', k_y')\, H^{*}(k_x' - k_x, k_y' - k_y)\, dk_x'\, dk_y' \quad .
\end{aligned}
$$

Expressing the OTF in terms of the pupil function p(x,y), we have

$$
\begin{aligned}
OTF(f_x, f_y) &= \iint p\left(\frac{\lambda f}{2\pi} k_x', \frac{\lambda f}{2\pi} k_y'\right) p^{*}\left[\frac{\lambda f}{2\pi}(k_x' - k_x), \frac{\lambda f}{2\pi}(k_y' - k_y)\right] \\
&\qquad \times d\left(\frac{\lambda f}{2\pi} k_x'\right) d\left(\frac{\lambda f}{2\pi} k_y'\right) \quad , \qquad (2.2.11) \\
&= \iint p(x', y')\, p^{*}(x' - \lambda f f_x, y' - \lambda f f_y)\, dx' dy' \\
&= p \circledast p
\end{aligned}
$$

where the limits of integration of all integrals in the last two equations are from $-\infty$ to ∞ and where nonessential constants have been left out of the derivation. We thus see that for incoherent imaging systems, the OTF is simply the autocorrelation of the system pupil function. By then comparing equations (2.2.11) and (2.1.7) the equivalence between scanning and incoherent imaging systems is established. Again, there is no novelty in deriving this equivalence. Its derivation does, however, aid in understanding the material to follow. Also, notice that due to the autocorrelation operation, the OTF of equation (2.2.11) is low-pass in nature, indicating the processing limitations of one-pupil scanning systems discussed in chapter 1.

2.3 In-Focus Two-Pupil OTF Synthesis by Acousto-Optics

A simple two-pupil scanning image processing technique exhibiting both spatial and temporal frequency offsets brought about by acousto-optic Bragg diffraction is shown schematically in Figure 3 [4]. As seen, a laser directs a beam of light onto an acousto-optic modulator (AOM) - a device which in essence creates two identical light beams differing in temporal frequency by $\Delta\nu$ and in propagation angle by $\alpha \simeq (\lambda/V_s)\Delta\nu$, V_s being the velocity of sound in the AOM. Next, lens ℓ_1 forms, in its back focal plane, the Fourier transforms U_1', V_1' of the fields U_0, V_0 exiting the AOM. A beam shaping transparency Γ_1 then acts on U_1' and V_1' to create U_1, V_1, after which a second lens ℓ_2 forms the Fourier transforms U_2, V_2 in its back focal plane. The total field $U_2 + V_2$ is then used to scan the transparency Γ_2. In contrast to the one pupil scanning technique discussed in the preceding sections, in which the photodiode (PD), and associated electronics, delivered a DC signal, the PD now delivers a heterodyne signal at the beat frequency $\Delta\nu$ of the two fields U_2 and V_2. This signal is given in voltage form by

$$v(x,y,t) = \int_{-\infty}^{\infty}\int_{-\infty}^{\infty} \left| \left[V_2(x_2 - x, y_2 - y) + U_2(x_2 - x, y_2 - y) \exp(-j\,2\pi\,\Delta\nu\,t) \right] \times \Gamma_2(x_2, y_2) \right|^2 dx_2\,dy_2 \quad , \quad (2.3.1)$$

where the time varying part of equation (2.3.1) containing the pupil interaction information is expressed simply as

$$\tilde{v}(x,y,t) = Re\left[\int_{-\infty}^{\infty}\int_{-\infty}^{\infty} U_2(x_2 - x, y_2 - y)\, V_2^{*}(x_2 - x, y_2 - y) \times |\Gamma_2(x_2, y_2)|^2\, dx_2\,dy_2 \times \exp(-j\,2\pi\,\Delta\nu\,t) \right] \quad , \quad (2.3.2)$$

with an nonessential constant left out.

In terms of a phasor $\tilde{V}(x,y)$, such that

$$\tilde{v}(x,y,t) = Re\left[\tilde{V}(x,y)\exp(-j\,2\pi\,\Delta\nu\,t)\right] \quad , \tag{2.3.3}$$

we find from equation (2.3.2) that

$$\tilde{V}(x,y) = \int_{-\infty}^{\infty}\int_{-\infty}^{\infty} U_2(x_2-x,\,y_2-x)\,V_2^{*}(x_2-x,\,y_2-y)\,|\Gamma_2(x_2,\,y_2)|^2\,dx_2\,dy_2 \quad . \tag{2.3.4}$$

The phase and amplitude of the photodiode signal, as a function of x and y, constitute the scanned and processed version of the transparency Γ_2. From the analysis of the one-pupil scanning OTF synthesis (i.e., from equation 2.1.1 - 2.1.5) we can immediately write down the OTF of the two-pupil system as [4]

$$\begin{aligned} OTF &= \frac{\mathcal{F}\{\tilde{V}(x,y)\}}{\mathcal{F}\{|\Gamma_2|^2\}} = \mathcal{F}^{*}\left\{U_2^{*}\,V_2\right\} \\ &= U_1 \circledast V_1 \end{aligned} \quad , \tag{2.3.5}$$

by which is meant

$$OTF = \int_{-\infty}^{\infty}\int_{-\infty}^{\infty} U_1(x_1,y_1)\,V_1^{*}(x_1-\lambda\,f_2\,f_x\,,\,y_1-\lambda\,f_2\,f_y)\,dx_1\,dy_1 \quad . \tag{2.3.6}$$

We thus see that the OTF of the two-pupil system is the cross correlation of the pupil functions U_1 and V_1, and that the two-pupil system is incoherent in the sense that its operation is described by the same general formalism leading to equation 2.2.11, even though the system uses coherent light and its output (a heterodyne current readily separated from the

noninteraction DC terms of equation (2.3.1) through electronic bandpass filtering centered at $\Delta\nu$) is characterized by the amplitude and phase (i.e., the OTF is not necessarily low-pass, thus allowing bipolar PSFs) - a characteristic generally indicative of coherent optical systems. We now extend the result of equation (2.3.5) to the more general defocused case.

2.4 Defocused Two-Pupil OTF Synthesis by Acousto-Optics

Refering to Figure 3, Γ_2 is now placed in an out-of-focus plane, plane 2′, a distance z from the in-focus plane, plane 2. Following the procedure leading to equation (2.3.5) we have

$$OTF = \frac{\mathcal{F}\left\{\tilde{V}(x,y;z)\right\}}{\mathcal{F}\left\{|\Gamma_2|^2\right\}} = \mathcal{F}^*\left\{U_2'^*(x_2', y_2')\, V_2'(x_2', y_2')\right\} \quad , \tag{2.4.1}$$

where U_2' and V_2' are obtained through the Fresnel diffraction of U_2 and V_2, respectively, and U_2 and V_2 are related to U_1 and V_1, respectively, through the action of lens ℓ_2. The explicit relations are [25]

$$U_2(x_2, y_2) = \int_{-\infty}^{\infty}\int_{-\infty}^{\infty} U_1(x,y) \exp\left[-j\frac{2\pi}{\lambda f_2}(x_1x_2 + y_1y_2)\right] dx_1\, dy_1 \quad , \tag{2.4.2}$$

and

$$U_2'(x_2', y_2') = \exp\left(j\frac{k}{2z}(x_2'^2 + y_2'^2)\right)$$
$$\times \int_{-\infty}^{\infty}\int_{-\infty}^{\infty} U_2(x_2, y_2)\exp\left[j\frac{k}{2z}(x_2^2 + y_2^2)\right] \quad , \qquad (2.4.3)$$
$$\times \exp\left[-j\frac{k}{z}(x_2x_2' + y_2y_2')\right] dx_2\, dy_2$$

where $k = 2\pi/\lambda$, f_2 is the focal length of lens ℓ_2 and identical expressions exist for V_2 and V_2'.

Using equations (2.4.2), (2.4.3) and the similar expressions for V_2 and V_2' in equation (2.4.1) it has been shown [4] that the defocused OTF is

$$OTF(f_x, f_y; z) = \exp\left[j\pi\lambda z(f_x^2 + f_y^2)\right]$$
$$\times \int_{-\infty}^{\infty}\int_{-\infty}^{\infty} U_1(x_1, y_1)\, V_1^*(x_1 - \lambda f_2 f_x, y_1 - \lambda f_2 f_y) \quad . \qquad (2.4.4)$$
$$\times \exp\left[-j\frac{2\pi z}{f_2}(x_1 f_x + y_1 f_y)\right] dx_1\, dy_1$$

In the next chapter we will see how the two-pupil scanning image processor, described by the OTF of equation (2.4.4) can be used in holographic applications.

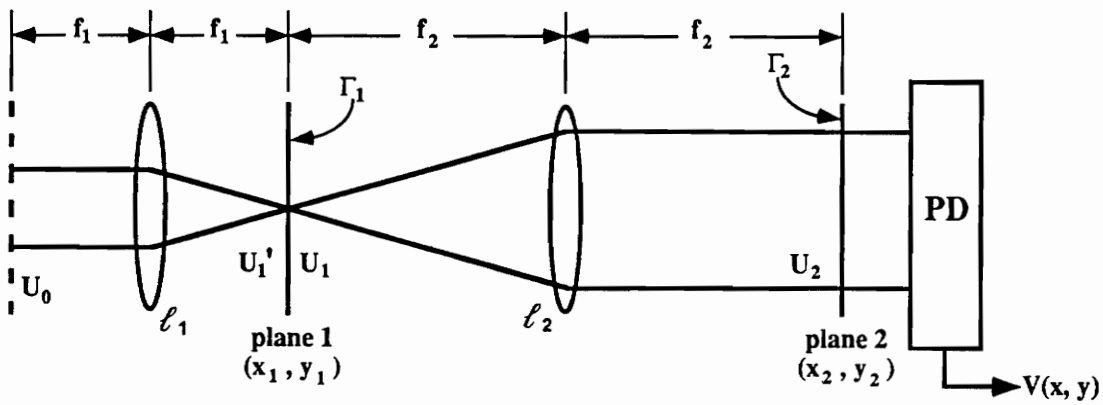

Figure 1. One-pupil optical scanner [4].

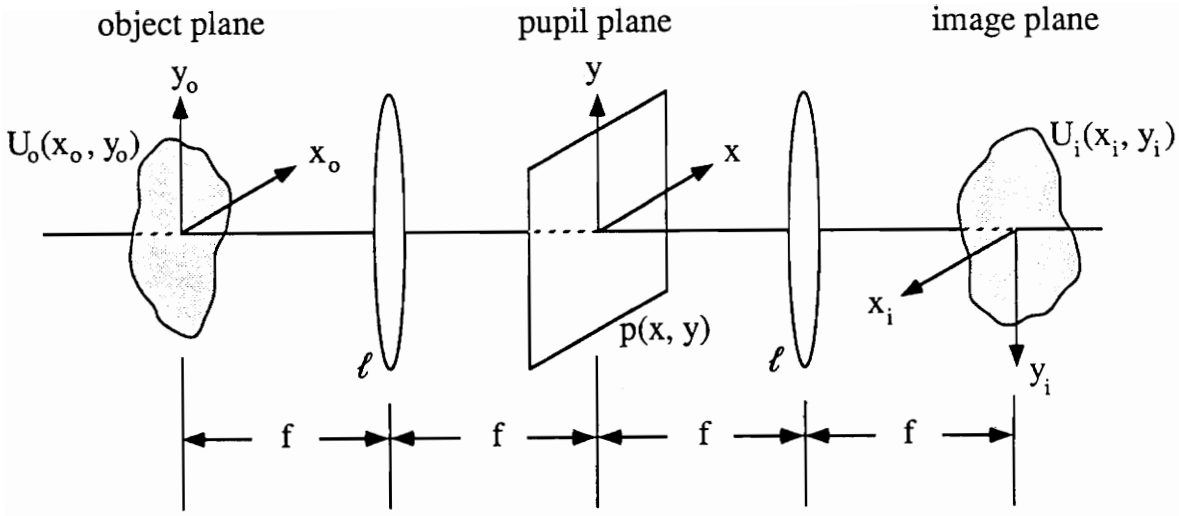

Figure 2. Conventional coherent optical image processing system.

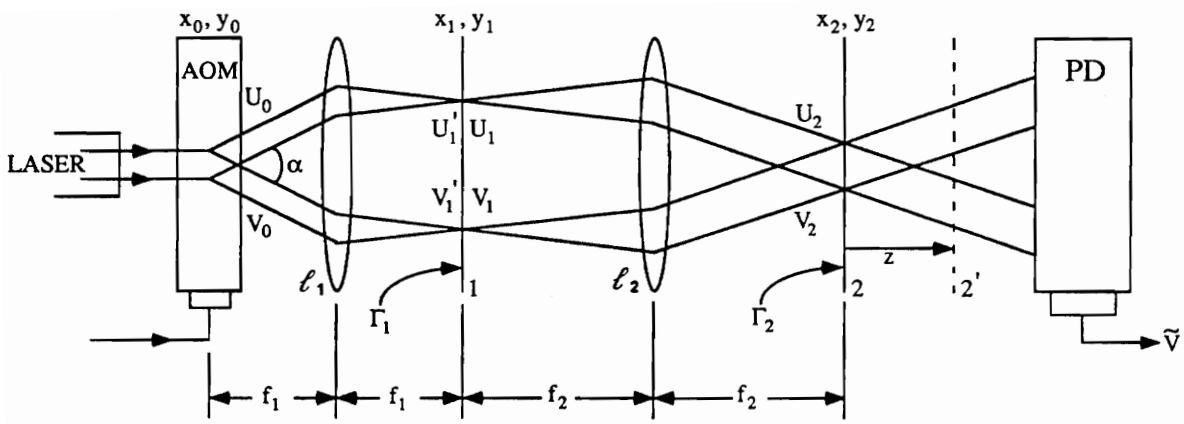

Figure 3. Idealized acousto-optic heterodyne image processor [4].

3.0 OPTICAL SCANNING HOLOGRAPHY

In this chapter the basic concepts involved in optical scanning holography are presented, along with an analysis of the technique based on a Gaussian beam interaction approach.

3.1 Basic Concepts

This section begins with a presentation of the heterodyne scanning image processor used in the experimental work to be described later. Provided next is a description of how this image processor can be used for generating optical holograms. The reconstruction of 3-D surfaces and the compatibility of the image processor with real-time spatial light modulators is then discussed, and finally, section 3.1 concludes with a simple heuristic description of the general principles involved in optical scanning holography.

3.1.1 Heterodyne scanning image processor

The experimentally implemented OTF synthesis system based on the acousto-optic two-pupil approach is shown schematically within the shaded lines of Figure 4, where the notation (including subscripts) describing the various lenses, pupil functions, etc., has been chosen to allow direct cross referencing between the material in this chapter and that of chapter 2.

From Figure 4 we see that the Fourier transforms of the pupil functions U_1 and V_1 are superposed on the mirror of an x-y scanning device. Notice that the contribution due to pupil U_1 is upshifted in temporal frequency according to the operating frequency f_c (in our case, $f_c = 40\,MHz$) of the indicated acousto-optic modulator (AOM) and that pupil U_1, in general, can be subject to intraplanar translation, with respect to V_1, by a distance d. After propagating a distance z, the Fresnel diffraction pattern of this composite beam is used to scan the object amplitude transparency Γ_2. Lens ℓ_i then images Γ_2 onto a PIN photodiode such that after scanning all light passing through Γ_2 is collected and converted to a corresponding scanned electrical signal. Subsequent bandpass filtering centered at f_c yields a processed signal of the form

$$\tilde{v}(x,y,z,t) = Re\left\{\tilde{V}(x,y;z)\ \exp(-j2\pi f_c t)\right\} \quad , \tag{3.1.1}$$

where $\tilde{V}$ is the voltage phasor at the output of the radio-frequency (RF) amplifier and it is assumed that the bandpass filter passes the entire signal spectrum imposed on the carrier without distortion. Note that in equation (3.1.1), x and y are in general functions of time determined by the scanner's motion.

As shown in section 2.4, the spectrum of the voltage signal produced by the photodiode and its associated circuitry is related to the spectrum of the object intensity $|\Gamma_2|^2$ by

$$F\{\tilde{V}(x,y;z)\} = OTF \times F\{|\Gamma_2|^2\} \quad , \tag{3.1.2}$$

where OTF is the defocused optical transfer function of the incoherent processing system and the explicit form of the OTF is

$$OTF(f_x, f_y;z) = \exp\left(j\pi\lambda z(f_x^2 + f_y^2)\right)\int_{-\infty}^{\infty}\int_{-\infty}^{\infty} U_1(x-d, y)\, V_1^*(x-\lambda f_2 f_x,\ y-\lambda f_2 f_y) \times \exp\left(-j\frac{2\pi z}{f_2}(xf_x + yf_y)\right) dxdy \quad , \tag{3.1.3}$$

where $*$ indicates the complex conjugate, f_2 is the focal length of the lens ℓ_2, d is the intraplanar translation of pupil U_1 (with respect to pupil V_1), λ is the wavelength of the laser source and z is the depth parameter which equals the distance from the scanning mirror to Γ_2. Note that equation (3.1.3) is identical to equation (2.4.4), except that the intraplanar translation of the pupil function U_1 is made explicit in equation (3.1.3). Also note that incoherent bandpass spatial filtering based on this approach has been demonstrated [26] and that a similar system has also been used recently for applications in textural edge extraction [27].

3.1.2 Fundamentals of optical scanning holography

The system of Figure 4 can be used in holographic recording applications because the amplitude and phase of $\tilde{v}(x,y,z,t)$ can be preserved [8] by either homodyning or heterodyning the scanned electrical signal $\tilde{v}$ at the output of the RF amplifier. In Figure 4 the heterodyne detection scheme is employed, where the scanned signal is mixed with a sinusoid of frequency $f_o + f_c$. The mixed signal, after bandpass filtering at f_o, is then amplified and added

to a DC bias voltage to give an output signal from the entire system. Using equations (3.1.1) and (3.1.2) the form of this signal is

$$v(x,y,z,t) = V_{DC} + Re\left\{F^{-1}\left[OTF \times F\left\{|\Gamma_2|^2\right\}\right] \exp(-j2\pi f_o t)\right\} \quad , \tag{3.1.4}$$

where the DC bias is needed to preserve the phase of the AC signal. The total signal can now be fed into the intensity modulating input of a two dimensional display device, whose electron gun (for example, in the case of an electron beam addressed spatial light modulator (EBSLM) [9]) is synchronized with the x and y scanning frequencies of the scanner. If we assume that scanning takes place in a raster fashion such that f_x, the x-scanning frequency, is much greater than f_y, the y-scanning frequency, while also assuming that f_o is an integer multiple of f_x, then the temporal carrier frequency f_o $[s^{-1}]$ directly translates to a spatial carrier frequency f_o/v_x $[m^{-1}]$, where v_x is the electron gun velocity of the display device in the x direction. Equation (3.1.4) can now be written in the form of a two dimensionally displayed signal as

$$v(x,y;z) = V_{DC} + Re\left\{F^{-1}\left[OTF \times F\left\{|\Gamma_2|^2\right\}\right] \exp\left(-j2\pi \frac{f_o}{v_x} x\right)\right\} \quad , \tag{3.1.5}$$

where the temporal carrier frequency f_o in equation (3.1.4) has been translated to a spatial carrier frequency f_o/v_x, with v_x denoting the electron gun velocity of the display device in the x direction. Note that as written, equation (3.1.5) is a general description, for planar objects $|\Gamma_2|^2$ located a distance z from the scanning mirror, of the output of the scanning image processor shown in Figure 4 (3-D objects will be discussed later). By judicious selection of the pupil functions U_1 and V_1, one can synthesize desired OTFs. The discussions here, however, will be restricted to the values of U_1 and V_1 which will result in equation (3.1.5) reducing to a form representing the holographic recording of $|\Gamma_2|^2$. (Recall that in incoherent holography the intensity distribution of the input object $|\Gamma_2|^2$ is recorded rather than the amplitude distribution Γ_2, as would be the case in coherent holography. This should pose no conceptual

difficulty when one realizes that all objects seen by the human eye, for example, are seen as intensity objects; i.e., the human eye is a square law detection device.)

To show that equation (3.1.5) can indeed be used to represent holographic information, consider the case when $U_1 = \delta(x, y)$ and $V_1 = 1$. This situation is shown in Figure 5. We will see that this choice of U_1 and V_1 results in a complex Fresnel zone plate (FZP) impulse response for the heterodyne scanning system. Recall that a FZP is the hologram of a point source. One can then imagine that it is through the action of scanning that this impulse response is convolved with a general object $|\Gamma_2|^2$ such that the hologram of $|\Gamma_2|^2$ is generated.

Through the direct application of equation (3.1.3) we see that the OTF when $U_1 = \delta(x,y)$ and $V_1 = 1$ is

$$OTF(f_x, f_y;z) = \exp\left(j\pi\lambda z(f_x^2 + f_y^2)\right) \exp\left(-j\frac{2\pi zd}{f_2} f_x\right) \quad . \tag{3.1.6}$$

Completing the square and combining terms yields

$$OTF(f_x, f_y;z) = \exp\left(-j\frac{z\pi}{\lambda}\left(\frac{d}{f_2}\right)^2\right) \exp\left(j\frac{z}{2k}\left[\left(K_x - \frac{kd}{f_2}\right)^2 + K_y^2\right]\right) \quad , \tag{3.1.7}$$

where $K_{x,y} = 2\pi f_{x,y}$, $k = 2\pi/\lambda$ and we see that the translation of U_1 by d has introduced a spatial carrier offset in the OTF of an amount $f_{xo} = d/\lambda f_2$. This is easily visualized in Figure 5 where the Fourier transform of the displaced point source results in a plane wave with a constant spatial frequency offset of $f_{xo} = (k/2\pi)\sin(\theta) \simeq d/\lambda f_2$, in the paraxial approximation.

The impulse response of the system $\tilde{V}_\delta$ is found by inverse Fourier transforming equation (3.1.7). Upon performing the inverse Fourier transform operation we find that

$$\tilde{V}_\delta(x,y;z) = \frac{\exp\left(j\frac{\pi}{2}\right)}{\lambda z} \exp\left(-j\frac{\pi}{\lambda z}\left\{\left[x - d\frac{z}{f_2}\right]^2 + y^2\right\}\right) \quad , \tag{3.1.8}$$

where $\tilde{V}_\delta(x,y;z)$ is recognized as a complex chirp-type impulse response, or complex FZP. To more fully investigate this result we let $|\Gamma_2|^2 = \delta(x,y)$ and use the impulse response of equation (3.1.8) to evaluate equation (3.1.5). We anticipate that this will result in the generation of a real FZP which is characteristic of point source holograms. With $|\Gamma_2|^2 = \delta(x,y)$ equation (3.1.5) then becomes

$$v(x,y;z) = V_{DC} + Re\left\{\tilde{V}_\delta \, exp\left(-j2\pi \frac{f_o}{v_x} x\right)\right\} \quad . \tag{3.1.9}$$

It is evident from equations (3.1.7) and (3.1.9) that due to the low frequency temporal carrier f_o and the intraplanar translation d, the total effective spatial frequency carrier becomes

$$f_{xo} = \frac{d}{\lambda f_2} - \frac{f_o}{v_x} \quad . \tag{3.1.10}$$

We thus see that spatial frequency carriers associated with the signal v(x,y;z) can be introduced by either providing a low frequency temporal carrier through electronic mixing or by displacing pupil U_1 with respect to V_1 by an amount d.

Continuing with our calculations, we insert equation (3.1.8) into equation (3.1.9) and perform the appropriate simplifications to yield the displayed signal corresponding to the result of scanning a point object. When U_1 and V_1 are chosen as previously described, the result is

$$v(x,y;z) = C_1 + C_2 \cos\left(\frac{\pi}{\lambda z}\left\{(x - x_o)^2 + y^2\right\} - \phi\right) \quad , \tag{3.1.11}$$

where

$$
\begin{aligned}
C_1 &= V_{DC} \\
C_2 &= \frac{A}{\lambda z} \\
x_o &= \frac{zd}{f_2} - \lambda z \frac{f_o}{v_x} \\
\phi &= \phi_{uv} + \frac{\pi}{2} + \pi\lambda z\left(\frac{f_o}{v_x}\right)^2\left[1 - 2\left(\frac{zd}{f_2}\right)\left(\frac{v_x}{f_o}\right)\right] \quad ,
\end{aligned}
\tag{3.1.12}
$$

and where a possible relative phase difference ϕ_{uv} between pupils U_1 and V_1 has been introduced. The constant A will account for the intensities of the light passing through the pupils. We see that equation (3.1.11) is a real off-axis Fresnel zone plate (FZP), characteristic to an off-axis point source hologram, where z is the depth information of the point source and x_o is the spatial offset of the FZP [28,29]. Physical insight to these parameters can be gained by once again referring to Figure 5 and assuming that $|\Gamma_2|^2 = \delta(x,y)$. We see that the depth information z is the distance from the scanner to the point source. We also see that the center of the interference pattern at the object plane is located at $x = -zd/f_2$. Considering now that $f_o = 0$, (i.e., homodyne detection) and that $|\Gamma_2|^2$ is being scanned in the $+x$ direction, it is seen that the light passing through $|\Gamma_2|^2 = \delta(x,y)$ will not correspond to the center of the interference pattern until $x = +zd/f_2$, as expected from equation (3.1.11) when $f_o = 0$ and $x_o = zd/f_2$.

The next parameter for consideration in equation (3.1.11) is the phase term ϕ. This term is constant for a given source point and only influences the phase of that point upon holographic reconstruction. As our eyes would not be able to detect this phase information upon viewing the reconstructed image, the phase term ϕ is essentially irrelevant. However, as will be seen later, ϕ influences the holographic fringe structure.

The last interesting term of equation (3.1.11) is the bias level C_1. The requirement on this value is that it must be large enough such that $v(x,y;z) \geq 0$ for all x, y and z. By adjusting C_1 so that $v(x,y;z)_{min} = 0$, fringe contrast can be maximized by minimizing the effective

background light buildup encountered in conventional incoherent holography [15]. This will become more evident in a later section when computer simulated holograms are discussed.

3.1.3 Reconstruction of incoherent 3-D surfaces

Though indicated as a planar object in Figure 4, $|\Gamma_2|^2$ can in general be three dimensional in nature. This is easily verified for the two transverse dimensions x and y if one considers that the previous analysis leading to equation (3.1.11) could be similarly applied to any object point located in the plane of $|\Gamma_2|^2$. This, of course, is not a terribly remarkable statement, considering that most incoherent holographic methods to date have been capable of recording planar information [14,15]. Consider now the three dimensional representation of the planar object $|\Gamma_2|^2$ of Figure 4. We have

$$|\Gamma_2(x,y,z)|^2 = |\Gamma_2(x,y)|^2 \, \delta(z - z_o) \quad , \tag{3.1.13}$$

where z_o is the distance from the scanner to Γ_2. We can then write the processed signal corresponding to $|\Gamma_2|^2$, using equation (3.1.5), as

$$v(x,y) = V_{DC} + Re\left\{ \mathcal{F}^{-1}\left[OTF(f_x,f_y;z_o)\, \mathcal{F}\left\{ |\Gamma_2(x,y)|^2 \right\} \right] \exp\left(-j2\pi \frac{f_o}{v_x} x \right) \right\} \quad , \tag{3.1.14}$$

where we have left the z dependence out of the left hand side of equation (3.1.14) in order to emphasize that the recorded holographic data remain two-dimensional. Using the sifting property of delta functions, equation (3.1.14) can be written as

$$v(x,y) = V_{DC} + Re\left\{ F^{-1}\left[\left(\int_{-\infty}^{\infty} OTF(f_x, f_y;z)\, \delta(z - z_o)\, dz \right) F\left\{ |\Gamma_2(x,y)|^2 \right\} \right] \right.$$
$$\left. x \ \exp\left(-j2\pi \frac{f_o}{V_x} x \right) \right\} \quad . \qquad (3.1.15)$$

Rearranging terms we have

$$v(x,y) = V_{DC} + Re\left\{ F^{-1}\left[\int_{-\infty}^{\infty} OTF(f_x, f_y;z)\, F\left\{ |\Gamma_2(x,y)|^2 \delta(z - z_o) \right\} dz \right] \right.$$
$$\left. x \ \exp\left(-j2\pi \frac{f_o}{V_x} x \right) \right\} \quad , \qquad (3.1.16)$$

or

$$v(x,y) = V_{DC} + Re\left\{ F^{-1}\left[\int_{z_o}^{z_o + \delta z} OTF(f_x,f_y;z)\, F\left\{ |\Gamma_2(x,y,z)|^2 \right\} dz \right] \right.$$
$$\left. x \ \exp\left(-j2\pi \frac{f_o}{V_x} x \right) \right\} \quad , \qquad (3.1.17)$$

where equation (3.1.17) can be taken to represent the generalized output, for 3-D objects, of the image processor of Figure 4 and the limits of integration are chosen, as shown in Figure 6, to correspond to the region in which the scanned object exists. (We note that, strictly speaking, equation (3.1.17) is valid for only reflective or weakly scattering transmissive 3-D objects.) From Figure 6 we see that z_o is now taken as the point on the 3-D object $|\Gamma_2(x,y,z)|^2$ closest to the scanning mirror, while δz is the total depth of the object. Equation (3.1.17) can be used to represent the hologram of a 3-D object if the OTF is chosen as in equation (3.1.7). This technique contrasts with many earlier incoherent holographic techniques [15] whose optical arrangements allowed only the holographic recording of planar objects -

i.e., depth information was often severely distorted. We also note that our methods are not limited to transmissive type objects. As shown in Figure 6, if the collecting lens ℓ_i is used to image $|\Gamma_2|^2$ onto a highly sensitive photodetection device, such as a photomultiplier tube (PMT), then holograms of reflective objects can be made as well.

We now turn our attention to the reconstruction of holograms recorded by the heterodyne scanning method. Consider, for instance, that an on-axis hologram was recorded (i.e., $d = f_o = 0$). Also consider that reconstruction is now taking place with monochromatic, infinite uniform plane wave illumination. For a single plane of an object the recorded hologram can be written, according to equation (4.1.14), as

$$v(x,y;z) = V_{DC} + \frac{1}{2}F^{-1}\left\{OTF \times F\left\{|\Gamma_2|^2\right\}\right\} + \frac{1}{2}\left[F^{-1}\left\{OTF \times F\left\{|\Gamma_2|^2\right\}\right\}\right]^* \quad , (3.1.18)$$

where we recall that $A + A^* = 2Re\{A\}$ (refer to equation (3.1.5)) and the OTF is

$$OTF(f_x, f_y; z_o) = \exp\left(j\pi\lambda z_o\left(f_x^2 + f_y^2\right)\right) \quad , \qquad (3.1.19)$$

with nonessential constants left out and where we take the plane under consideration to be located a distance z_o in front of the scanner. The first term of equation (3.1.18) is simply the background bias term, while the second and third terms correspond to, respectively, the real and virtual reconstructed image terms, as will be evident shortly.

Using the second term of equation (3.1.18), the reconstructed real image intensity seen by the observer can be written as

$$I_r \simeq \left|F^{-1}\left\{OTF \times H_z \times F\left\{|\Gamma_2|^2\right\}\right\}\right|^2 \quad , \qquad (3.1.20)$$

where H_z is the free space spatial *transfer function* indicating the propagation of the diffracting field resulting in the reconstructed real object a distance $z = z_0$ in *front* of the hologram. (We

assume unity magnification of the holographic information so that reconstruction takes place at the same distance in front of the hologram as the distance the original object was in front of the scanning mirror.) Since $H_z(z = z_o)$ is given by

$$H_z(z = z_o) = \exp\left(-j\pi\lambda z_o\left(f_x^2 + f_y^2\right)\right) = OTF^* \quad , \tag{3.1.21}$$

with an nonessential constant left out, we see immediately that equation (3.1.20) reduces to

$$I_r = |\Gamma_2|^4 \quad . \tag{3.1.22}$$

A reconstructed virtual image would be obtained, a distance -z behind the hologram, if the third term of equation (3.1.18) was used in conjunction with $H_z(z = -z_o)$ in equation (3.1.20).

From equation (3.1.22) we see a further difference of incoherent holography, as compared to conventional coherent techniques. Whereas Γ_2 is recorded and $|\Gamma_2|^2$ is viewed upon reconstruction in coherent holography, we find that $|\Gamma_2|^2$ is recorded and $|\Gamma_2|^4$ is viewed upon reconstruction in incoherent holography. Object points of relatively low intensity (as compared to bright object points) will thus tend to be supressed upon reconstruction using incoherent techniques. This limitation, combined with the possible bias buildup problems mentioned earlier, indicates that objects of choice for minimal distortion in incoherent holography are high contrast objects with only moderate spatial detail. If, however, one is willing to accept a loss of spatial resolution (through effective spatial low pass filtering due to bias buildup) and contrast upon reconstruction, more complicated objects could be used. Note that the need for these considerations is not made evident through the discussion of only point source holograms, as both coherent and incoherent holography perform equally well for point objects.

3.1.4 Compatibility with real-time spatial light modulators

Just as with coherent holography, incoherent holograms incorporating spatial frequency carriers cause a spatial separation of the real and virtual objects, and the throughput light. If we measure this separation as the angular deviation θ_d of the real reconstructed object from the throughput light (which generally can be considered as propagating normal to the hologram surface upon reconstruction), we find with the aid of equations (3.1.10)-(3.1.12) that

$$\theta_d \simeq \sin\theta_d = \frac{x_o}{z} = \left(\frac{d}{f_2} - \lambda\frac{f_o}{v_x}\right) [radians] \quad , \tag{3.1.23}$$

where the paraxial approximation is assumed, and z describes the reconstruction distance from the hologram. Note that the angular deviation can be adjusted by varying the displacement d between the scanning fields U_1 and V_1. Most importantly, however, is the ability to create an angular deviation through the choice of f_o, which can be adjusted electronically. Since the choice of the temporal carrier f_o is essentially only limited by the spatial frequency limitations of the display device, such as commercially available EBSLMs [9], this aspect of angular deviation adjustment tends to make the scanning system compatible with real-time display devices.

Another important advantage of the heterodyne scanning technique is the introduction of the constant bias during recording. In standard holographic recording, $|O+R|^2$ is recorded, where O and R represent the wavefronts of the object and the reference waves, respectively. Note that

$$|O+R|^2 = |O|^2 + |R|^2 + OR^* + O^*R \quad , \tag{3.1.24}$$

where the first two bias terms are spatially variant and produce annoying effects in on-axis holography. They also cause unnecessary information content to be recorded, which is undesirable in off-axis holography. In contrast, the bias term in the heterodyne scanning system is constant (see equation (3.1.17)). This in turn leads to a reduction of the spatial resolution required of the recording medium - an issue of major concern when spatial light modulator applications in holography are considered. The effect of constant bias buildup is further investigated in section 3.2.4.

3.1.5 Heuristic description

To conclude this section we mention that equation (3.1.17) has a relatively simple physical interpretation in that the principle of holographic recording is to cause the convolution of a Fresnel zone plate, or FZP (the impulse response of the scanning holography system), with some general object through scanning. The FZP can in essence be visualized as emanating from the scanning mirror as the plane and spherical waves propagate and interfere. It is then by scanning this FZP across the object that the convolution takes place. Convolving this FZP with a general object yields the hologram of that object. Though this description is somewhat simplistic, it aids in understanding the general concepts. We also note that, based on this description, it is possible to formulate our techniques based on the fields at the scanning mirror instead of U_1 and V_1. We shall refrain from doing this so that the more general formalism developed in reference [4] is preserved.

3.2 Gaussian Beam Theory

This section begins with a Gaussian beam analysis of the defocused OTF. The scaling, magnification and resolution properties of the scanning holographic process are then investigated under the Gaussian beam assumption. This is followed by a discussion of experiments performed to verify the theoretical expectations. The section then concludes with a discussion of the bias reduction properties of the technique.

3.2.1 Gaussian beam analysis

Generally speaking it is impossible to choose U_1 and V_1 such that at the scanner we have the superposition of a true uniform infinite plane wave and a true point source. Since the spatial distribution of the scanning laser beam is in general taken to be Gaussian, we therefore consider the superposition of a broadened and a focused Gaussian beam. This can be accomplished experimentally by removing lens ℓ_2 from the propagation path of pupil U_1 and by altogether removing any physical pupils at both planes U_1 and V_1, as shown in Figure 6. In order to employ equation (3.1.3), effective values for U_1 and V_1 have to be determined under this condition. The effective pupil function V_1, by direct inspection of Figure 4, is given by

$$V_1 = \frac{1}{\pi\omega_v^2}\exp\left(-\frac{\left(x^2+y^2\right)}{\omega_v^2}\right) \quad , \tag{3.2.1}$$

where $\omega_v = M_{cv}\omega_o$, M_{cv} is the magnification of the collimator in the path of V_1 and ω_o is the Gaussian waist of the laser source beam.

As for the specification of pupil function U_1, since lens ℓ_2 has been removed, as shown in Figure 6, we find the effective pupil function U_1 by specifying the broadened Gaussian distribution at the scanning mirror and equating this distribution to the Fourier transform of U_1. Mathematically, this is written as

$$\exp\left(-\frac{(x^2+y^2)}{(M_{cu}\omega_o)^2}\right) = F\{U_1\} \quad , \tag{3.2.2}$$

where $f_x = x/\lambda f_2$, $f_y = y/\lambda f_2$ are the spatial frequencies employed in the Fourier transformation in equation (3.2.2). Solving for U_1 gives

$$U_1 = \frac{1}{\pi\omega_u^2}\exp\left(-\frac{(x^2+y^2)}{\omega_u^2}\right) \quad , \tag{3.2.3}$$

where $\omega_u = \lambda f_2/\pi\omega_o M_{cu}$.

Notice that due to the phase flattening properties of the collimators, equations (3.2.1) and (3.2.3) represent real Gaussian functions. Also notice that U_1 and V_1 have been chosen to be normalized Gaussians; i.e.,

$$\int_{-\infty}^{\infty}\int_{-\infty}^{\infty}\Psi_1\, dxdy = 1 \quad , \tag{3.2.4}$$

where Ψ_1 represents either U_1 or V_1. Now, taking $f_2 = 17.5cm$, $\lambda = 633nm$, $M_{cu} = M_{cv} = 10$ and $\omega_0 = 1mm$, as is the case in our actual experimental set-up, we find that $\omega_u = 3.526\mu m$ and $\omega_v = 1.0cm$. As expected, $\omega_u << \omega_v$. A somewhat more quantitative description of how the relative sizes of ω_u and ω_v effect the hologram generation process will be presented later, though for now simply note that the condition $\omega_u << \omega_v$ is required so that we may most closely model the pupil interaction discussed in the previous section (i.e., $V_1 = 1$ and $U_1 = \delta(x,y)$).

Before calculating the OTF of the scanning holographic system we make one further observation. That is, for generality, we still consider that U_1 is subject to a possible intraplanar translation by a distance d, though with U_1 existing only as an effective pupil function, as in our experimental system, causing this translation directly is impossible. One method of causing an effective translation of pupil U_1 in this case is to slightly misalign the system such that the mirror following the collimator in the propagation path of U_1 is positioned at an angle slightly greater or less than 45° from the direction of the incident collimated light (see Figure 4). Taking θ_m as the incremental misalignment angle from 45°, the effective displacement d_{eff} is then found through simple geometrical considerations to be

$$d_{eff} = 2f_2\theta_m \quad , \tag{3.2.5}$$

where θ_m is expressed in radians, and where an analogy has been drawn between the propagation angle θ of the plane wave in Figure 5, when U_1 is translated by d, and the propagation angle of the collimated beam when the mirror under consideration is misaligned by θ_m.

We now calculate the OTF by inserting equations (3.2.1) and (3.2.3) into equation (3.1.3). Performing the required calculations and simplifications we obtain the result

$$OTF(f_x, f_y;z) = \exp\left(-K + \frac{H^2}{G}\right) \exp\left(-G\left\{\left(f_x + \frac{H}{G}\right)^2 + f_y^2\right\}\right) \quad , \tag{3.2.6}$$

where

$$G = \left\{ \eta\left(\frac{\lambda f_2}{\omega_v}\right)^2 + \eta\left(\frac{\pi\omega_u z}{f_2}\right)^2 + j\pi\lambda(1-2\eta)z \right\} \quad [m^2]$$

$$H = \eta d\left\{ \frac{\lambda f_2}{\omega_v^2} + j\frac{\pi z}{f_2} \right\} \quad [m] \tag{3.2.7}$$

$$K = \frac{d^2\eta}{\omega_v^2} \quad , \quad \eta = \frac{\omega_v^2}{\omega_u^2 + \omega_v^2}$$

and where an nonessential constant has been left out of equation (3.2.6). In addition, by inverse Fourier transforming equation (3.2.6), the impulse response is found to be

$$\tilde{V}_\delta(x,y;z) = \frac{1}{G}\exp(-K)\,exp\left(-\frac{\pi^2}{G}\left\{\left(x + j\frac{H}{\pi}\right)^2 + y^2\right\}\right) \quad , \tag{3.2.8}$$

with an nonessential constant left out. As a check, letting $\omega_v \to \infty$ and $\omega_u \to 0$, we readily see, for the ideal case, that $\eta \to 1$, $G \to -j\pi\lambda z$, $H \to jd\pi z/f_2$, $K \to 0$ and equations (3.2.6) and (3.2.8) reduce to equations (3.1.7) and (3.1.8), respectively.

Notice that both G and H are complex quantities. If we now expand the argument of the second exponential term in equation (3.2.6) and collect the real (decay) and imaginary (phase and frequency) terms, we can calculate the spatial carrier offset to be

$$f_{xo} = -\left(Re\left\{\frac{H}{G}\right\} + \left(\frac{G_r}{G_i}\right)Im\left\{\frac{H}{G}\right\} + \frac{f_o}{v_x}\right) \quad [m^{-1}] \quad , \tag{3.2.9}$$

where G_r and G_i are the real and imaginary parts of G, respectively, and where the contribution of the temporal frequency carrier f_o has been included. Again, under the condition that $\omega_v \to \infty$ and $\omega_u \to 0$ we find that equation (3.2.9) reduces directly to equation (3.1.10).

In order to aid in visualizing the results expressed in equations (3.2.6) - (3.2.8) we provide Figures 7 - 17. Figure 7 shows a simulation of equation (3.1.9), when $|\Gamma_2|^2 = \delta(x,y)$, $f_{xo} = 0$ (i.e., $d = f_o = 0$), $\lambda = 633nm$, $\omega_u = 3.526\mu m$, $\omega_v = 1.0cm$, $z = f_2 = 17.5cm$, $\phi_{uv} = -\pi/2$ and when $\tilde{V}_\delta$ is

chosen as described in equation (3.2.8). The choice of $z = f_2$ was made because in actual experiments, at $z = f_2$ (see Figure 4) the collimated and diverging beams coinciding at $|\Gamma_2|^2$ most completely and uniformly overlap - ultimately yielding optimal fringe contrast. In fact, it is easily shown that as $z \rightarrow \infty$, the OTF described by equation (3.2.6) approaches zero. We will thus take $z \simeq f_2$ as a generally applicable operating requirement (i.e., $|\Gamma_2|^2$ located nominally at $z \simeq f_2$ and the total depth of $|\Gamma_2|^2$ much less than f_2). We also mention that Figure 7, as with Figures 8 - 11, has been normalized so that the maximum value is unity and $V_{DC} = 0.5$, and that ϕ_{uv} is chosen to be $-\pi/2$ so that on-axis impulse response simulations have a central maximum..

Figure 7 is readily identified as a Fresnel zone plate, characteristic of on-axis point source holograms. We only begin to notice the effects of the Gaussian wave interaction when we inspect Figure 8 which shows a one dimensional slice through Figure 7 when y=0. Note the apodization of the FZP as $|x|$ increases. As this effect would not be present in the case of true spherical and plane wave interaction, we attribute this apodization to the Gaussian nature of the interfering beams. Figure 9 is a cross section plot of a carrier frequency hologram with d=0 and $f_o/v_x = -3.2\ c/mm$ (i.e., $2\pi f_{xo} = 20\ radians/mm$) in equation (3.2.8). Note the shift in the central fringe and the apparent contrast reversal.

To investigate the importance of the relative sizes of ω_u and ω_v, we increased ω_u in our simulation from $3.526\mu m$ to $40\mu m$ and generated Figures 10 and 11. As in Figure 9, the spatial carrier frequency in Figure 11 is $2\pi f_{xo} = 20\ radians/mm$, with d=0 and $f_o/v_x = -3.2\ c/mm$. Notice the more drastic decay of the fringes in these plots caused by increasing ω_u. Notice also that the fringe spacings in Figures 10 and 11 do not perceptibly differ from those in Figures 8 and 9. These effects are verified by closely inspecting equation (3.2.8), when, for simplicity we take $d = f_o = H = 0$. It is seen that fringe decay is proportional to Re{1/G} while fringe spacing is inversely proportional to Im{1/G}. It can be shown by inserting various values for ω_u and ω_v into the expression for G, that if $\omega_u << \omega_v$, then as ω_u increases, Re{1/G} increases, causing a more distinct decay, while Im{1/G} and thus the fringe spacing remain

essentially unchanged. If, however, ω_u increases so that $\omega_u \simeq \omega_v$, we find that Im{1/G} decreases rapidly, causing the fringe spacing to increase accordingly. Furthermore, it can be shown that if $\omega_u = 3.526\mu m$ and $\omega_v = 1.0cm$, as in our experiments, then the fringe spacing is imperceptably different from the ideal case when $\omega_u = 0$ and $\omega_v = \infty$ (i.e., $\pi^2 Im\{1/g\}$ is approximately equal to the parameter $\pi/\lambda z$ in equation (3.1.11)). It thus becomes apparent that the requirement $\omega_u << \omega_v$ is necessary so that equation (3.2.8) most closely resembles the ideal impulse response of equation (3.1.8).

The necessity of requiring $\omega_u << \omega_v$ is further emphasized by inspecting Figures 12 - 15. Here we have plotted the width of the point source hologram, ω_H, defined as the radial location where the apodization envelope falls to the value 1/e, and the number of fringes N within the hologram out to ω_H, for various values of ω_u and ω_v. All four figures are plotted assuming $d = f_o = 0$ (i.e., on-axis), $\lambda = 633nm$, $z = f_2 = 17.5cm$ and $\phi_{uv} = -\pi/2$. Figures 12 and 13 assume $\omega_u << \omega_v$ while Figures 14 and 15 assume $\omega_u \simeq \omega_v$. Specifically, from equation (3.2.8) we find that

$$\omega_H = \frac{1}{\pi\sqrt{Re\{G_{inv}\}}} \quad , \tag{3.2.10}$$

where $G_{inv} = 1/G$. The number of fringes within ω_H is also found from equation (3.2.8) by considering only the imaginary (or oscillatory) terms and by setting $x^2 + y^2 = r^2 = \omega_H{}^2$. We then evaluate the expression

$$\omega_H^2 \pi^2 Im\{G_{inv}\} - (\phi_{G_{inv}} + \phi_{uv}) = (2N-1)\pi \quad , \tag{3.2.11}$$

where $\phi_{G_{inv}}$ is a phase term arising from the 1/G factor which precedes the exponentials in equation (3.2.8) and the right hand side of equation (3.2.11) was chosen in order to count the number N of minimums through which the oscillatory terms pass. It is easily shown that

$\phi_{G_{inv}} \simeq \pi/2$ if $\omega_u << \omega_v$ (see, for example, the ideal ϕ term of equations (3.1.12)). Inserting equation (3.2.10) into equation (3.2.11) we find that

$$N = \frac{1}{2\pi}\left(\frac{Im\{G_{inv}\}}{Re\{G_{inv}\}} - (\phi_{G_{inv}} + \phi_{uv})\right) + \frac{1}{2} \quad . \tag{3.2.12}$$

From Figures 12 and 13 we see that if $\omega_u << \omega_v$, then as ω_u increases, we expect fewer fringes within ω_H. This is verified by reinspecting Figures 8 and 10 and is due primarily to the increasing decay factor Re{1/G}. As per the previous discussion, change in fringe spacing essentially does not influence the results of Figures 12 and 13. On the other hand, Figures 14 and 15 show that though the hologram width ω_H remains appreciable if $\omega_u \simeq \omega_v$, the number of fringes within ω_H falls essentially to zero. (Note that Figure 15 represents five overlaping curves, one each for the five values of ω_u. Again, as per the previous discussion, this loss of fringes is due to the increased fringe spacing as ω_u approaches ω_v (i.e., as Im{1/G} decreases). As it is well known that several fringes are necessary for a FZP to exhibit a proper lens-like focusing action, it is clearly unacceptable if ω_u is chosen comparable to ω_v. Thus the earlier statement that $\omega_u << \omega_v$ is a necessary requirement for proper hologram generation is further reinforced. In fact, Figures 12 - 15 give us guidelines by which to choose ω_u and ω_v such that a certain number of fringes within the hologram is maintained.

Consider now the spatial carrier frequency f_{xo} expressed in equation (3.2.9). We have plotted equation (3.2.9) as f_{xo} vs. d in Figure 16 under the assumptions that $\omega_v = 1.0cm$, $\omega_u = 3.526\mu m$, $\lambda = 633nm$, $f_o = 0$ and $f_2 = 17.5cm$. Notice that if $\omega_u << \omega_v$, then regardless of the depth parameter z (Figure 16 shows five overlapping plots), the slope of the resulting line is constant. In fact, this slope is negligibly close to the value $1/\lambda f_2$, as predicted under ideal conditions ($\omega_u \to 0$, $\omega_v \to \infty$) by equation (3.1.10). (It should be mentioned that though Figure 16 is plotted for widely varying values of z, this is done merely to show that equation (3.2.9) is essentially independant of z when $\omega_u << \omega_v$, as expected. In general, we will require $z \simeq f_2$, as previously discussed.) Note, however, that as d increases, the exp(-K) terms in both

equations (3.2.6) and (3.2.8) begin to decay, as is expected, since when $d \neq 0$ the interferometer configuration of Figure 4 becomes misaligned. This decay is illustrated in Figure 17, where the relative OTF amplitude is plotted for all f_x and f_y as a function of the misalignment factor d. The parameters of interest again are $z = f_2 = 17.5cm$, $\lambda = 633nm$, $\omega_v = 1.0cm$ and where ω_u is variable. Once again notice that the curves are independant of ω_u if $\omega_u << \omega_v$ (i.e., Figure 17 also contains five overlaping curves). We now turn our attention to a few topics of interest regarding holographic reconstructions under the Gaussian beam assumption.

3.2.2 Scaling, magnification, resolution and distortion

Let us first consider the reconstruction of a simple on-axis ($d = f_o = 0$) point source hologram recorded by our method. From equation (3.1.20), with $|\Gamma_2|^2 = \delta(x,y)$, we see that the real object can be expressed as

$$I_r = \left|F^{-1}\{OTF \times H_z\}\right|^2 \quad , \tag{3.2.13}$$

where the OTF and H_z are expressed in equations (3.2.6) and (3.1.21), respectively. Performing the required calculations we find

$$I_r = \left| \frac{1}{4\pi G'} \exp\left(-\frac{(x^2 + y^2)}{4G'} \right) \right|^2 \quad , \tag{3.2.14}$$

where a constant phase term has been ignored and where

$$4G' = \left(\frac{\eta}{\pi^2} \left(\frac{\lambda f_2}{\omega_v} \right)^2 + \eta \left(\frac{\omega_u z}{f_2} \right)^2 - j \frac{2\pi z}{\pi} (\eta - 1) \right) \quad . \tag{3.2.15}$$

Under the assumptions that $z \simeq f_2$ and $\omega_u << \omega_v$, it is clear that $\eta \simeq 1$ and that the first two terms of equation (3.2.15) dominate. For the system then, when $M_{cv} = M_{cu}$, we find from equations (3.2.1) and (3.2.3) that $\omega_u = \lambda f_2/\pi\omega_v$ so that $4G' \simeq 2\omega_u^2$. Equation (3.2.14) then reduces to

$$I_r \propto \exp\left(-\frac{(x^2 + y^2)}{\omega_u^2} \right) \quad . \tag{3.2.16}$$

We thus see that our reconstructed object is a Gaussian function whose intensity width at the 1/e point is no smaller than ω_u. Figure 18 shows a simulated on-axis reconstructed point source when $\omega_u = 3.526\mu m$. Therefore, it is evident that the choice of ω_u will influence the resolution of the scanning holographic system. So in addition to requiring that $\omega_u << \omega_v$, ω_u should also be made small so as to maximize resolution. We will now investigate these effects further.

Consider the holographic recording of an object consisting of three distinct point sources such that

$$|\Gamma_2|^2 = \delta(x,y;z - z_o) + \delta(x - x_o, y, z - z_o) + \delta(x,y;z - (z_o + \Delta z_o)) \quad , \tag{3.2.17}$$

as shown in Figure 19, where z_o is the distance from the scanner to points 1 and 2, Δz_o is the relative depth between points 1 and 3, and x_o is the intraplanar translation from point 1, in the x direction of point 2. We then find that $F\{|\Gamma_2|^2\}$ is

$$F\{|\Gamma_2|^2\} = \delta_1(z - z_o) + \exp(-jK_x x_o)\delta_2(z - z_o) + \delta_3(z - (z_o + \Delta z_o)) \quad . \tag{3.2.18}$$

Considering on-axis recording with $\omega_u << \omega_v$ (i.e., $\eta \to 1$), we can write the OTF of equation (3.2.6) as

$$OTF = \exp\left(-\frac{G}{4\pi^2} (K_x^2 + K_y^2) \right) \quad , \tag{3.2.19}$$

where

$$\frac{G}{4\pi^2} = \left\{ \frac{\omega_u^2}{4}\left(\varepsilon + \frac{z^2}{f_2^2}\right) - j\frac{\lambda_1}{4\pi}z \right\}$$
$$\varepsilon = \left\{ \frac{\lambda_1 f_2}{\pi\omega_v\omega_u} \right\}^2 \quad , \tag{3.2.20}$$

and λ_1 is the recording wavelength. Typically, ε will be approximately one. In fact for our system $\varepsilon = 1$ exactly, since as previously mentioned $\omega_u = \lambda_1 f_2/\pi\omega_v$.

Once again we look for the reconstructed object by evaluating equation (3.1.20), when the OTF is now given as in equation (3.2.19). However, we now write the spatial transfer function as

$$H_\ell = \exp\left(-j\frac{\lambda_2 \ell}{4\pi}\left(K_x^2 + K_y^2\right)\right) \quad , \tag{3.2.21}$$

where λ_2 is the wavelength of the incident plane wave used to reconstruct the hologram of $|\Gamma_2|^2$, and ℓ is the distance, yet to be determined, at which each point in $|\Gamma_2|^2$ reconstructs to a real image. For the first term of equation (3.2.18) we can write

$$\mathrm{I}_{r1} = \left| F^{-1}\left\{ \exp\left(-\frac{G(z_0)}{4\pi^2}\left(\left(\frac{K_x}{S_x}\right)^2 + \left(\frac{K_y}{S_x}\right)^2\right)\right) \right.\right.$$
$$\left.\left. \times \exp\left(-j\frac{\lambda_2 \ell}{4\pi}\left(K_x^2 + K_y^2\right)\right)\right\}\right|^2 \quad , \tag{3.2.22}$$

where $G(z_o)$ indicates that the parameter G is evaluated at $z = z_o$, and scale factors S_x and S_y have been introduced into the OTF of equation (3.2.19). Scale factors arise because the area over which $|\Gamma_2|^2$ is scanned may not be equal to the area of the device which displays the resulting hologram, and we recall that

$$F\{\psi(S_x x,\ S_y y)\} = \frac{1}{|S_x S_y|}\Psi\left(\frac{K_x}{S_x}, \frac{K_y}{S_y}\right) \quad , \tag{3.2.23}$$

where ψ is some function, S_x and S_y are the scale factors and $F\{\psi\} = \Psi$. For example, if an object is scanned over a 2 cm x 1 cm area and its hologram is subsequently displayed on a 3 cm x 2 cm display device, then $S_x = 2/3$ and $S_y = 1/2$ (note that $S_x, S_y < 1$ results in magnification, suggesting the use of this technique in holographic microscopy). H_ℓ is, of course, not subject to scaling and, for simplicity, we will from now on assume $S_x = S_y = S$.

Continuing with the evaluation of equation (3.2.22) we have

$$\begin{aligned} I_{r1} = \Bigg| F^{-1}\Bigg\{ & \exp\left(-\left\{\frac{\omega_u^2}{4}\left(\varepsilon + \frac{z_o^2}{f_2^2}\right)\right\}\frac{1}{S^2}\left(K_x^2 + K_y^2\right)\right) \\ & \times \exp\left(j\left(\frac{\lambda_1 z_o}{4\pi}\frac{1}{S^2} - \frac{\lambda_2 \ell}{4\pi}\right)\left(K_x^2 + K_y^2\right)\right)\Bigg\}\Bigg|^2 \quad . \end{aligned} \tag{3.2.24}$$

The real object, then, is found where the phase term of equation (3.2.24) is cancelled. This can be understood by recalling that when a lens focuses a collimated (or phase flat) Gaussian beam, the minimum waist occurs where the phase curvature returns to zero. In equation (3.2.24) this occurs at a distance ℓ_1 from the hologram given as

$$\ell_1 = \frac{\lambda_1}{\lambda_2}\frac{1}{S^2} z_o \quad . \tag{3.2.25}$$

The evaluation of I_{r1} is then completed to yield

$$I_{r1} \propto \exp\left(-\frac{\left(x^2 + y^2\right)}{\omega_{r1}^2}\right) \quad , \tag{3.2.26}$$

where

$$\omega_{r1}^2 = \frac{1}{2}\left\{\left(\frac{\omega_u}{S}\right)^2\left(\varepsilon + \frac{z_o^2}{f_2^2}\right)\right\} \quad . \tag{3.2.27}$$

Proceeding in a similar fashion for the second and third terms of equation (3.2.18) we find the locations ℓ_2 and ℓ_3 and the widths ω_2 and ω_3 of the reconstructed images of points 2 and 3, respectively, to be $\ell_2 = \ell_1$, $\omega_{r1} = \omega_{r2}$,

$$\begin{aligned} \ell_3 &= \frac{\lambda_1}{\lambda_2}\frac{1}{S^2}(z_o + \Delta z_o) \\ \omega_{r3}^2 &= \frac{1}{2}\left\{\left(\frac{\omega_u}{S}\right)^2\left(\varepsilon + \frac{(z_o + \Delta z_o)^2}{f_2^2}\right)\right\} \quad . \end{aligned} \tag{3.2.28}$$

We also find that point 2 reconstructs in the plane $z = \ell_2$ at a point translated in the x direction by $\ell_{2x} = x_o/S$ from point 1.

The longitudinal (z directed) magnification M_{long} of the reconstructed image is then found to be

$$M_{long} = \frac{\ell_3 - \ell_1}{\Delta z_o} = \frac{\lambda_1}{\lambda_2}\frac{1}{S^2} \quad , \tag{3.2.29}$$

while the lateral (x directed) magnification M_{lat} is

$$M_{lat} = \frac{\ell_{2x}}{x_o} = \frac{1}{S} \quad . \tag{3.2.30}$$

Combining equations (3.2.29) and (3.2.30) we obtain the well known result [28,29]

$$M_{long} = \frac{\lambda_1}{\lambda_2} M_{lat}^2 \quad . \tag{3.2.31}$$

The preceding results are graphically depicted in Figure 19 where the input and reconstructed point objects are represented together in relative proportion when $S \geq 1$.

Consider now the lateral and longitudinal resolutions possible with the scanning holographic system. We will take the longitudinal resolution as the minimum value of Δz_o (which we will call Δz) such that upon reconstruction, the real images of points 1 and 3, in Figure 19, overlap where their intensities both equal 1/e. This is found by setting $\omega_{r1} + \omega_{r3}$ equal to $\ell_3 - \ell_1$. Solving this equality we find that

$$\Delta z = \frac{\lambda_2}{\lambda_1} S \frac{\omega_u}{\sqrt{2}} \left\{ \left(\varepsilon + \frac{z^2}{f_2} \right)^{\frac{1}{2}} + \left(\varepsilon + \frac{(z + \Delta z)^2}{f_2^2} \right)^{\frac{1}{2}} \right\} \quad , \tag{3.2.32}$$

where the nominal depth parameter z_o has been replaced with the more general variable z, to emphasize that the ability to resolve any two points on an extended object $|\Gamma_2|^2$ depends on the nominal distance from those points to the scanning mirror - not the distance z_o of the closest object point and the scanner as shown in Figure 6. Assuming that the minimum resolvable distance Δz is much smaller than the nominal depth parameter z, we can solve for the resolution Δz explicitly to find

$$\Delta z = \frac{\sqrt{2}\, \frac{\lambda_2}{\lambda_1} S \omega_u \left(\varepsilon + \frac{z^2}{f_2^2} \right)^{\frac{1}{2}}}{1 - \frac{\lambda_2}{\lambda_1} \frac{S \omega_u}{\sqrt{2}} \left(\varepsilon + \frac{z^2}{f_2^2} \right)^{\frac{1}{2}} \left(\frac{z}{\varepsilon f_2^2 + z^2} \right)} \quad . \tag{3.2.33}$$

The lateral resolution is found in a similar fashion by finding the minimum value of x_o (which we will call Δx) such that upon reconstruction the real images of points 1 and 2, in Figure 19, overlap where their intensities both equal 1/e. Now the equality to be solved is $\omega_{r1} + \omega_{r2} = \ell_{2x}$. Solving this equality we find directly that the lateral resolution is given as

$$\Delta x = \sqrt{2}\, \omega_u \left(\varepsilon + \frac{z^2}{f_2^2} \right)^{\frac{1}{2}} \quad . \tag{3.2.34}$$

Figures 20 - 23 provide a graphical representation of the lateral and and longitudinal resolutions, respectively, of the system as a function of z, for several small values of ω_u. Additionally, Figure 21 is plotted for S=1, while Figures 22 and 23 are plotted for S=5 and S=0.2, respectively . Other parameters of interest are $\lambda_1 = \lambda_2$ and $f_2 = 17.5cm$, Notice that Δx and Δz are in micrometers while z is in centimeters. Also notice from Figures 20 and 21 that if the scaling factor S is unity, then the lateral and longitudinal resolutions are imperceptably different, resulting in minimal distortion in reconstructed holographic images. This result is verified by noting that the denominator of equation (3.2.33) is approximately unity for S=1, $\lambda_1 = \lambda_2$ and ω_u small. Under these conditions then, equations (3.2.33) and (3.2.34) are approximately equal. However, as the scaling factor S changes, the lateral and longitudinal resolutions are no longer the same, as shown by inspecting Figures 22 and 23, since only Δz is a function of the scaling factor S. Thus, for example, as $|\Gamma_2|^2$ increases in size with respect to the area of the display device (i.e., S increasing) there is a loss of spatial detail along the z direction in the reconstructed holographic images. Furthermore, from Figures 20 - 23 we see that in order to resolve any neighboring points along z, the relative distance between them in $|\Gamma_2|^2$ must increase as z increases, indicating that as z increases it becomes more difficult to resolve fine spatial detail. *It should be noted that none of the above mentioned effects are evident under the previously discussed ideal assumptions of* $U_1 = \delta(x,y)$ *and* $V_1 = 1$, *since with these assumptions both* Δx *and* Δz *both approach zero for all z and S. Also note that the preceeding analysis does not account for resolution limits resulting from displaying a scaled hologram on a device with limited spatial bandwidth.*

Before continuing, two further comments are necessary concerning other distortion factors introduced by the practical experimental conditions. First, it is essential for distortion reduction purposes that objects be scanned in a linear fashion. This is most easily accomplished by using ramp signals to deflect the scanning mirrors, though, sinusoidal signals can also be used if the object is overscanned in such a way that during the central portion of the scan the object is scanned approximately linearly. (Note that if sinusoidal

scanning is used, then large objects will have to be placed farther from the scanner than small objects in order for linear scanning to take place. This will in turn require judicious selection of the focal length f_2 of lens ℓ_2 in Figure 4 so that fringe contrast is optimized - see the discussion in section 3.2.1.)

Also, it is reasonable to question whether or not there is phase distortion introduced into the detected signal by the non-parallel scanning nature of most scanning devices and the fact that the Fourier transforms of U_1 and V_1 are in effect created on the tilted Fourier plane of the scanning mirror, as indicated in Figure 4. In essence, neither of these factors result in noticable phase distortion. This is manifest by keeping scan angles small (either $|\Gamma_2|^2$ small or z large) so that paraxial scanning can be assumed and by noticing that light illuminating the scanning mirror is essentially the superposition of a point source and a plane wave. It is then easily seen that reflection at 90° (or small variations thereof) yields no phase distortion in the reflected plane wave. Furthermore, by causing the focused point due to the Fourier transformation of pupil V_1 to occur at the center of the scanning mirror (the only stationary point), no phase distortion is produced in the resulting spherical wave. We now turn our attention to experimental verification of the technique and some further simulations which aid in understanding the bias buildup reducing properties of the system.

3.2.3 Experimental verification

In order to experimentally verify the technique, precise measurements have been made of the signal representing the hologram of a 50 μm by 1 cm slit. As previously described, the experimental parameters of interest were $\omega_u = 3.526\mu m$, $\omega_v = 1.0cm$, $\lambda = 633nm$ and $z = f_2 = 17.5cm$. The slit can then be expressed as $|\Gamma_2|^2 = rect(x/a, y/b)$ where a = 50 μm and b = 1.0 cm and where we define

$$rect\left(\frac{x}{a}, \frac{y}{b}\right) = \begin{cases} 1; & \frac{-a}{2} \le x \le \frac{a}{2}, \ \frac{-b}{2} \le y \le \frac{b}{2} \\ 0; & elsewhere \end{cases} . \tag{3.2.35}$$

Using this description of $|\Gamma_2|^2$ and letting $d = f_o = 0$, equation (3.1.5) was first simulated using the OTF of equation (3.2.6). The result of this simulation is shown in Figure 24 for the y=0 cross section. Again, this plot is normalized to a maximum value of unity with $V_{DC} = 0.5$ Notice the appearance of the side lobes in the envelope apodising the fringe pattern in Figure 24, and that fringe visibility quickly drops off after $|x| \simeq 1.8mm$. To aid in interpreting this result, consider a Fresnel zone plate which is truncated in the radial direction after only a few fringes. Upon illunination, this FZP will exhibit poor focusing properties, yielding only a broadened spot, or line in one dimension, in its focal plane. Thus since a slit is in essence a broadened line, we expect its hologram to have fewer visible fringes, as in Figure 24, while retaining the basic FZP shape.

To measure the corresponding electrical signal representing the hologram of our slit, the signal just after the last amplifier of Figure 4 was directly fed into one of the vertical amplifiers of an oscilloscope. In order to ensure that we only looked at the y=0 cross section, the superposed scanning beams at the slit ($|\Gamma_2|^2$) were vertically centered, while the y scanning rate was set to zero. The displayed signal was then averaged 100 times to increase the signal-to-noise ratio.

The appropriate scale factor of our displayed signal was then determined by the following procedure. First the peak-to-peak excursion D from x=0 which the superposed scanning beams experienced was measured, in the plane of Γ_2, when the scanner was operating. As we used sinusoidal scanning signals, D was set large enough such that the scanning beam velocity was approximately constant over the 50 μm opening in Γ_2. The instantaneous velocity v_s of the scanning beam as it passed the center of Γ_2 (in the region of the 50 μm opening) was then determined, assuming sinusoidal scanning, to be

$$v_s = \frac{d}{dt}\left[\frac{D}{2}\cos(2\pi f_s t)\right]_{t=\frac{T}{4}} = \pi D f_s \left[\frac{m}{s}\right] \quad , \tag{3.2.36}$$

where f_s is the scanning frequency and T is the scanning period. We then multiply v_s by the TIM/DIV setting of the oscilloscope to obtain the scale factor S. For example, for this work D=1.2 cm, $f_s = 20Hz$ and TIM/DIV = 0.5 ms/div, yielding a scale factor S=0.377 mm/div. By then selecting a point on the oscilloscope trace located some number of divisions from the origin and multiplying its position (in oscilloscope divisions) by S, the corresponding location on , say, Figure 24 could be determined.

Several experimentally measured points were mapped onto the slit hologram simulation. The results are shown in Figure 25 where the scale has been enlarged from that of Figure 24 in order to emphasize the central fringes. We also mention that an assumed bias of $V_{DC} = 0.5$ was added to the experimental data after the amplitudes of the various points were normalized such that the maximum deviation from zero (the average value before adding the bias) was 0.5.

The data shown in Figure 25 proves to be quite repeatable, although averaging is usually necessary to reduce the noise. It is believed that the primary source of noise in our system is vibration induced by the oscillating scanner mirrors. Also, the interferometer arrangement in Figure 4 is not phase compensated to correct for errors such as thermal drift, and occasional signal fading has been observed as the room temperature fluctuates. Other contributions of noise likely arise due to the processing electronics and due to the fact that the composite scanning beam is usually not precisely azimuthally symmetric in the $|\Gamma_2|^2$ plane (as a result of various aberrations in the optical arrangement), although these contributions are relatively small. By carefully redesigning the optical arrangement of Figure 4, possibly to include heterodyned fiber optic techniques [30,31] and a higher precision scanning device, substantial reduction of all noise factors could be achieved.

3.2.4 Bias reduction

We now refer back to the earlier claim that this technique allow the effects of background bias buildup to be reduced from that normally encountered in incoherent holography. This is made visually evident with the aid of Figures 26-28. Figure 26 shows the y=0 cross section of the simulated on-axis hologram of a 200 μm x 1.0 cm slit. For comparison, Figure 27 shows experimentally measured hologram cross sections for 50 μm x 1.0 cm and 115.5 μm x 1.0 cm slits. As with previous simulations, Figure 26 has been normalized such that the peak value is unity and $V_{DC} = 0.5$ with $\omega_u = 3.526\mu m$, $\omega_v = 1.0cm$, $\lambda = 633nm$ and $z = f_2 = 17.5cm$. This normalization technique in essence represents the results which would be obtained by traditional incoherent holographic methods [15], where the bias level has equal contributions from each source point. This is seen by considering for a moment the incoherent hologram I_H of a collection of several point objects, as recorded by Cochran's method [15]. Quite simply the hologram would be

$$I_H = \frac{C}{2N} \sum_{i=1}^{N} \left\{ 1 + \cos\left(\frac{\pi}{\lambda z} \left((x - x_{oi})^2 + (y - y_{oi})^2 \right) \right) \right\} \quad , \tag{3.2.37}$$

where C is a constant, (x_{oi}, y_{oi}) is the location of each point at a common distance z from the recording plane, and where each point is equally radiant (as is the case with a uniformly illuminated slit). We see that the maximum and average intensity levels of this hologram are C and C/2, respectively, where C is chosen such that the maximum intensity level just reaches the saturation level of the recording medium. For simplicity, we set C=1.

From Figure 26 we see that this method results in a relatively high bias level as the object becomes continuous. As the fringes are what give rise to the focusing action of the hologram when the recorded object is reconstructed, we only need a bias such that I_H is

always non-negative. This can be achieved in our system by proper selection of V_{DC} and the audio amplifier gain (see Figure 4), and is depicted in Figure 28. In the simulation of Figure 28 the normalization was done as follows. First, the minimum value I_m of the data of Figure 24 was determined and subsequently subtracted from every data point. The difference $I_D = 1 - I_m$ was then divided into each data point, and since $I_D \leq 1$ we see that fringe visibility has been increased and the bias level reduced. (Again this normalization process is in practice carried out by properly adjusting the audio amplifier gain and V_{DC} as shown in Figure 4, where the maximum value output to the display device would be adjusted for maximum intensity modulation.

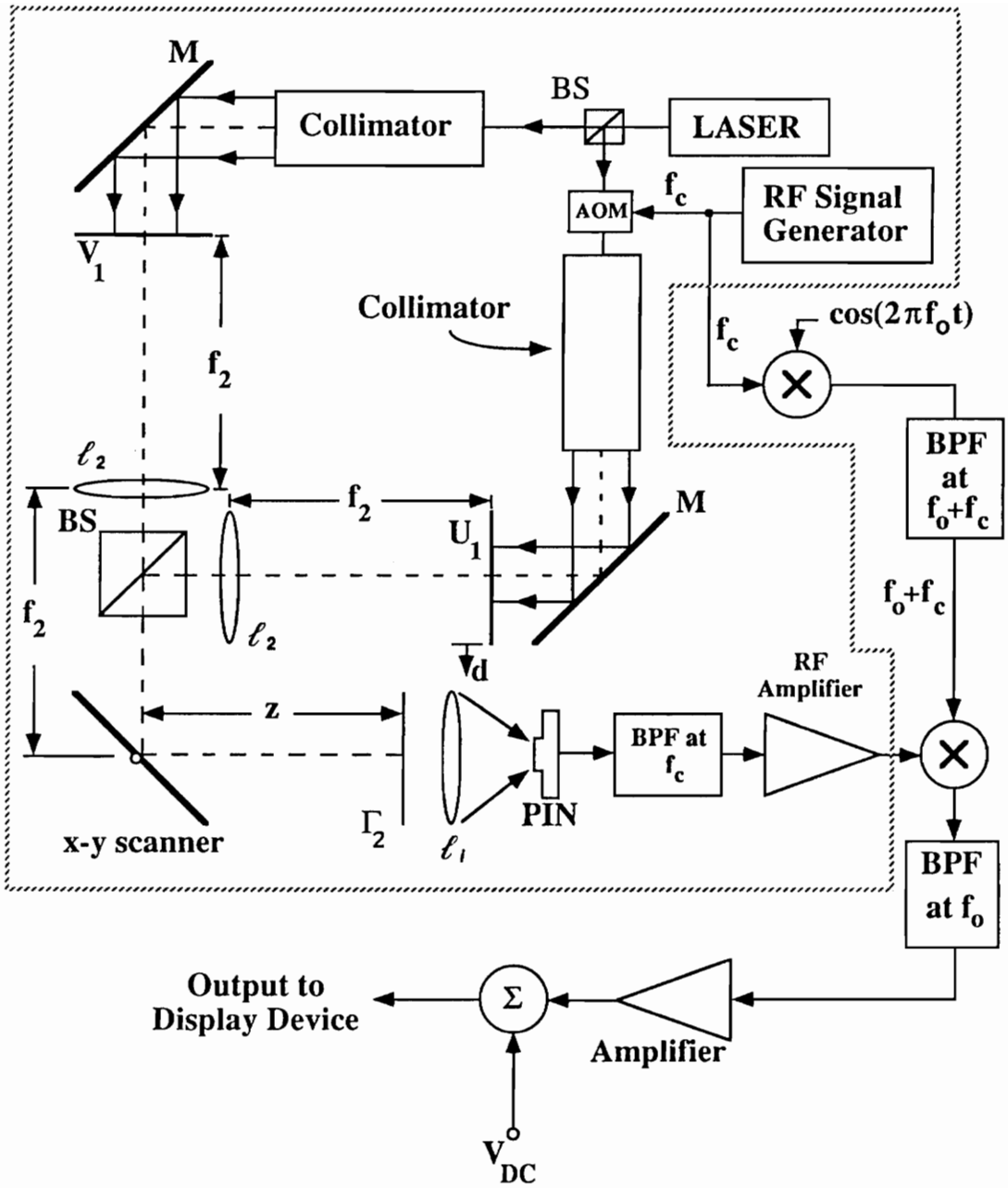

Figure 4. The optical scanning holography system: (with notation consistent with that of chapter 2).

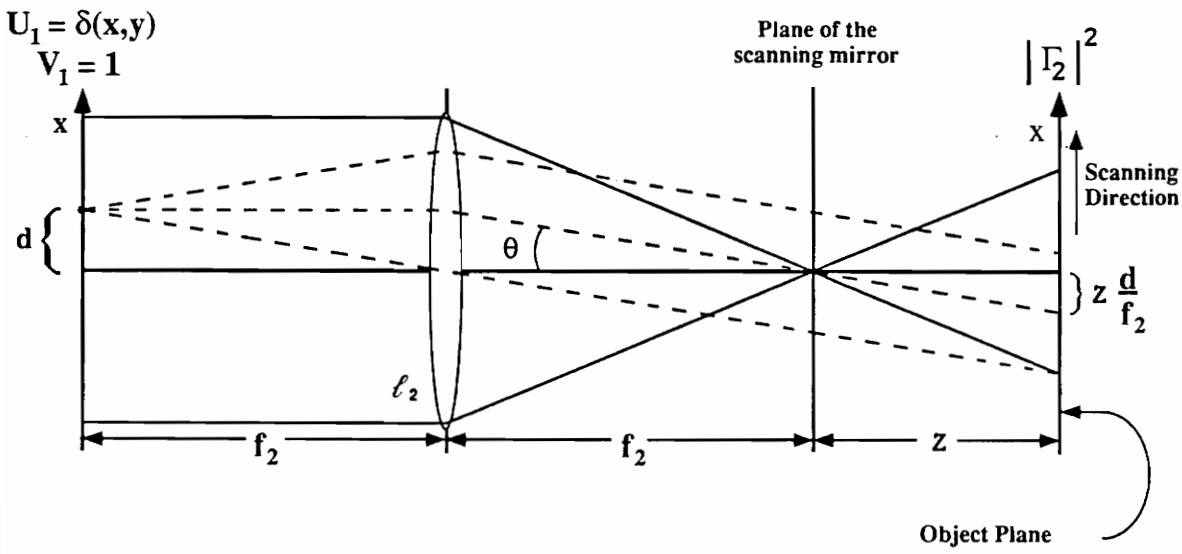

Figure 5. Construction of the composite scanning beam.

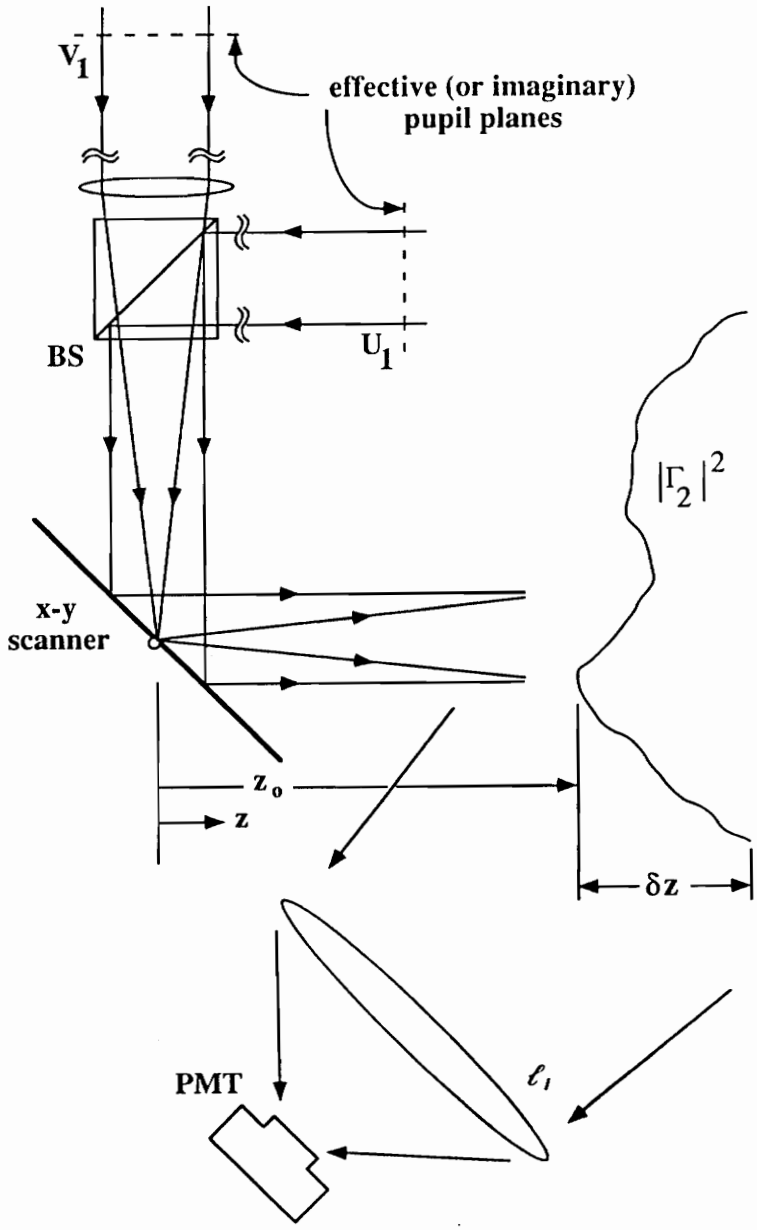

Figure 6. Holographic recording of a three dimensional object.

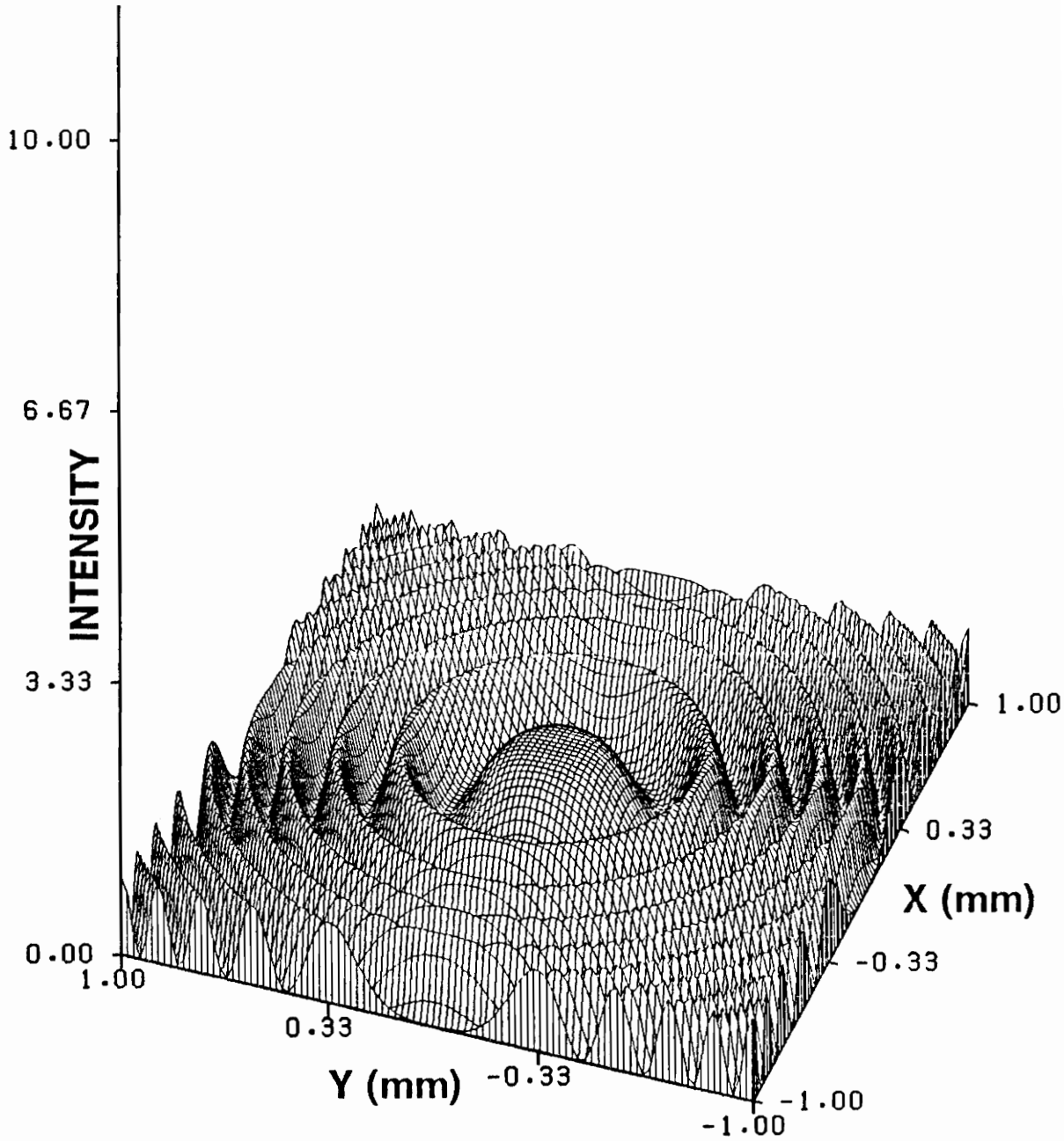

Figure 7. Point source hologram simulation.

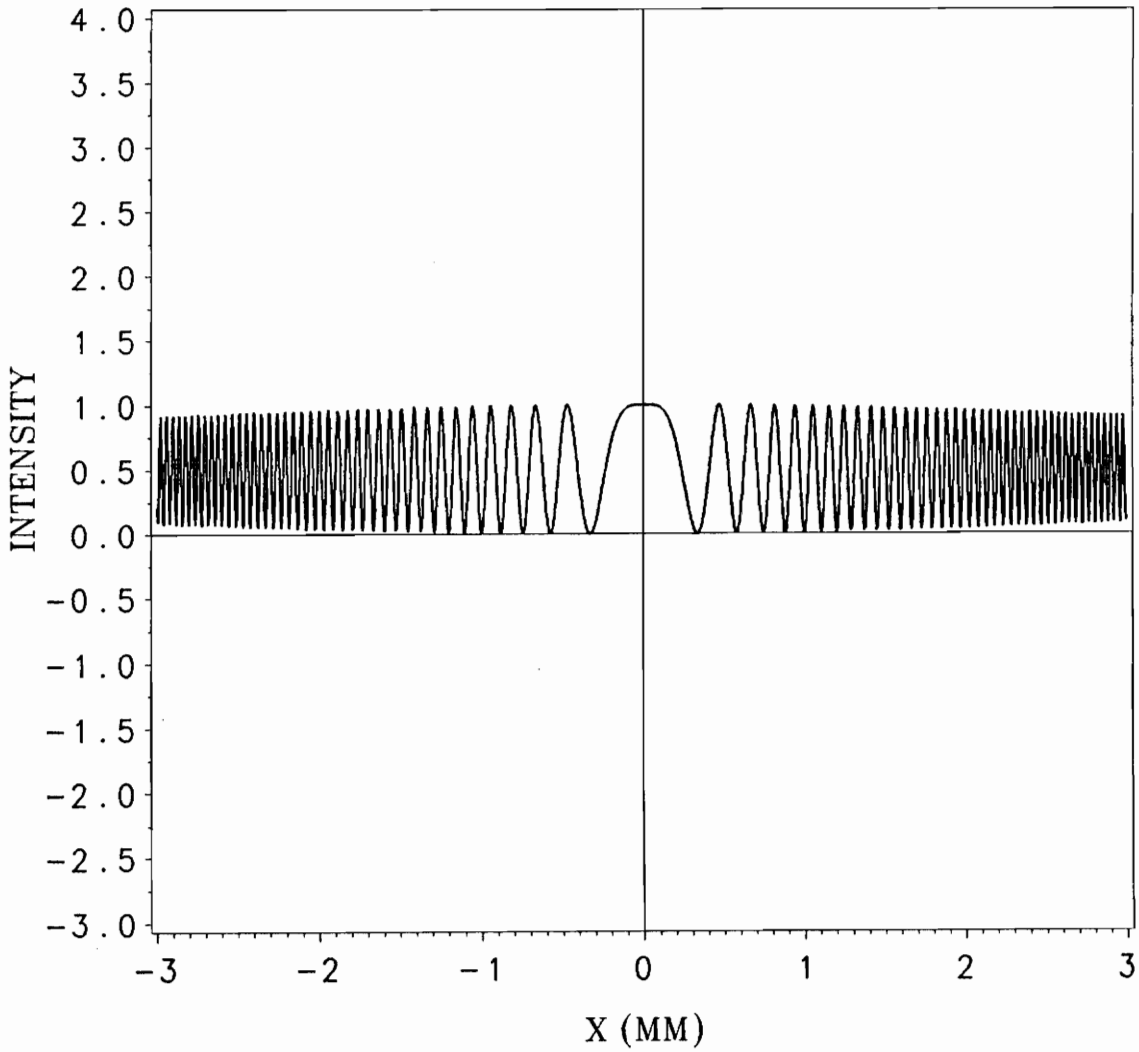

Figure 8. Cross section of a point source hologram: (generated with $\omega_u = 3.526\mu m$).

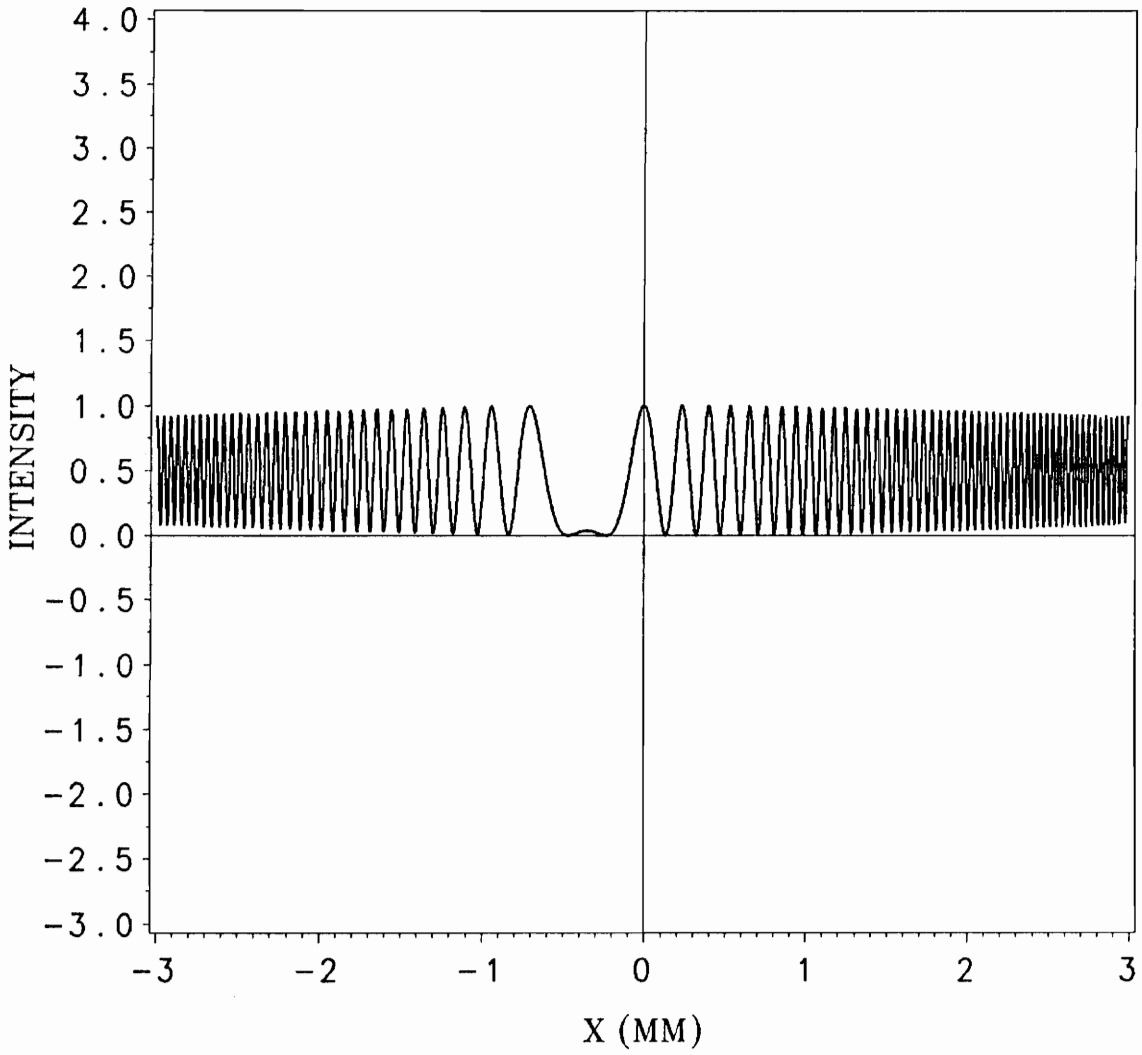

Figure 9. Cross section of a point source hologram: (with a small spatial carrier frequency included when $\omega_u = 3.526\mu m$).

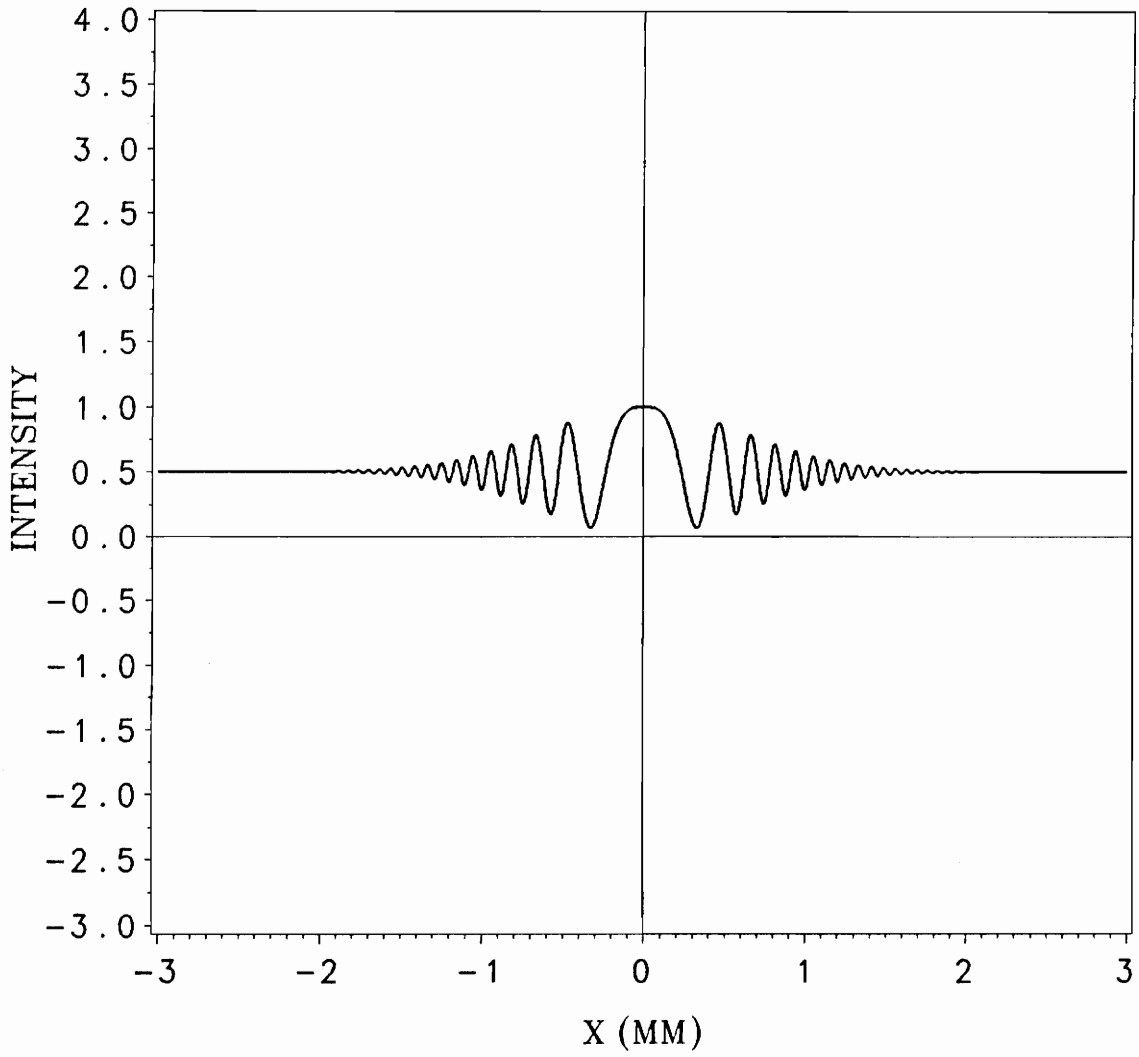

Figure 10. Cross section of a point source hologram: (generated with $\omega_u = 40\mu m$).

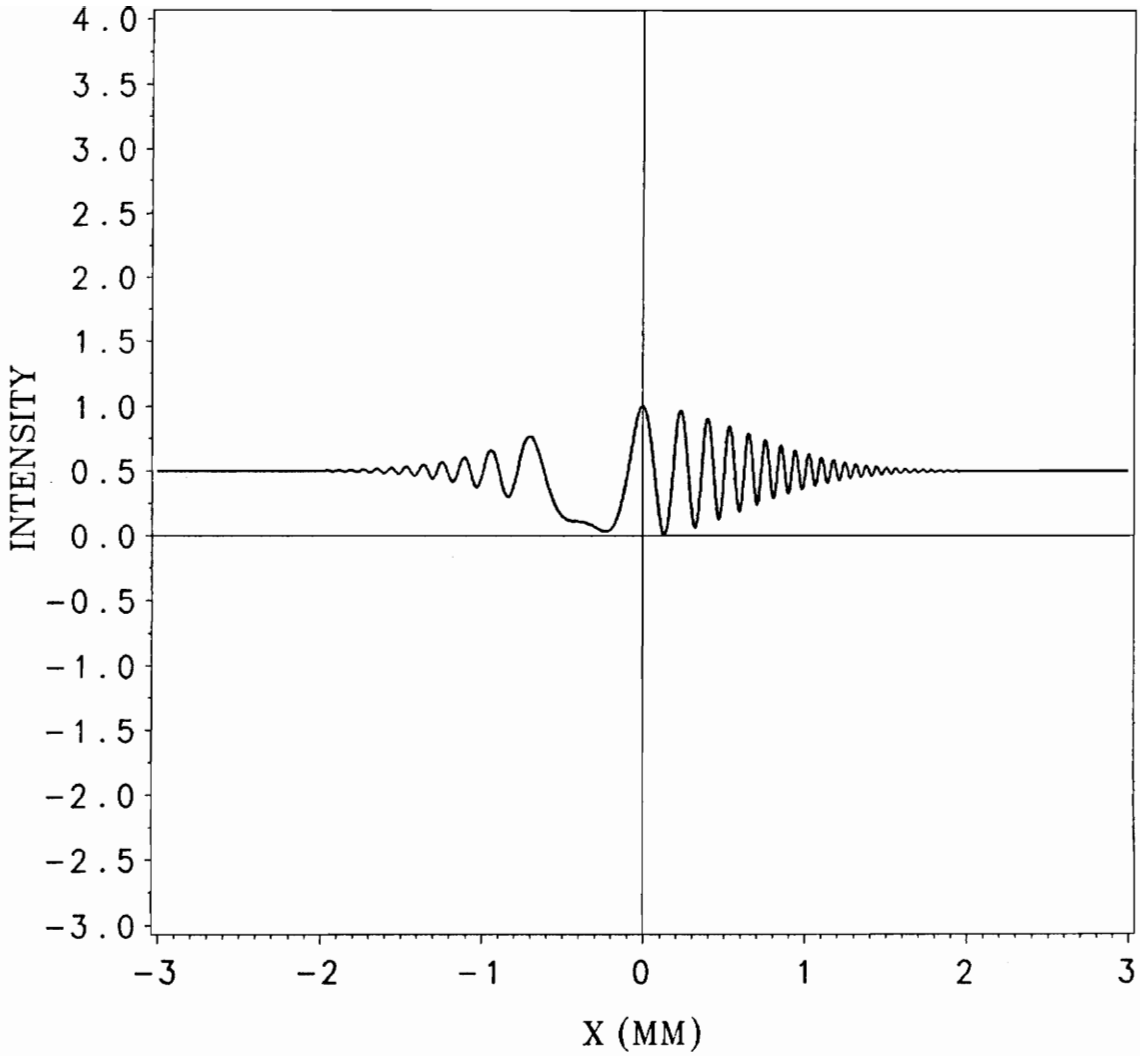

Figure 11. Cross section of a point source hologram: (with a small spatial carrier frequency included when $\omega_u = 40\mu m$).

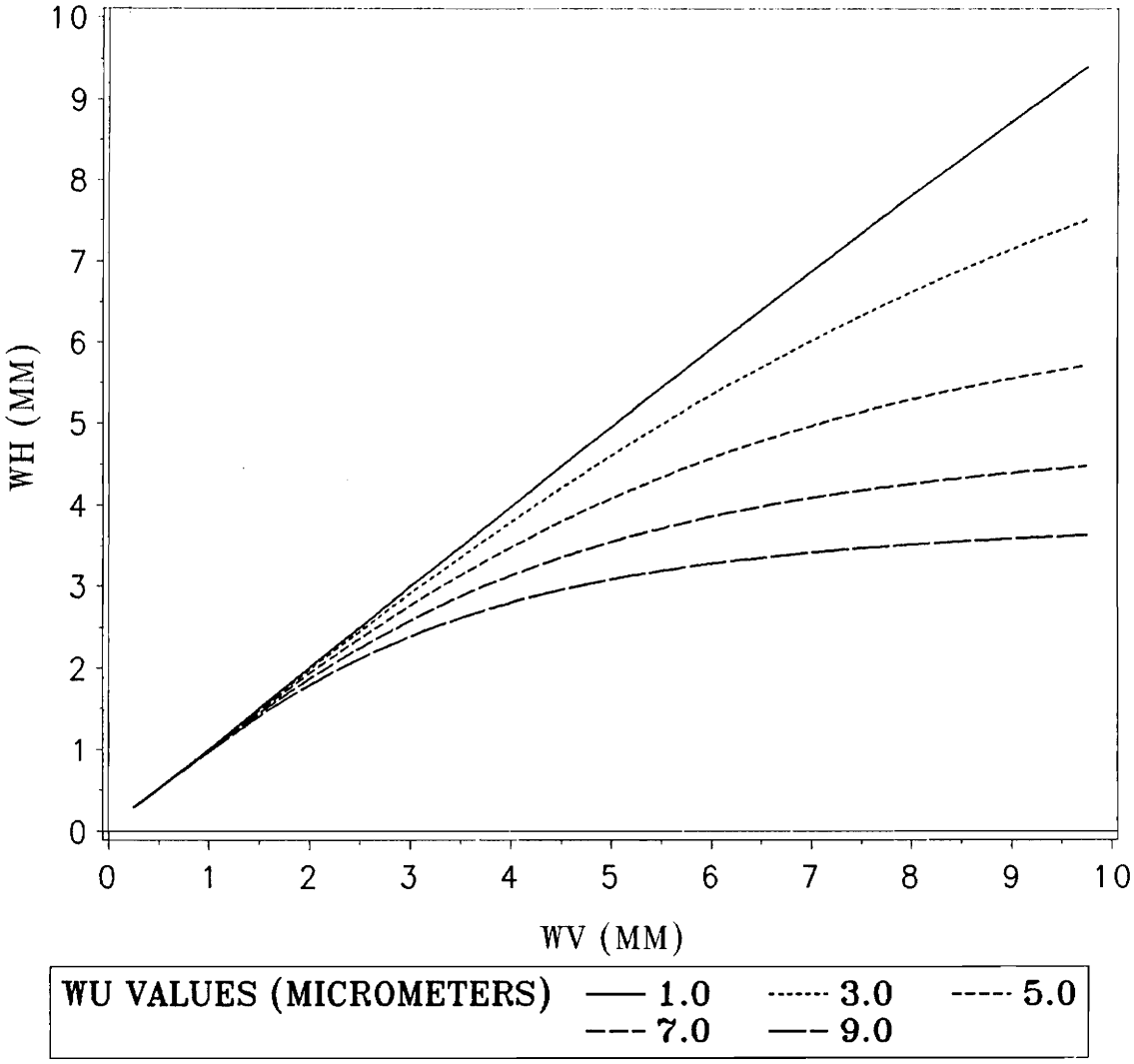

Figure 12. Point source hologram width: (as a function of ω_u and ω_v with $\omega_u << \omega_v$).

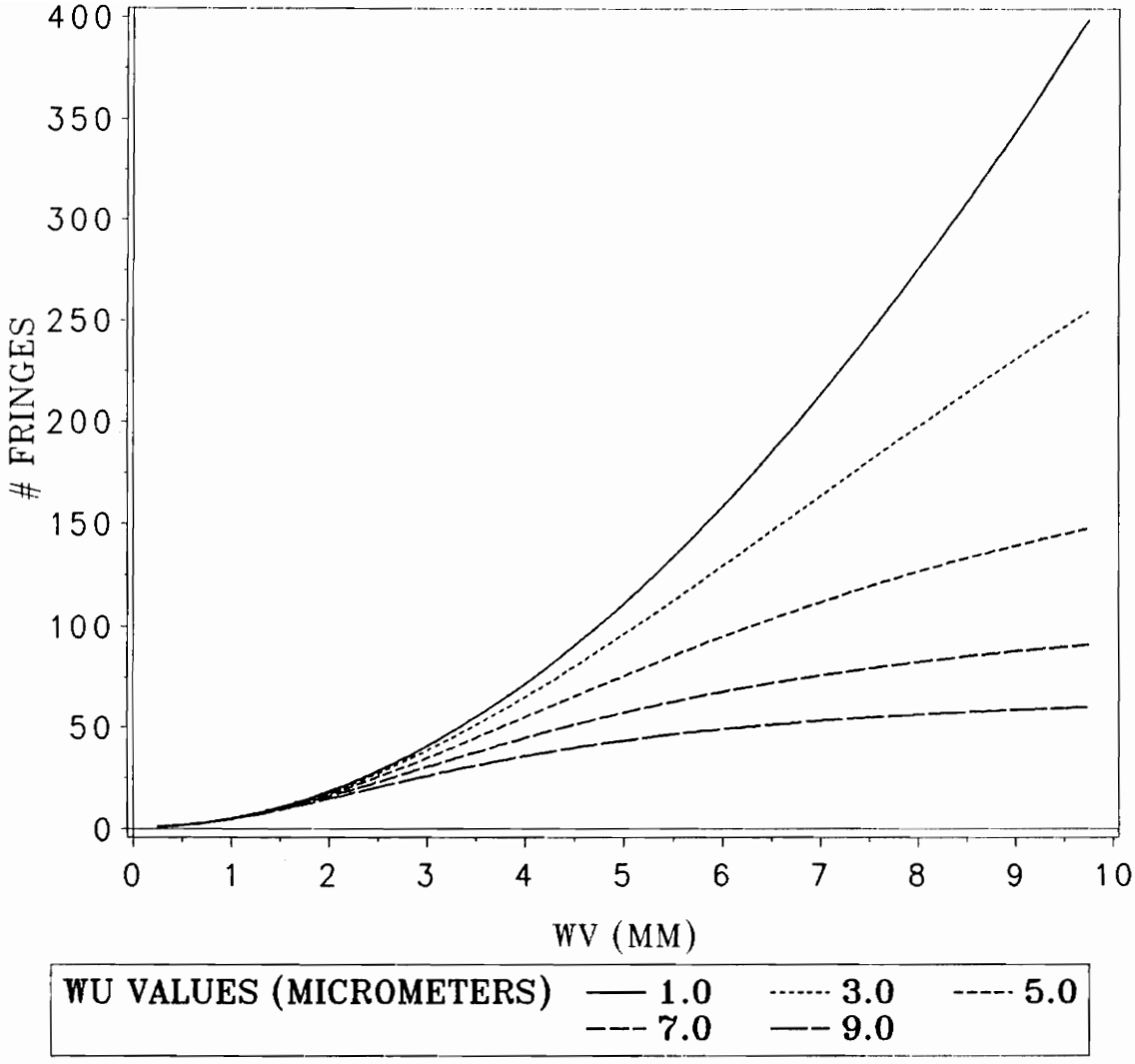

Figure 13. Number of fringes in a point source hologram: (to the 1/e point, as a function of ω_u and ω_v with $\omega_u << \omega_v$).

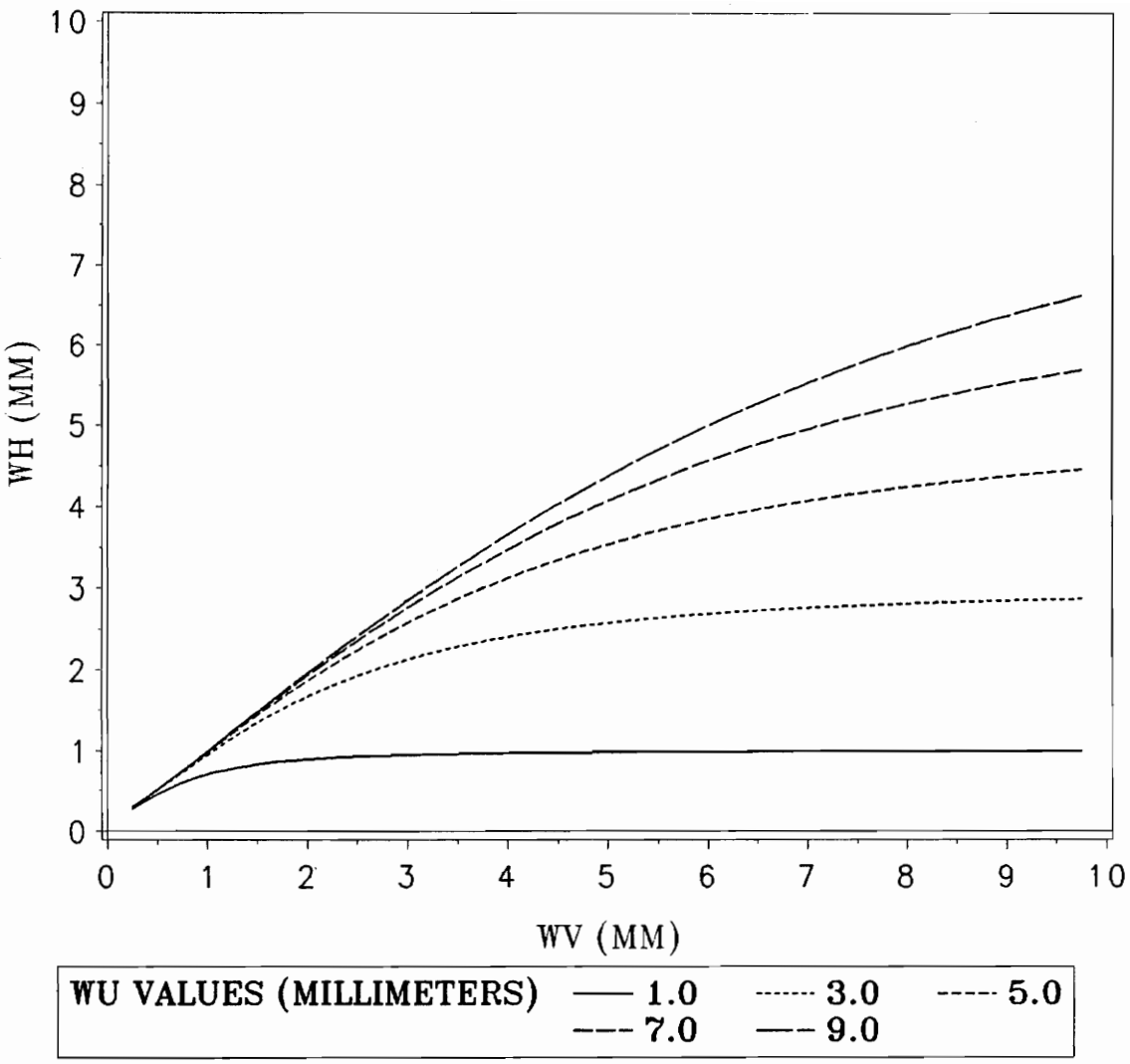

Figure 14. Point source hologram width: (as a function of ω_u and ω_v with $\omega_u \simeq \omega_v$).

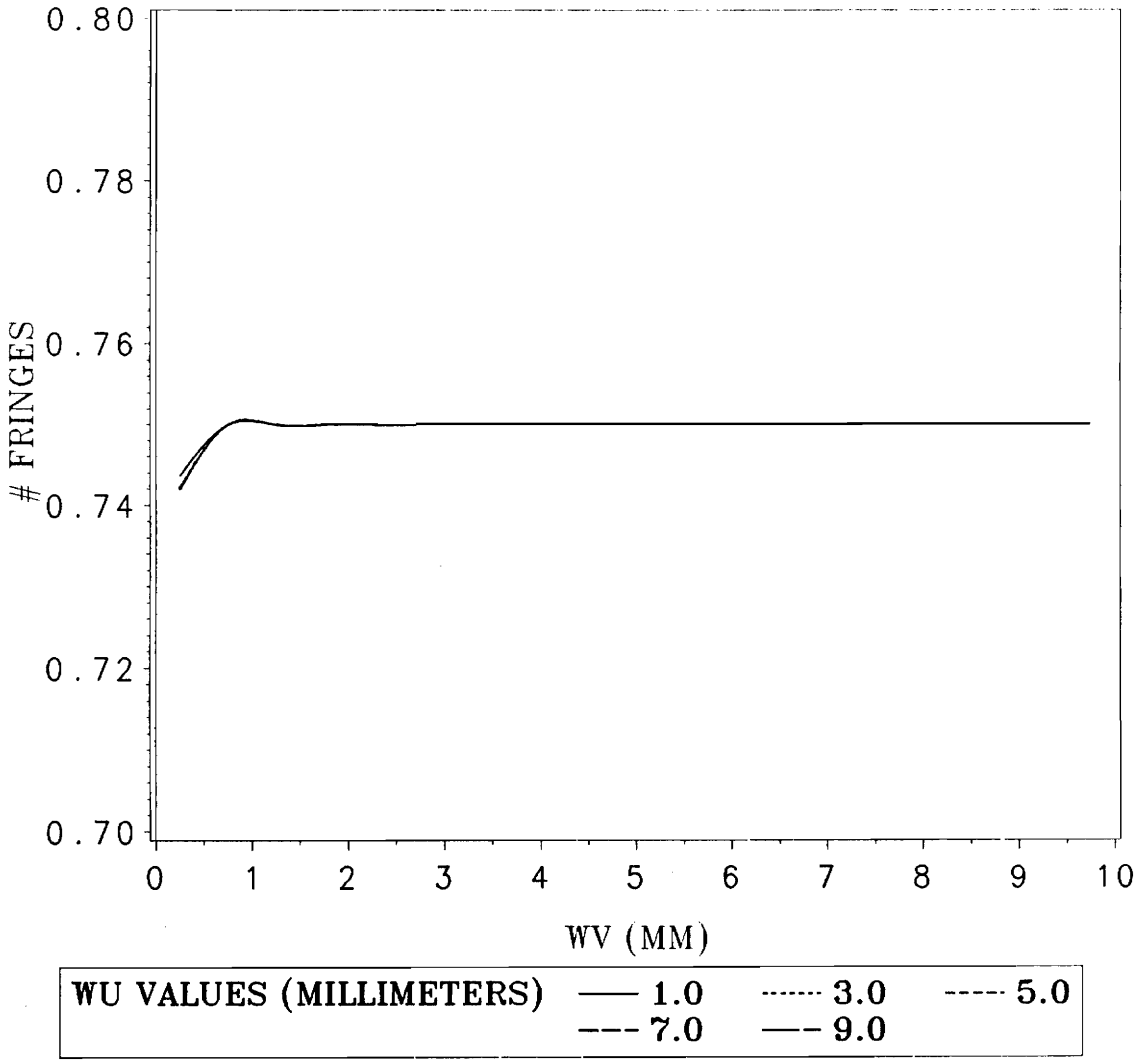

Figure 15. Number of fringes in a point source hologram: (to the 1/e point as a function of ω_u and ω_v with $\omega_u \simeq \omega_v$).

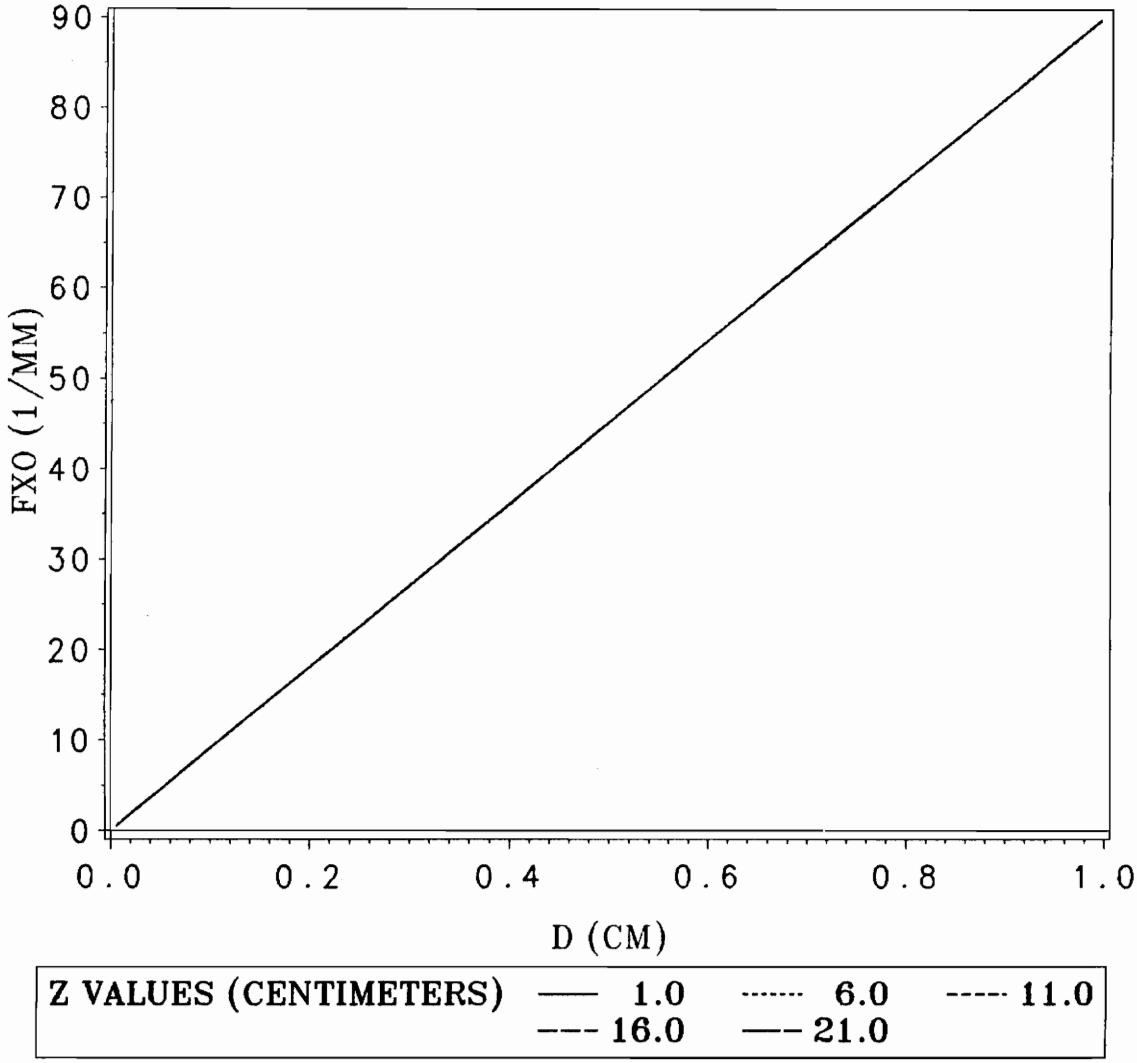

Figure 16. Spatial carrier frequency: (as a function of the interferometer misalignment factor D).

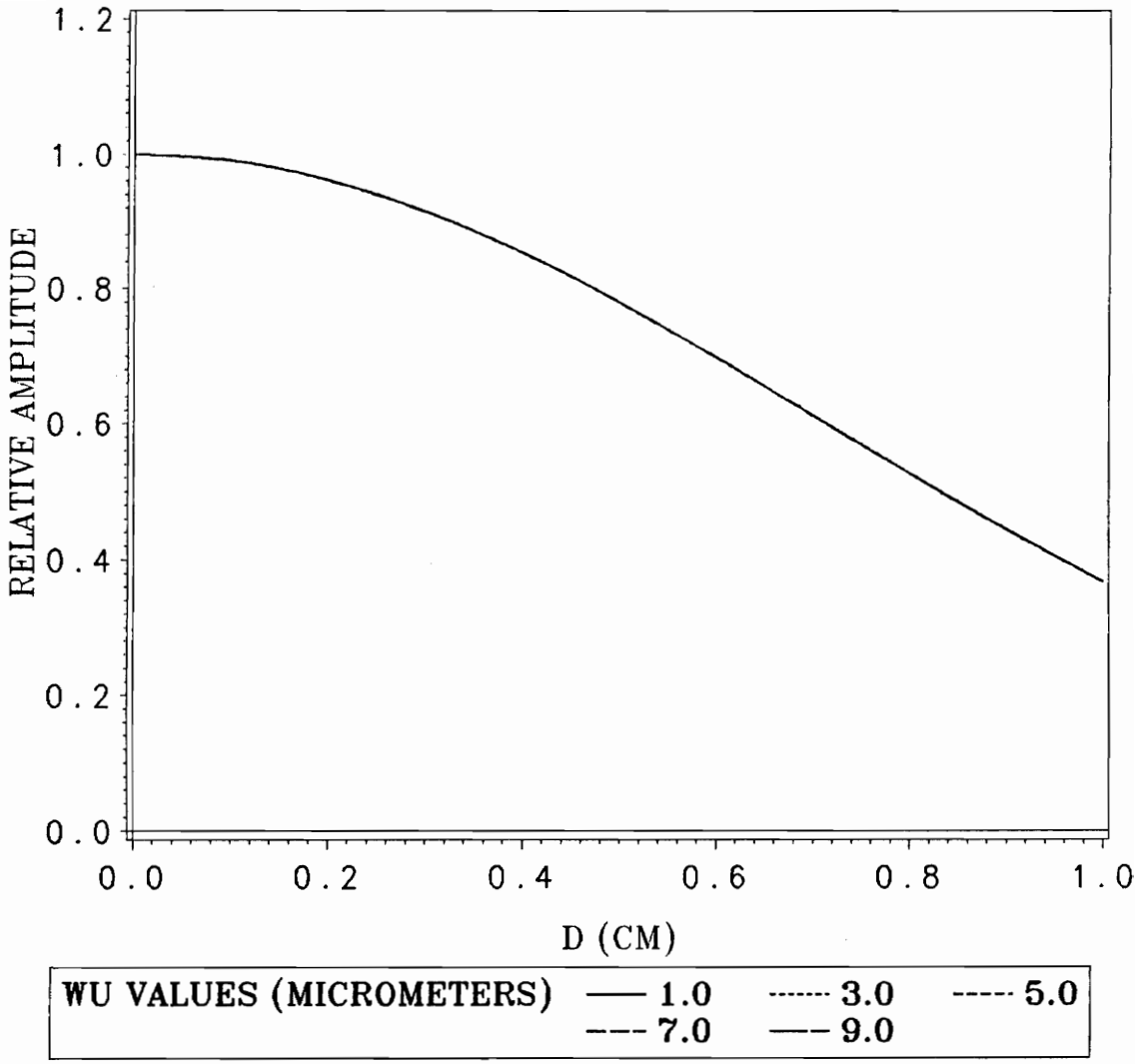

Figure 17. Relative OTF amplitude: (as a function of the interferometer misalignment factor D).

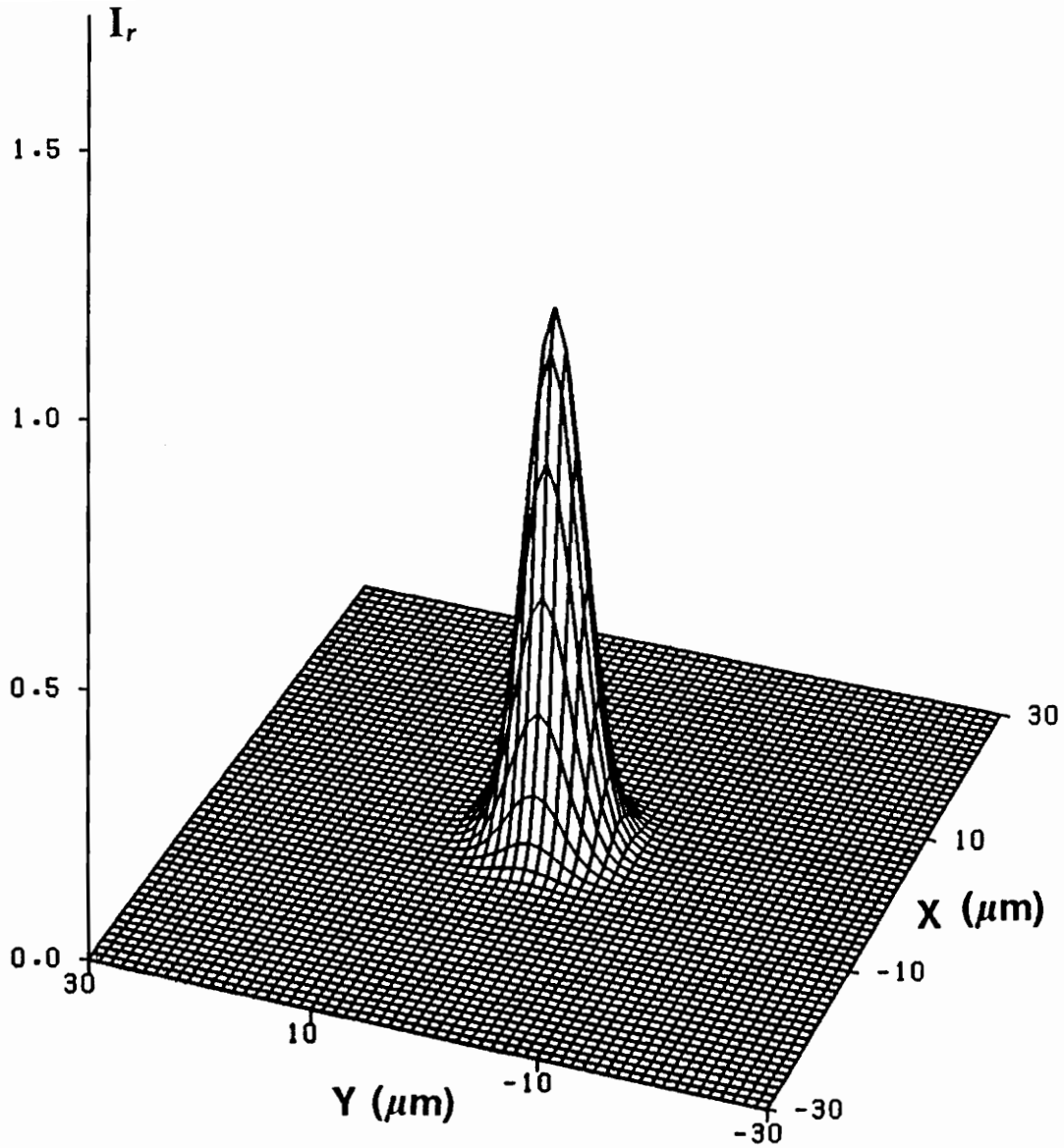

Figure 18. Point source hologram reconstruction: (when $\omega_u = 3.526\mu m$ and the intensity has been normalized to unity).

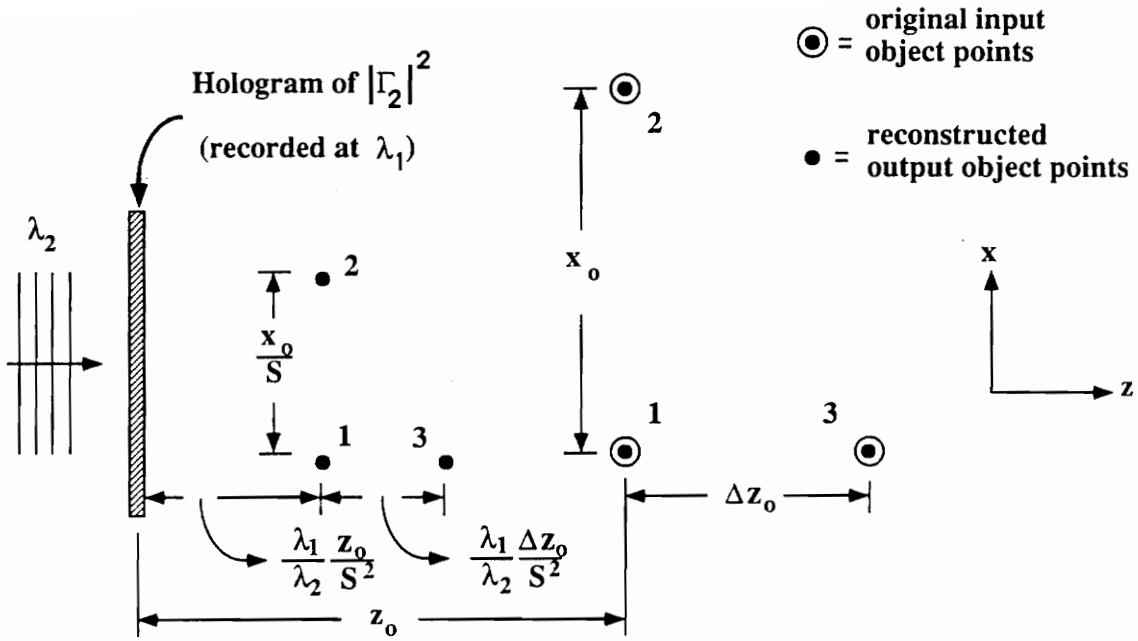

Figure 19. Overlay of input and reconstructed objects: (to demonstrate holographic magnification when $S \geq 1$).

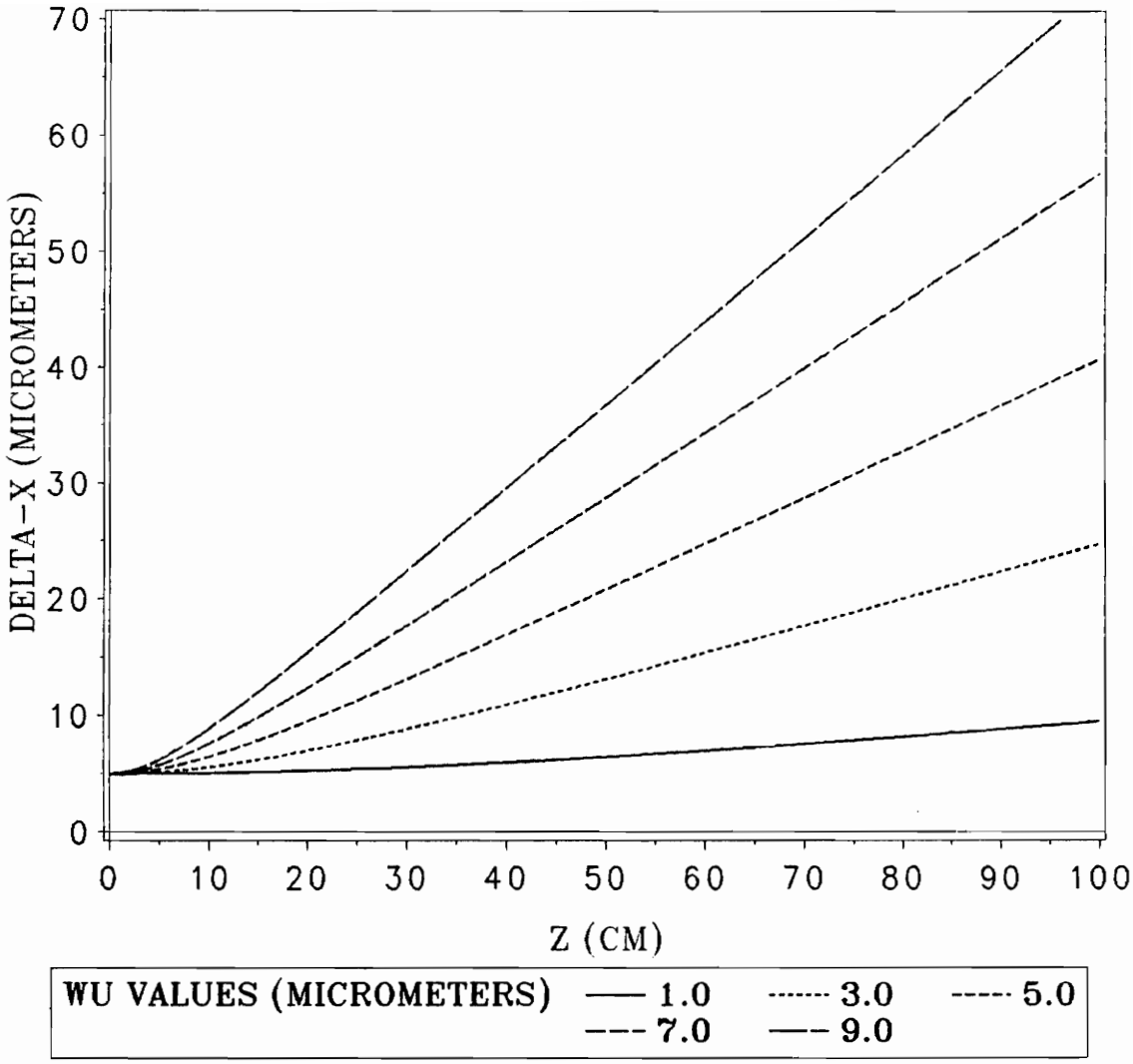

Figure 20. Lateral resolution: (Δx as a function of ω_u and the depth parameter z).

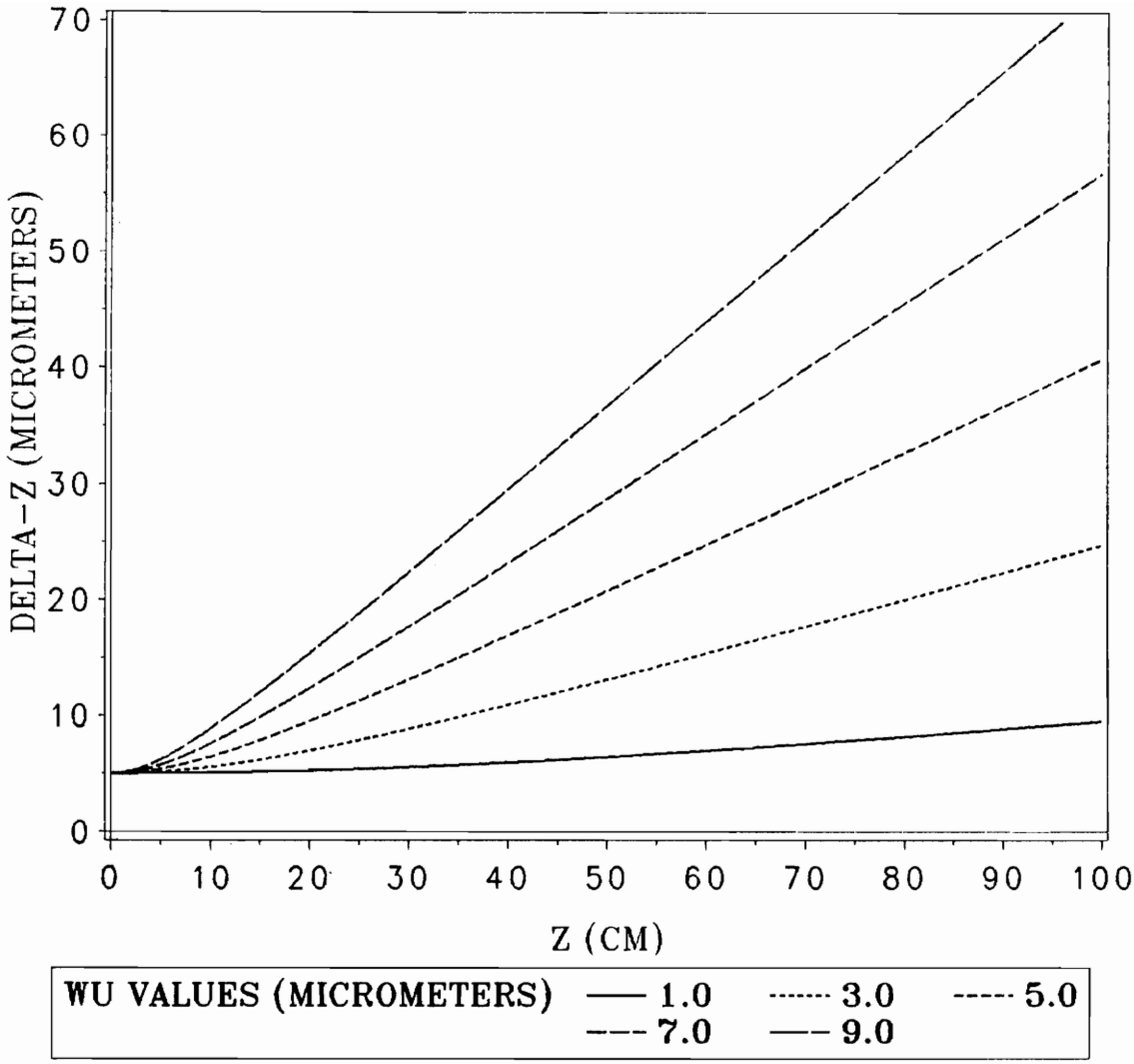

Figure 21. Longitudinal resolution: (Δz as a function of ω_u and the depth parameter z, with scale factor S = 1).

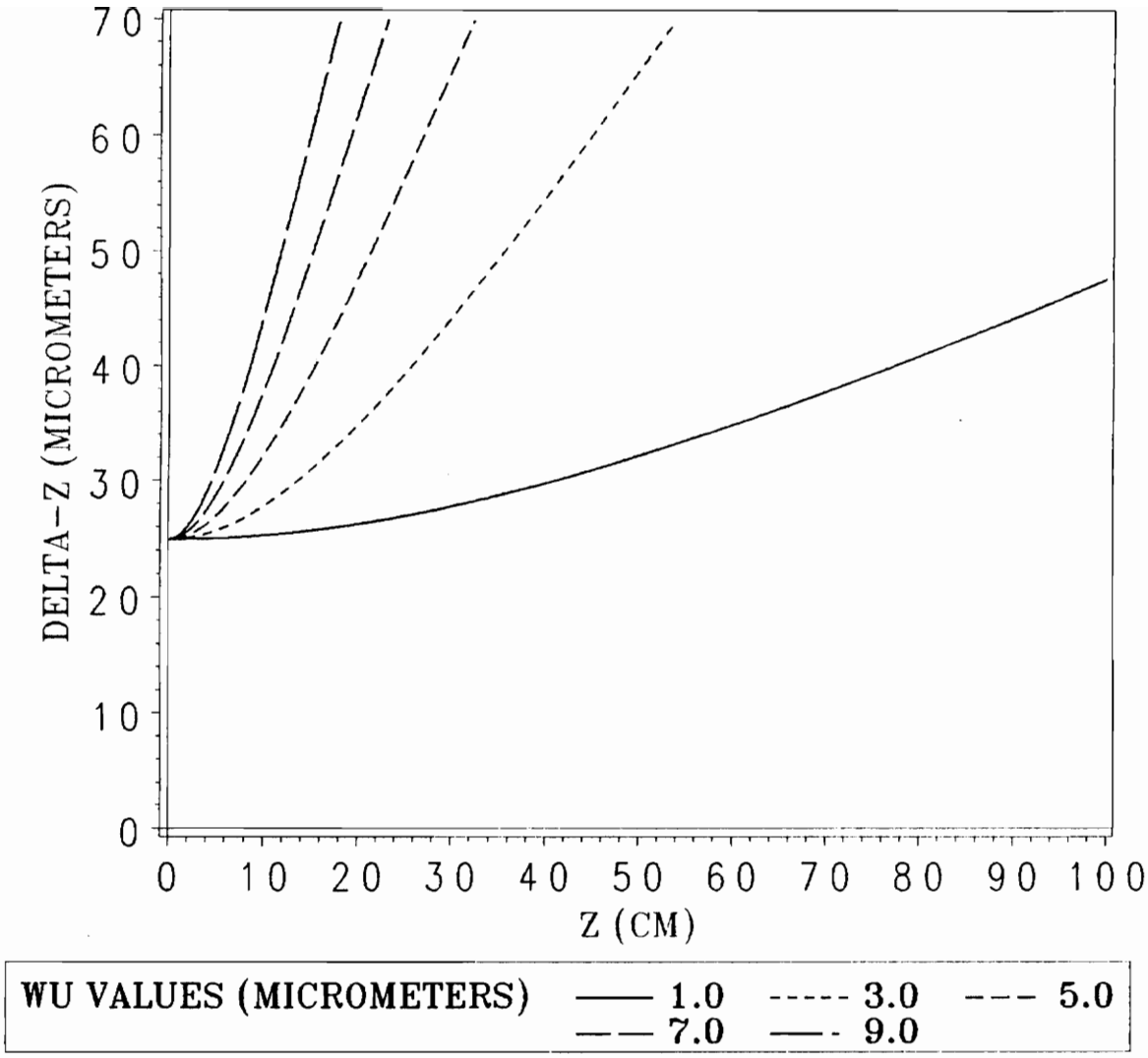

Figure 22. Longitudinal resolution: (Δz as a function of ω_u and the depth parameter z, with scale factor S = 5).

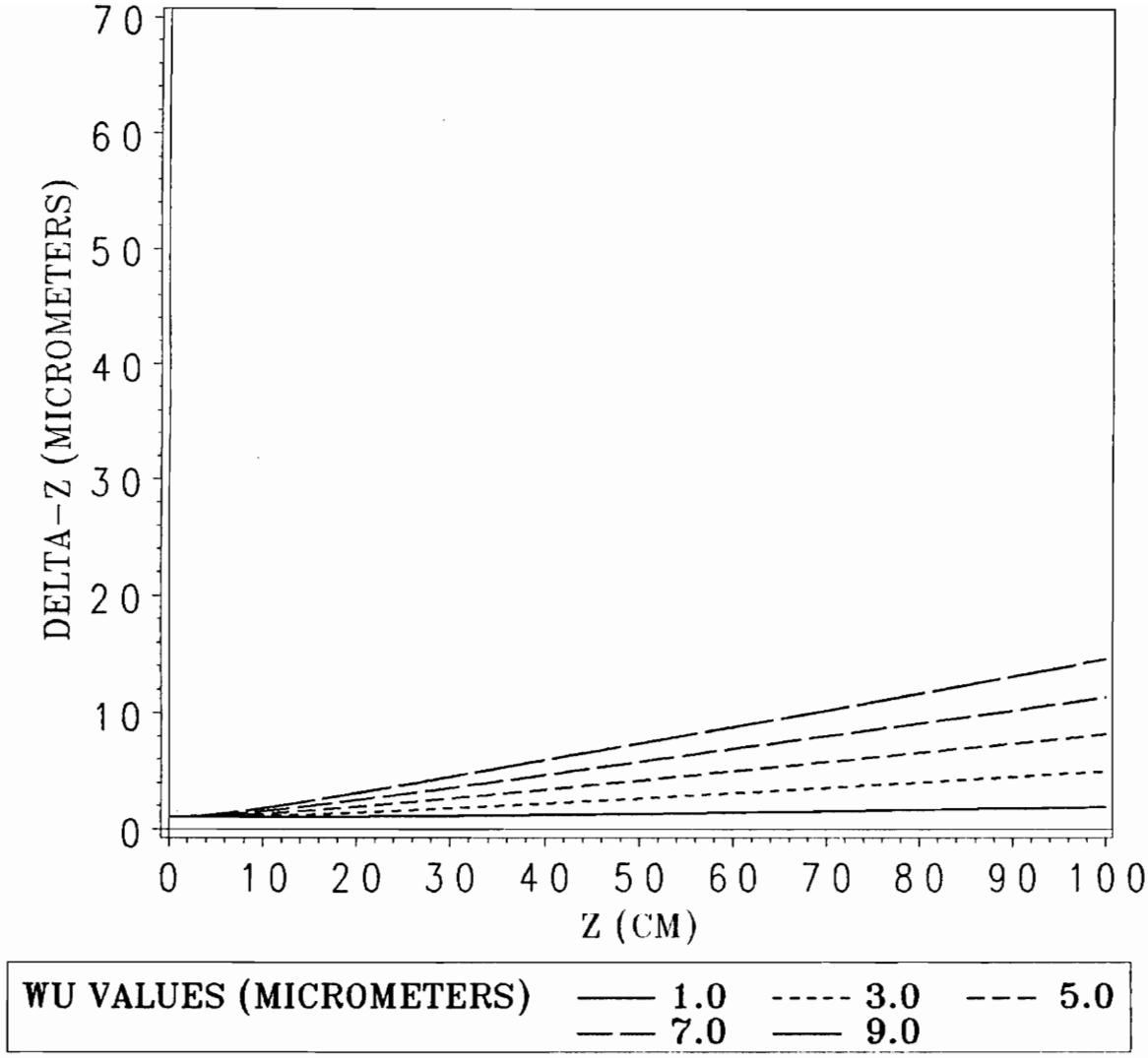

Figure 23. Longitudinal resolution: (Δz as a function of ω_u and the depth parameter z, with scale factor S = 0.2).

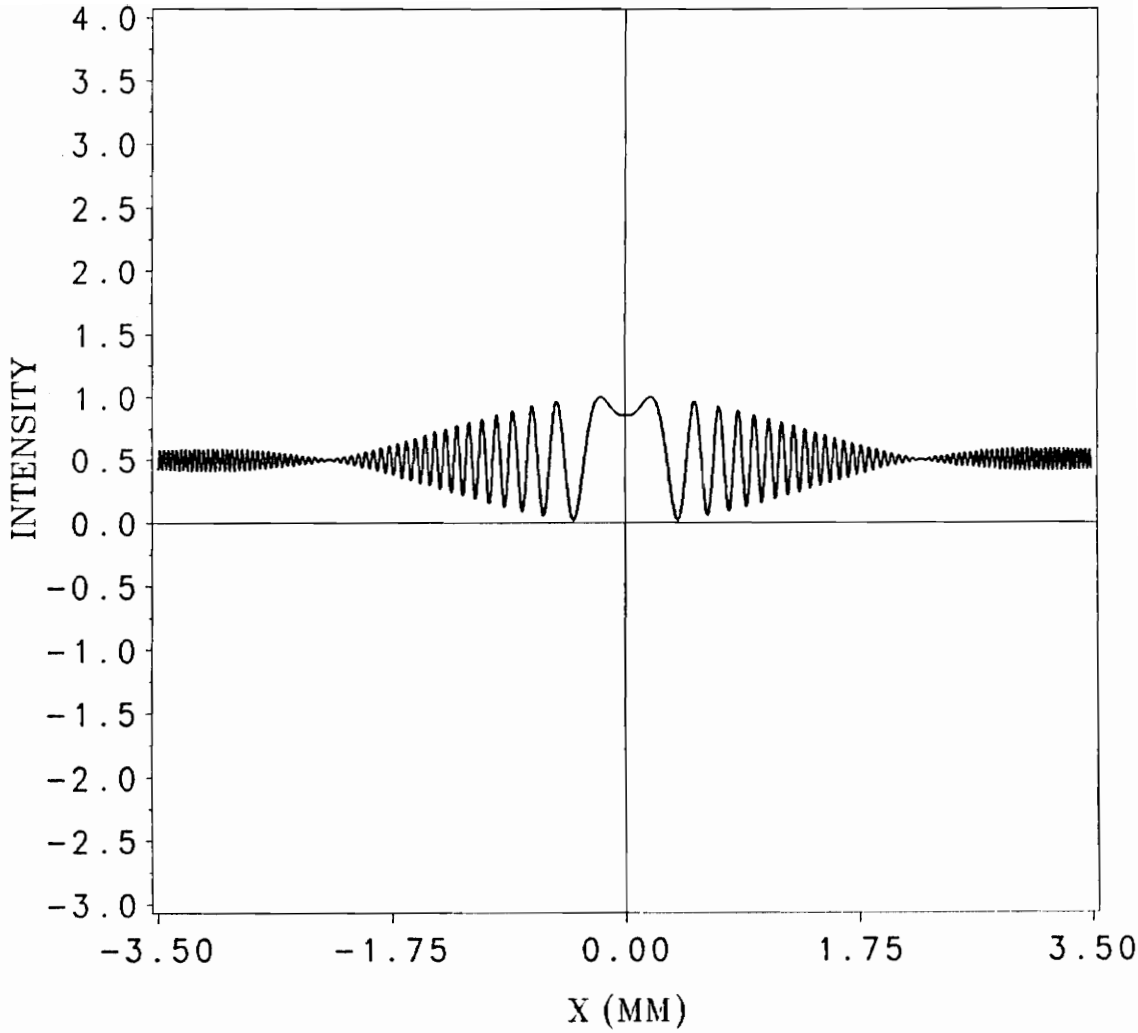

Figure 24. Simulated hologram cross section of a 50 micrometer slit.

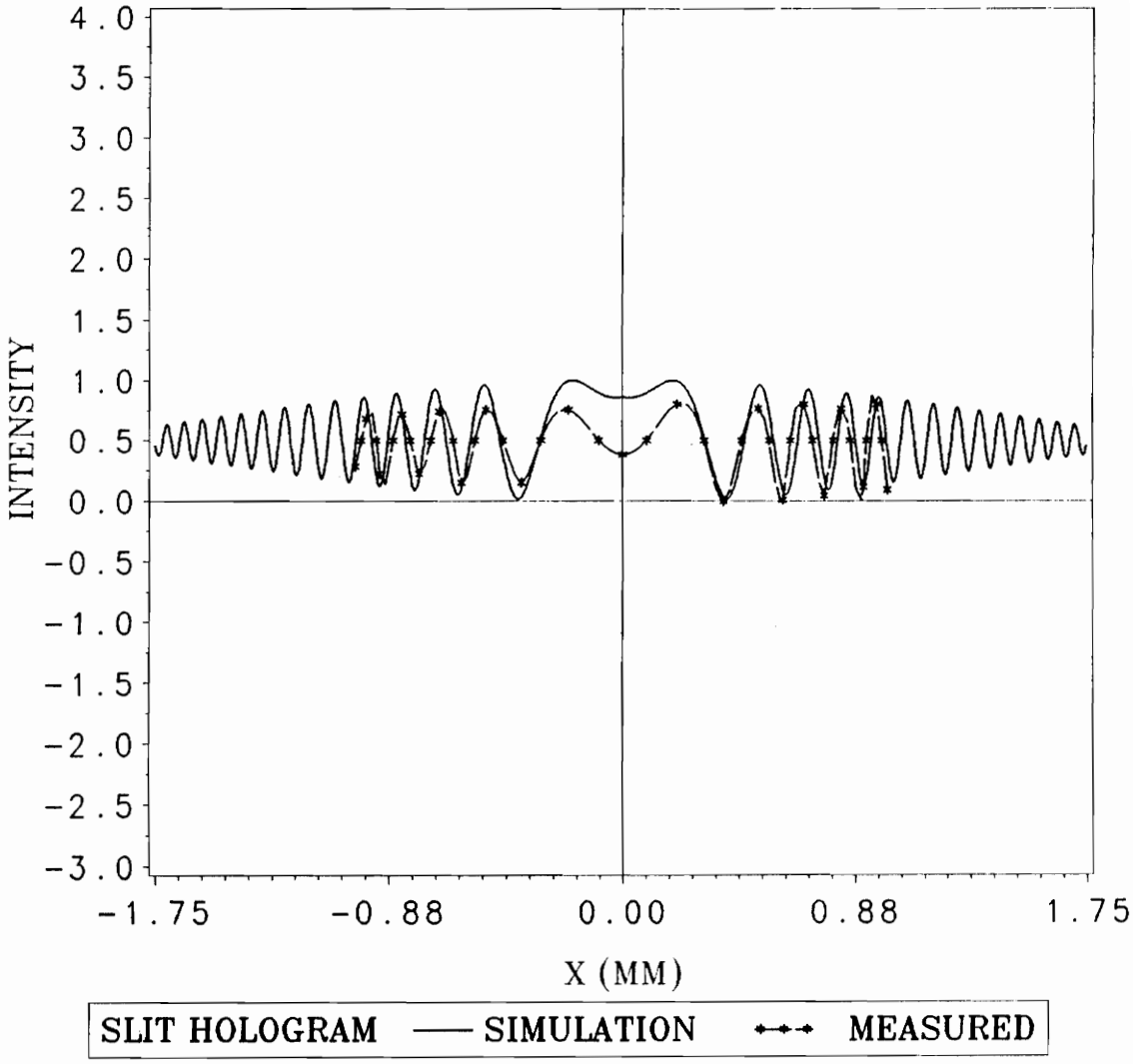

Figure 25. Simulated and experimentally measured hologram: (crossection of a 50 μm slit).

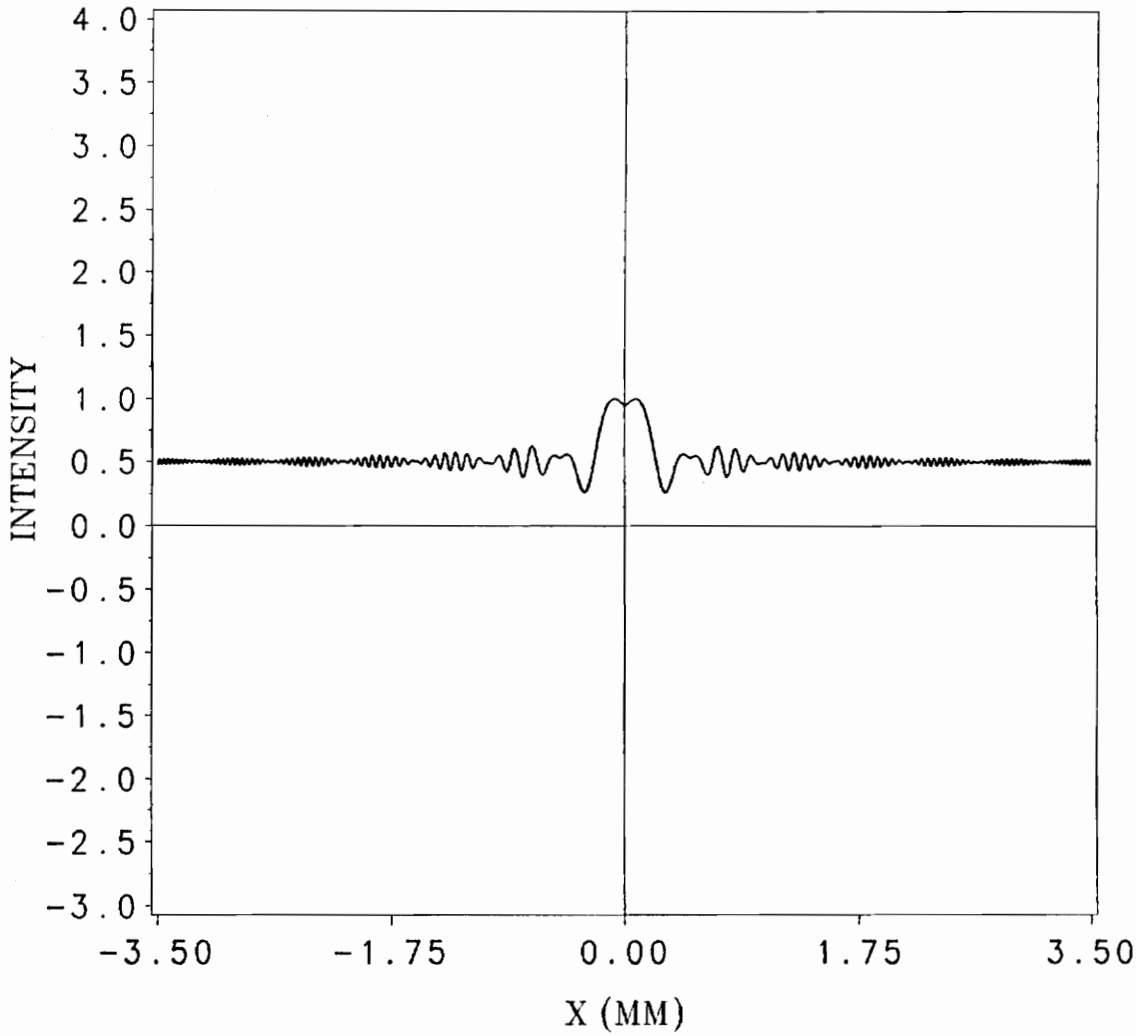

Figure 26. Simulated hologram cross section of a 200 micrometer slit: (demonstrating background light accumulation).

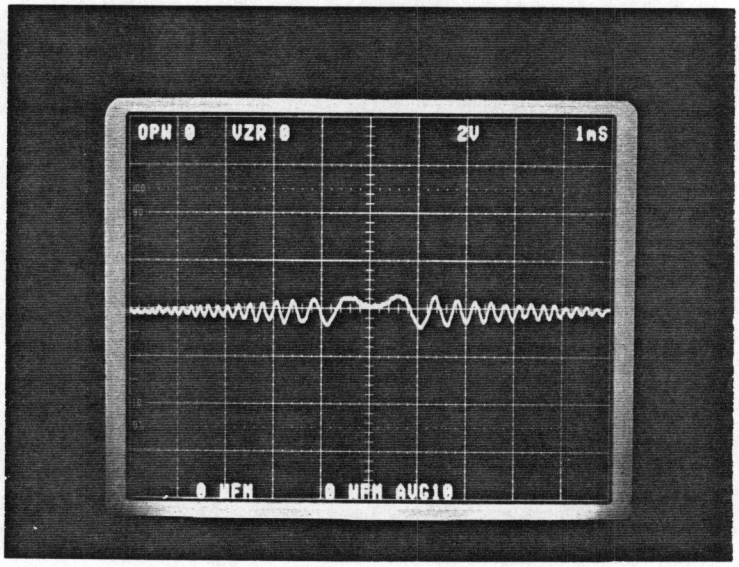

(a)

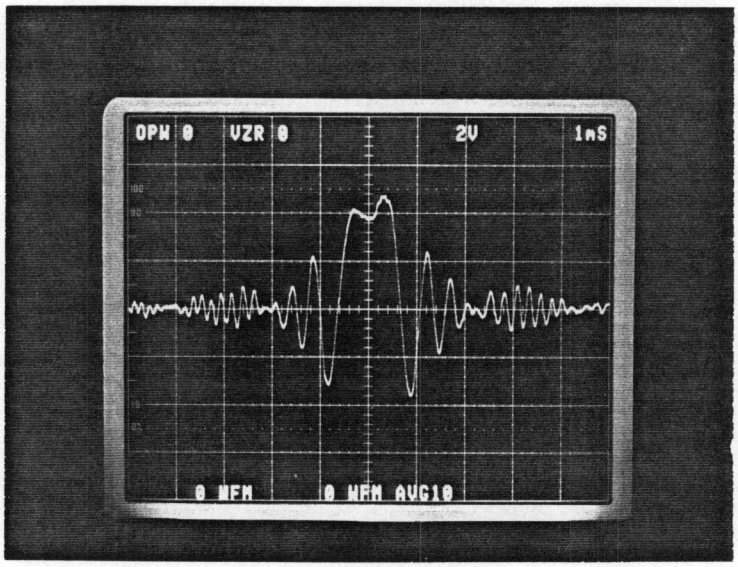

(b)

Figure 27. Experimentally measured slit hologram cross sections: a) 50 μm x 1.0 cm, b) 115.5 μm x 1.0 cm.

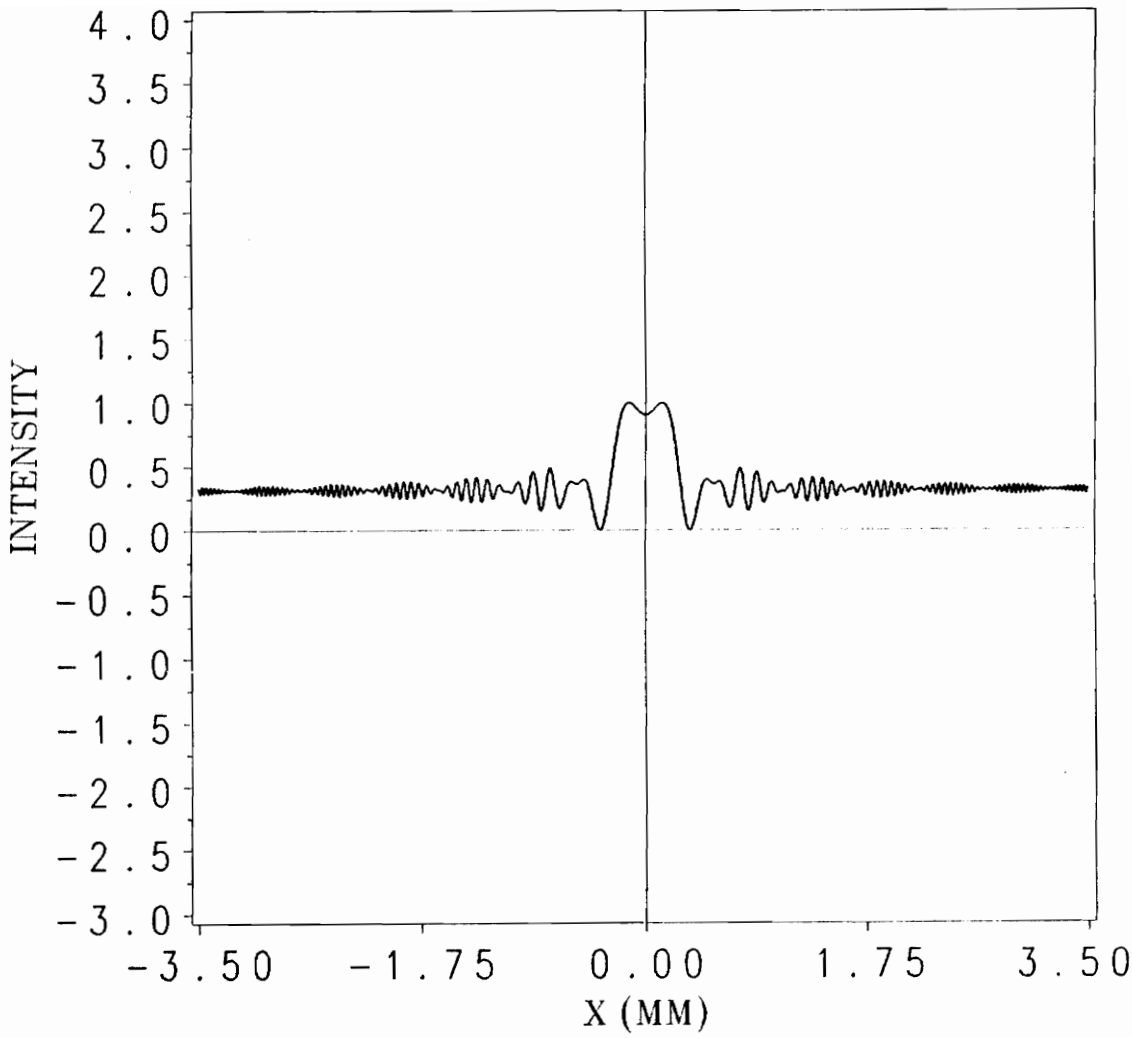

Figure 28. Simulated hologram cross section of a 200 micrometer slit: (demonstrating bias buildup reduction and increased fringe contrast).

4.0 RECONSTRUCTION OF SCANNED OPTICAL HOLOGRAMS

In this chapter the principles of real-time optical holography are presented as they relate to the active heterodyne scanning (recording) technique used in conjunction with holographic reconstruction methods employing an electron beam addressed spatial light modulator (EBSLM) [8]. Results of experiments performed to verify these principles are also presented [10].

4.1 Principles of Real-Time Optical Scanning Holography

In this section the techniques by which holographic recording and reconstruction can be achieved using the heterodyne scanning image processor in conjunction with an EBSLM [9,32] are described. To begin, a brief description of the EBSLM and a discussion of its application

as a real-time display device in holographic reconstruction is presented [10]. This is followed by a description of the spatial frequency resolution capabilities of the EBSLM, after which the overall incoherent point spread function (PSF) of the recording/reconstruction system is developed. Finally, based on the calculated PSF, the size of the reconstructed real image of a simple slit object is predicted so as to provide a basis of evaluation for experimental measurements presented in the following section. (It should be noted that though methods of recording carrier frequency (off-axis) holograms were proposed and analyzed for the scanning image processor in the previous chapter [5,33], the discussions in this chapter will be limited to on-axis holographic methods (i.e., $d = f_o = 0$ in equation (3.1.5)), as only on-axis holograms have been produced and evaluated experimentally.)

4.1.1 Electron beam addressed spatial light modulator

A schematic diagram of the EBSLM as it is used in a coherent light conversion system is shown in Figure 29 [9,32]. As seen, a serial video signal is the required input to the EBSLM controller (Hamamatsu model # C3737). The controller in turn provides the signal which intensity modulates the emission from the electron gun within the EBSLM head (Hamamatsu model # X3636). This electron beam is then two-dimensionally scanned onto the surface of a 55-degree cut $LiNbO_3$ crystal with a deflection coil. As a result, electric charges accumulate on the surface of the crystal. Through the Pockels effect then, the field associated with the charges changes the refractive index of the crystal on a point-by-point basis. To read out these results, a linearly polarized laser is used to illuminate the crystal from an external source. In the coherent light conversion technique, a pointwise varying elliptical polarization due to the corresponding pointwise change in refractive index change of the crystal is

manifest within the reflected light. By passing this reflected light through an analyzer, a converted coherent image is obtained [9].

In order to display a holographic image generated through the scanning process described in chapter 3, an arrangement such as that shown in Figure 30 is used. In this set-up, a storage oscilloscope is used as an intermediate display device. This is accomplished by feeding the x and y scanning signals driving the scanner of Figure 4 in parallel to the external trigger and vertical amplifier inputs of the oscilloscope, respectively, while also feeding the electrical signal v(x,y;z) (see equations (3.1.5) and (3.2.6)) corresponding to the scanned hologram into the intensity modulating input (z-axis) of the oscilloscope. In this way the electron gun of the oscilloscope is synchronized with the x and y scanning rates of the scanner of Figure 4 and the hologram is mapped in a two-dimensional fashion onto the oscilloscope screen. A closed circuit television (CCTV) camera then views the hologram on the oscilloscope and provides a serial video signal output which is in turn amplified and sent to the EBSLM controller.

We mention that this intermediate display step is necessary because, in general, the rate at which an object is scanned with the heterodyne scanning image processor does not correspond to video standards. In fact, in most of the experimental work, objects are scanned very slowly so as to reduce mechanical jitter which tends to introduce undesirable phase noise into the Mach-Zehnder interferometer type configuration shown in Figure 4. We also mention that after being written onto the EBSLM, the hologram in essence appears as a coherently back illuminated transmitance function in the plane of the analyzer of Figure 30. The reconstructed real object image then can be found a distance zM_{long} in front of the analyzer, where z is the distance, shown in Figure 4, at which the object $|\Gamma_2|^2$ is initially scanned and M_{long} is the longitudinal magnification of the holographic imaging system (see equation (3.2.31)) arising from various scaling factors which will be discussed later.

In order to investigate the spatial frequency resolution of the EBSLM, the CCTV camera was used to "look" directly at a linear chirp grating. The image of this grating was then written

onto the EBSLM and viewed on a smoked glass screen placed just after the analyzer of Figure 29. Using a magnifying eye loupe with a reticle graduated in 50 micrometer increments, it was observed that under optimum conditions the lines on the image of the chirp grating became barely distinguishable when the separation between the lines was between 150 - 200 micrometers. This translates to a spatial resolution of between 5 - 6.6 lp/mm. In order to verify that the EBSLM was the limiting factor in this measurement, the output of the CCTV camera was displayed directly on a video monitor. As expected, the most closely spaced lines on the chirp grating were easily resolved on the video monitor screen, indicating that the CCTV camera did not influence the observed SLM resolution. In the next subsection we will show how this resolution limit affects reconstructed holographic images.

4.1.2 The overall point spread function

In order to develope the incoherent point spread function (PSF) for the overall holographic recording/reconstruction system, consider that an on-axis hologram is recorded for a single point object; that is, $|\Gamma_2|^2 = \delta(x,y)$. From equation (3.1.5) the recorded point source hologram can then be written as

$$v(x,y;z) = V_{DC} + \frac{1}{2}\mathcal{F}^{-1}\{OTF(f_x, f_y;z)\} + \frac{1}{2}\left[\mathcal{F}^{-1}\{OTF(f_x, f_y;z)\}\right]^* \quad , \qquad (4.1.1)$$

where the OTF is given as in equation (3.2.6) when d=K=H=0 and we recall that $A + A^* = 2Re\{A\}$. Simplifying equation (4.1.1) yields

$$v(x,y;z) = V_{DC} + \frac{1}{2}\tilde{V}_\delta + \frac{1}{2}\tilde{V}_\delta^* \quad , \qquad (4.1.2)$$

where $\tilde{V}_\delta$ is given in equation (3.2.8), again when d = K = H = 0. As in conventional holography, equation (4.1.2) represents, in essence, the effects of three lenses. The first term of equation (4.1.2) represents a flat lens with focal plane at infinity. The second and third terms correspond, respectively, to positive and negative lenses of focal length $f_\delta = z$, under unity magnification (i.e., the distance at which the hologram was originally recorded - see equations (3.2.8) and (3.1.8) for Gaussian beam and standard plane and spherical wave formulations of $\tilde{V}_\delta$, respectively), which upon reconstruction yield the real and virtual images of the reconstructed point object.

As it is easier to experimentally investigate the reconstructed real image, only this image will be discussed in further analyses. Using the second term of equation (4.1.2) then, the reconstructed real image intensity $I_{r\delta}$ is written as

$$I_{r\delta} \simeq \left| F^{-1}\left[F\left\{ \mathrm{circ}\left(\frac{r}{a}\right) \exp\left(-\frac{r^2}{\omega_I^2} \right) \tilde{V}_\delta(x,y;z) \right\} H_z \right] \right|^2 , \tag{4.1.3}$$

where the beam illuminating the hologram in the reconstruction process is assumed to be a broad, collimated real Gaussian (i.e., ω_I is large with respect to a) and where the circular apodization is included to account for the limited number of fringes, or Fresnel zones, available to contribute to the reconstruction process; the limited number of fringes being in turn due to the limited spatial resolution of the EBSLM. Note that in equation (4.1.3) it is assumed that the EBSLM has the same spatial resolution in all radial directions. In addition, note that, mathematically, circ(r/a) is defined as

$$\mathrm{circ}\left(\frac{r}{a}\right) = \begin{cases} 1; & r \le a \\ 0; & r > a \end{cases} , \tag{4.1.4}$$

where $r = \sqrt{x^2 + y^2}$ and a is in practice limited to the radial size of the EBSLM crystal (in our case the crystal diameter is about 1.2 cm). Finally, H_z in equation (4.1.3) represents the spatial *transfer function* of equation (3.1.21), rewritten here as

$$H_z = \exp\left(-j\pi\lambda z\left(f_x^2 + f_y^2\right)\right) \quad , \tag{4.1.5}$$

where an nonessential constant has been left out and where z is the propagation distance to the reconstruction plane of the field emerging from the illuminated hologram, and exactly equals (under unity magnification) the distance at which the point object leading to equation (4.1.2) was originally scanned. We thus recognize equation (4.1.3) as the overall incoherent PSF for the scanning holographic imaging system. In general, though, the form of equation (4.1.3) must be investigated through numerical simulations. Such simulations will be presented shortly; however, we must first further investigate the circ(r/a) function and determine how it is influenced by the EBSLM resolution.

The instantaneous spatial frequency ρ at any radial location from the origin can be determined for a FZP by first identifying the phase term of $\tilde{V}_\delta$ by rewriting equation (3.2.8) under on-axis assumptions as

$$\tilde{V}_\delta = \frac{1}{G}\exp\left(-\pi^2 Re\left\{\frac{1}{G}\right\}\left(\frac{r}{M}\right)^2\right)\exp(-j\,\Phi_\delta) \quad , \tag{4.1.6}$$

where

$$\Phi_\delta = \pi^2\, Im\left\{\frac{1}{G}\right\}\left(\frac{r}{M}\right)^2 \tag{4.1.7}$$

and the factor M has been included to account for any magnification of the FZP which would occur during the recording and display process. (We introduce this magnification factor now simply because it is convenient to do so, though, a detailed discussion of the precise mechanisms leading to holographic magnification will be deferred to the following,

experimental section. Notice also that the magnification factor M exactly equals 1/S, where S is the scaling factor introduced in section 3.2.2.) The instantaneous spatial frequency ρ is then found to be

$$\rho = \frac{1}{2\pi}\frac{\partial \Phi_\delta}{\partial r} = \frac{\pi\, r\, \mathrm{Im}\left\{\frac{1}{G}\right\}}{M^2} \quad [m^{-1}] \quad . \tag{4.1.8}$$

Generally speaking then, the value of the parameter a in equations (4.1.3) and (4.1.4) is found by setting r=a in equation (4.1.8) while ρ is set equal to the spatial resolution of the EBSLM. That is,

$$a = \frac{\rho\, M^2}{\pi\, \mathrm{Im}\left\{\frac{1}{G}\right\}} \quad . \tag{4.1.9}$$

We thus see that the effective size of a point source hologram displayed on an EBSLM is directly proportional to the EBSLM spatial resolution, where by *effective* we mean to indicate that due to the limited available spatial resolution, the size a of the displayed hologram can be less than the size of the EBSLM crystal.

It is also of interest to estimate the number of observable fringes expected in a displayed FZP as a function of EBSLM resolution. Using the imaginary (oscillatory) term of equation (4.1.6), the location r_n of the nth fringe (or maximum) is found to be

$$r_n = \sqrt{\frac{2n\pi\, M^2}{\pi^2\, \mathrm{Im}\left\{\frac{1}{G}\right\}}} \quad [m] \quad ; n = 0,1,2... \quad , \tag{4.1.10}$$

where n=0 corresponds to the central maximum. Setting $r = r_n$ in equation (4.1.8) and rearranging terms we then find that the number n of observable fringes as a function of ρ is simply

$$n = \frac{\rho^2 M^2}{2\pi \, Im\left\{\frac{1}{G}\right\}} \quad , \tag{4.1.11}$$

where, strictly speaking, one must round n to the next lowest integer. For example, in our work $\omega_u = 3.526\,\mu m$, $\omega_v = 1.0\,cm$, $z = f_2 = 17.5\,cm$ and $\lambda = 633\,nm$. In addition, the characteristic size of the reconstruction beam was $\omega_I = 3.0\,cm$ and the maximum spatial resolution of the EBSLM was specified by the manufacturer to be 20 lp/mm [9]. Using these parameters we find under unity magnification (M = 1) that

$$\begin{aligned} Im\left\{\frac{1}{G}\right\} &= 2.8735 \times 10^6 \ [m] \\ a &= 2.215 \ [mm] \end{aligned} \quad , \tag{4.1.12}$$

and

$$n = 22 \, fringes \quad , \tag{4.1.13}$$

where, as discussed in section 3.2.1, the choice of $z = f_2$ was made because in actual experiments, at $z = f_2$ (see Figure 4) the collimated and diverging beams coinciding at $|\Gamma_2|^2$ most completely and uniformly overlap - yielding optimal fringe contrast.

The parameters of equations (4.1.12) were in turn used in equation (4.1.3) to simulate $I_{r\delta}$ when M = 1. The result of this simulation is shown in cross section by the solid line in Figure 31, where for comparison, an idealized simulation (dotted line) of $I_{r\delta}$ when $\rho = a \rightarrow \infty$ (i.e., all fringes are available in the reconstruction) and $\omega_I \rightarrow \infty$ (i.e., infinite uniform plane wave reconstruction beam) is also provided. Note that both curves in Figure 31 have been normalized to unity peak intensity and that the radial width of the idealized simulation at the 1/e point is approximately equal to ω_u. The simulation of Figure 31 can in fact be taken as the PSF of the overall holographic imaging system when the primary limiting factors are the EBSLM resolution ρ (solid line) and the size ω_u of the focused scanning beam (dotted line).

Note that as ρ, a and ω_I approach infinity, it is readily shown, using equations (3.2.8) and (4.1.3), that $I_{r\delta}$ is in fact Gaussian with waist equal to ω_u.

To further investigate the PSF, the full width half maximum (FWHM) of $I_{r\delta}$ was calculated as a function of the number of fringes used in the reconstruction. The results of these calculations are plotted in Figure 32, where the horizontal dotted line indicates the minimum FWHM if all fringes are available in the reconstruction process (i.e., $\rho \rightarrow \infty$) and $\omega_u = 3.526\mu m$ (note that the FWHM of a Gaussian is found by multiplying the waist value by $2\sqrt{\ln(2)}$). The vertical dotted line, on the other hand, indicates the practical limit on the number of fringes available in the reconstruction process based on the manufacturer specified EBSLM resolution [9] of 20 lp/mm, (corresponding to about 22 fringes, or zones, on the hologram). As in the calculation of equations (4.1.12) and (4.1.13), Figure 32 was plotted assuming $M=1$, $f_2 = z = 17.5\,cm$, $\lambda = 633\,nm$, $\omega_u = 3.526\,\mu m$, $\omega_v = 1.0\,cm$ and $\omega_I = 3.0\,cm$. Note that, as expected, the FWHM of the PSF gets smaller as the number of fringes in the reconstruction process increases. Also note that, strictly speaking, Figure 32 gives the FWHM, for unity magnification, of the incoherent PSF as a function of the number of reconstructing fringes, without requiring that the fringes be limited only by the EBSLM resolution. Furthermore, as we will see in the experimental section, a convenient way of measuring the EBSLM resolution is to display a FZP on an EBSLM and measure the number of visible fringes. Once the magnification factor M is determined, equation (4.1.4) can be used to find ρ_{SLM}, the EBSLM resolution.

As we will discuss in some detail in the next section the holographic recording and reconstruction of a simple transmissive slit object, it will be helpful if we now discuss the form of the reconstructed slit image, based on the predicted PSF. Strictly speaking, we see from Figure 31 that as the number of fringes used in the reconstruction process is limited, the PSF is broadened and takes on some side lobes. However, for our purposes it is much easier mathematically and computationally to model the PSF as a Gaussian function with waist $\beta = (FWHM)/2\sqrt{\ln(2)} \simeq 0.6(FWHM)$, where the FWHM is determined from Figure 32 and the

number of reconstruction fringes is known. Modeling the PSF in this manner will, of course, introduce some error in the predicted shape and size of the reconstructed slit, though as we will see in the next section, for the previously described system parameters the Gaussian PSF approximation proves to allow an accurate and convenient estimate of the size of the reconstructed slit image.

Using the Gaussian PSF approximation, the reconstructed slit image I_{rs} is then simply written in normalized form as

$$I_{rs} = \left(rect\left(\frac{x}{\alpha}\right) * \exp\left(-\frac{r^2}{(\beta M)^2} \right) \right) \frac{1}{I_{rs}(0)} \quad , \tag{4.1.14}$$

where

$$rect\left(\frac{x}{\alpha}\right) = \begin{cases} 1; & |x| \le \alpha/2 \\ 0; & elsewhere \end{cases} \quad , \tag{4.1.15}$$

α is the width of the slit, $I_{rs}(0)$ is the (maximum) value of I_{rs} at $r=0$, M accounts for magnification of the PSF after display on the EBSLM and where * now denotes convolution along the x direction. Upon performing the convolution in equation (27) and making the required simplifications, we find in the x-direction that

$$I_{rs}(x) = \left[erf\left(\frac{1}{M\beta}\left(\frac{\alpha}{2} - x\right) \right) + erf\left(\frac{1}{M\beta}\left(\frac{\alpha}{2} + x\right) \right) \right] \frac{1}{I_{rs}(0)} \quad , \tag{4.1.16}$$

where erf(x) is the error function [34] defined as

$$erf(x) = \frac{2}{\sqrt{\pi}} \int_0^x \exp\left(-t^2\right) dt \quad . \tag{4.1.17}$$

Of course, I_{rs} will be uniform in the y-direction. As we will see in the next section, equation (4.1.16) will prove useful in comparing experimental measurements with theoretical predictions, where for simulation purposes it is mentioned that a simplified algebraic expansion of erf(x) can be written as [34]

$$erf(x) = 1 - \left(a_1 t + a_2 t^2 + a_3 t^3\right) \exp\left(-x^2\right) \quad , \tag{4.1.18}$$

where

$$\begin{aligned} t &= \frac{1}{1 + px} \\ p &= 0.47047 \\ a_1 &= 0.3480242 \\ a_2 &= -0.0958798 \\ a_3 &= 0.7478556 \end{aligned} \quad , \tag{4.1.19}$$

4.2 Size Of The Reconstructed Slit: Experimental Verification

Refering to Figure 4, in the following experimental work a narrow transmissive slit object such that $|\Gamma_2|^2 = rect(x/\alpha)$, where $\alpha = 50\mu m$ was scanned. (To aid in visualizing the discussion to follow, we mention that as discussed in section 3.2.3, the scanned hologram of such a narrow slit, when $\omega_v >> \omega_u$ (see equations (3.2.1) and (3.2.3)) and the distance z from the scanner is much larger than the slit width α, qualitatively looks like a truncated one dimensional FZP (see equation (3.1.11)), with true fringe spacing and visibility varying only slightly from that of an ideal FZP (see Figures 8 and 24). This of course, is due to the fact that

a narrow slit in essence approximates a one-dimensional spatial delta function.) The scanned electrical signal representing the hologram of the slit was then sent in synchronism and displayed on a storage oscilloscope as shown in Figure 30. With the ultimate intent of maximizing the diffraction efficiency of the slit hologram in the reconstruction process, and as the location and focal plane of the CCTV was arranged such that its field of vision was completely filled by only the oscilloscope screen, the time/div setting of the oscilloscope was adjusted such that when displayed on the EBSLM, the fringes of the slit hologram were just barely resolvable at the outermost edges of the EBSLM display area. In other words, by proper adjustment of the equipment in Figure 30, when displayed on the EBSLM, the scanned slit hologram filled the display area with fringes, all of which were at least minimally resolvable. Notice also that this procedure ensured that the maximum number of resolvable fringes were displayed on the EBSLM, further increasing the reconstruction diffraction efficiency. Figure 33 shows a photograph of the hologram recorded for the 50 μm slit. This picture was taken with an oscilloscope camera just after the holographic image was stored on the oscilloscope and just before the CCTV camera was used to send the corresponding hologram video signal to the EBSLM controller.

Notice the nonuniformity of the fringes in Figure 33. This is primarily due to phase noise introduced by scanner vibration into the Mach-Zhender interferometer type configuration shown in Figure 4. As we will see, this, as well as other factors, will limit the resolution of reconstructed images. Notice also the binary nature of the hologram of Figure 33 - that is, no smoothly varying brightness between fringes, as would be expected. This is due to the facts that only above a certain minimum threshold voltage does the oscilloscope provide appreciable intensity modulation of the displayed signal and that beyond the threshold voltage, only minimal increases in modulation intensity are possible except for very large z-axis input voltage levels. It is thus primarily due to the fact that the oscilloscope limits us to only two gray levels that we are able to only investigate holograms of very simple objects, such as narrow slits, where the fringe amplitudes are mostly uniform. Furthermore, in addition

to the fact that the finite spatial resolution limits the complexity of objects whose holograms are suitable for display on the EBSLM, the EBSLM also limits the complexity of holographic objects due to its limited number of grey-levels (the manufacturer predicts $\leq$ 10 grey levels in the EBSLM [9]).

In order to predict the size of the slit image after reconstruction, we must determine the magnification factor M_{SLM} resulting from displaying the hologram of Figure 33 on the EBSLM. This is accomplished by modeling, for simplicity, the slit hologram I_{hs} as a scaled one dimensional FZP, written as (see equation (3.1.11))

$$I_{hs} \simeq 1 + \cos\left(\frac{\pi}{\lambda z} \left(\frac{x}{M_{SLM}} \right)^2 \right) \quad . \tag{4.2.1}$$

M_{SLM} is then determined by measuring the location x_n of the nth maxima, or fringe, when the hologram is viewed on a screen placed after the analyzer shown in Figure 29. Analytically, M_{SLM} is given as

$$M_{SLM} = \frac{x_n}{\sqrt{2n\lambda z}} \ , \ n = 1,2,3... \tag{4.2.2}$$

where the central fringe (n=0) provides no useful information. By measuring the location of the first 10 fringes as just described, it was thus found that on average $M_{SLM} \simeq 2.574$. Furthermore, as in Figure 33, it was observed that as many as 20 fringes or fringe fragments were displayed on the EBSLM; the fragmentation of the higher order fringes, we feel, being primarily a result of the intermediate display process. (That is, as seen in Figure 8, due to the Gaussian nature of the scanning beams, the voltage signal v(x,y;z) of equation (3.1.11) is in effect pre-multiplied by a broad Gaussian apodization, thus reducing the amplitude of the signal corresponding to the higher order fringes to near the threshold level needed to clearly display them on the oscilloscope.) Using the average value for M_{SLM}, and assuming that the EBSLM resolution limits us to 20 visible fringes, equation (4.1.11) was used to determine that

the spatial resolution of the EBSLM was approximately $\rho_{SLM} \simeq 7.4\, lp/mm$, where for this calculation $\mathrm{Im}\{1/G\}$ is given as in equation (4.1.12). Notice that this value for ρ_{SLM} is slightly larger than the measured EBSLM resolution range mentioned in section 4.1.1. It is believed that this new value for the EBSLM resolution is more representative of the EBSLM performance and that the lower, previously presented EBSLM resolution values can be attributed to our initial observation of the EBSLM output on a smoked glass viewing screen - itself a mildly distorting medium.

Notice now that M_{SLM} represents the lateral magnification of the slit hologram displayed on the EBSLM, as well as the magnification of the reconstructed image. Recalling the well known result [28] of equation (3.2.31) when the holographic recording and reconstruction wavelengths are the same (i.e., $M_{long} = M_{lat}^2$), we see that the expected distance from the analyzer to the reconstruction plane is

$$z\, M_{long} = z\, M_{lat}^2 = z\, M_{SLM}^2 = 116.0\, cm \quad , \tag{4.2.3}$$

where the initial scanning distance was $z = 17.5$ cm and M_{SLM} is given above. In order to magnify the reconstructed image to a more manageable size, within a distance from the hologram plane comparable to that expressed in equation (4.2.3), the configuration shown in Figure 33 was used when reconstructing the real image of the slit object.

In Figure 34 we see that a long focal length lens ℓ_1 is placed against the analyzer of Figure 29. This in effect increases the curvature of the light emerging from the analyzer (i.e., the effective hologram plane), and causes the reconstructed image to occur at a shorter distance f' from the hologram. A short focal length lens ℓ_m is then used to magnify the reconstructed image to a measurable size, after which the magnified real image is recorded on film. In order to then determine the overall magnification of the reconstructed real image, we begin by writing the wave emerging from lens ℓ_1, in complex form, as

$$\Psi_{\ell 1} = \exp\left(-j\frac{\pi}{\lambda z}\left\{\frac{x}{M_{SLM}}\right\}^2\right)\exp\left(-j\frac{\pi}{\lambda f_1}x^2\right) \quad , \tag{4.2.4}$$

where $\Psi_{\ell 1}$ represents the complex amplitude of the wave emerging from lens ℓ_1, f_1 is the focal length of lens ℓ_1 and the first and second exponential terms of equation (4.2.4) represent, respectively, the approximate complex representation of the slit hologram (i.e., the on-axis, magnified version of $\tilde{V}_\delta$ given in equation (3.1.8)) and the complex phase transformation of a thin lens in the x-direction [28]. Combining the arguments of the exponentials in equation (4.2.4) we find that

$$\Psi_{\ell 1} = \exp\left(-j\frac{\pi}{\lambda f'}x^2\right) \quad , \tag{4.2.5}$$

where

$$f' = z\frac{M_{SLM}^2 f_1}{z M_{SLM}^2 + f_1} = z M'_{long} \tag{4.3.6}$$

and M'_{long} is now the effective longitudinal magnification of the reconstructed real image. The overall lateral magnification of the real slit image in the film plane is then

$$M_{tot} = M_{\ell m}\sqrt{M'_{long}} = M_{\ell m}\frac{M_{SLM}^2 f_1}{z M_{SLM}^2 + f_1} \quad , \tag{4.2.7}$$

where $M_{\ell m} = i/o$ is the magnification due to the imaging lens ℓ_m.

For this work $f_1 \simeq 1.0m$, z = 17.5 cm and $M_{SLM} \simeq 2.574$, indicating $f' \simeq 53.7cm$ (as opposed to the measured value $f' = 53.1cm$, the difference from the predicted value of being primarily due to the imprecise value of f_1 and a slight displacement of lens ℓ_1 from the analyzer in Figure 34). Using a lens of focal length $f_m \simeq 6.9cm$, we adjusted lens ℓ_m so that o = 7.6 cm and i = 74.1

cm, yielding $M_{\ell m} = 9.75$. Using the measured value of f', the total lateral magnification of the reconstructed real slit image was thus

$$M_{tot} = M_{\ell m}\sqrt{\frac{f'_{meas}}{z}} = 16.82 \quad . \tag{4.2.8}$$

Using $M = M_{tot}$ in equation (4.1.16) where in the same equation the PSF width β is determined using Figure 32, for a PSF with 20 fringes (recall that a slit hologram approximates a FZP), to be $\beta = 0.6(28.0\mu m) = 16.8\mu m$, we can find the expected shape of the reconstructed real slit image. A plot of equation (4.1.16) when $\alpha = 50\mu m$, $\beta = 16.8\mu m$ and M=16.82 is shown in Figure 35. We see that the overall width of the reconstructed real slit image is roughly expected to be 1.1 mm.

Figure 36a shows the results of a real-time reconstruction of the slit image. As measured directly on the film, the bright central line, corresponding to the reconstructed image is approximately 0.9 mm wide. (It should be mentioned that by "real-time" an ability to capture object motion is not implied - though in future work this may be possible. In the context of this work, therefore, we will take "real-time" holography to imply that a single, static hologram is recorded and reconstructed in quick succession. The time lapse till the reconstructed image is produced is essentially limited only by how fast the object is scanned and by how quickly the operator can then press the write switch on the EBSLM controller. This process is, of course, aided by the fact that no intermediate photoprocessing is necessary and that only electronic signal processing is required to produce the holographic image in the EBSLM.)

For comparison purposes, a silver positive transparency of the polaroid photograph of Figure 33 was produced, where through photographic reduction the width of the reduced hologram was made to be 1.2 mm (the diameter of the EBSLM crystal) in the dimension perpendicular to the fringe information. This ensured that magnification of the hologram transparency was about the same as that originally encountered when the slit hologram was

displayed on the EBSLM. The magnification in the dimension parallel to the fringe information is, of course, less critical and was not the same as the value in the real-time reconstruction. The hologram transparency was then reconstructed using conventional coherent techniques by placing it in front of lens ℓ_1 in Figure 34 and then illuminating it coherently. The resulting reconstructed real slit image is shown in Figure 36b, where the central line was measured on the recording film to be approximately 1.0 mm wide.

Note the similarity of Figures 36a and 36b. This would indicate that, at least for simple objects, the EBSLM does not introduce excess distortion into the reconstructed image, though as previously discussed, for more complicated objects, the grainesess of the SLM due to finite resolution and the limited gray levels will likely introduce some level of distortion. The nonuniformity of the central line in Figures 36a and 36b then is believed primarily to be due to the previously discussed phase noise introduced by the scanner. As mentioned in chapter 3, in future work we hope to eliminate this phase/vibrational noise by incorporating well known fiber optic technology into the interferometer of Figure 4 [30,31]. Physically isolating the mechanical scanner from the rest of the set-up in Figure 4, or the incorporation of acousto-optic scanners, will also aid in reducing vibrational noise.

Other background noise seen in Figures 34a and 34b are likely due to several factors. For instance, numerous unexpected vertical and horizontal fringes are observed other than the bright central line. These extraneous fringes are in part due to the fact that the hologram of Figure 33 is essentially illuminated through a rectangular aperture. That is the recorded slit hologram is finite in both the x and y dimensions. Furthermore, since the actual PSF has sidelobes, for finite EBSLM spatial resolution, we expect some background fringe information in the reconstructed image parallel to the central maximum. To a lesser extent, as Figures 36a and 36b represent the reconstruction of on-axis holograms, some extraneous noise due to the virtual (twin) image and throughput light may be present.

Finally, note that the sizes (0.9 mm using the real-time approach and 1.0 mm using coherent read out methods) of the reconstucted images of Figures 36a and 36b are somewhat

smaller than the predicted size of 1.1 mm due primary to the fact that it can be shown [5] that the fringe spacing for a narrow slit hologram is a bit wider than for an ideal FZP. Thus M_{SLM} is probably less than estimated by measuring the fringes in the slit hologram, indicating our prediction of 1.1 mm is probably an over estimate.

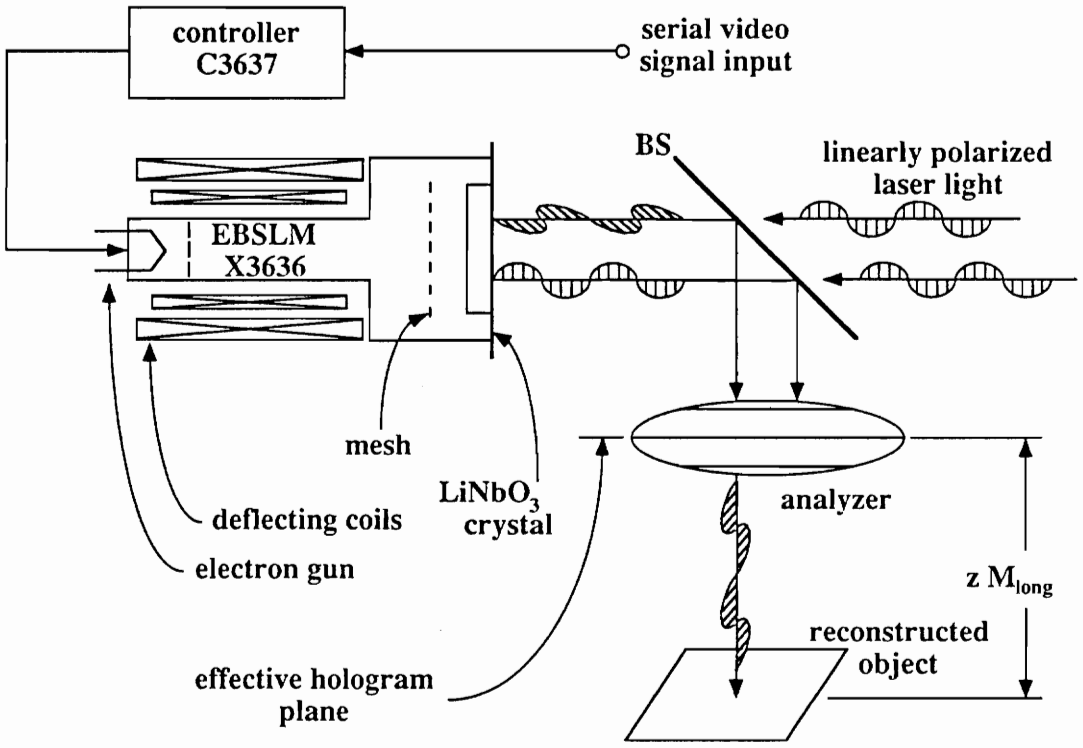

Figure 29. Schematic diagram of the EBSLM: (electron beam addressed spatial light modulator) [4].

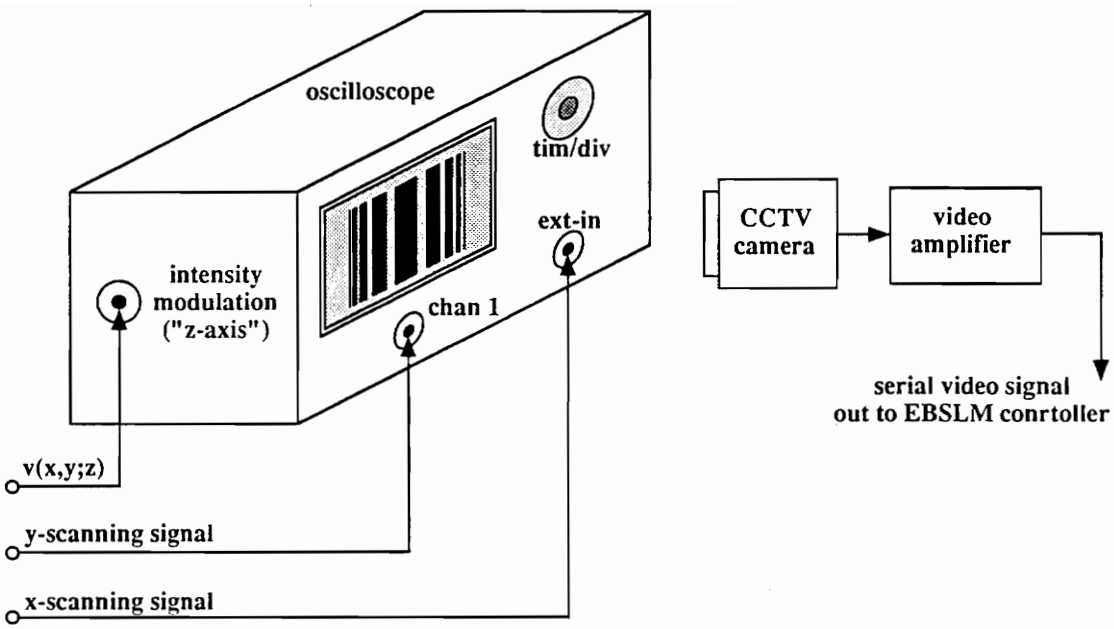

Figure 30. Intermediate display technique: (used to convert slowly scanned holographic data into a corresponding standard video image).

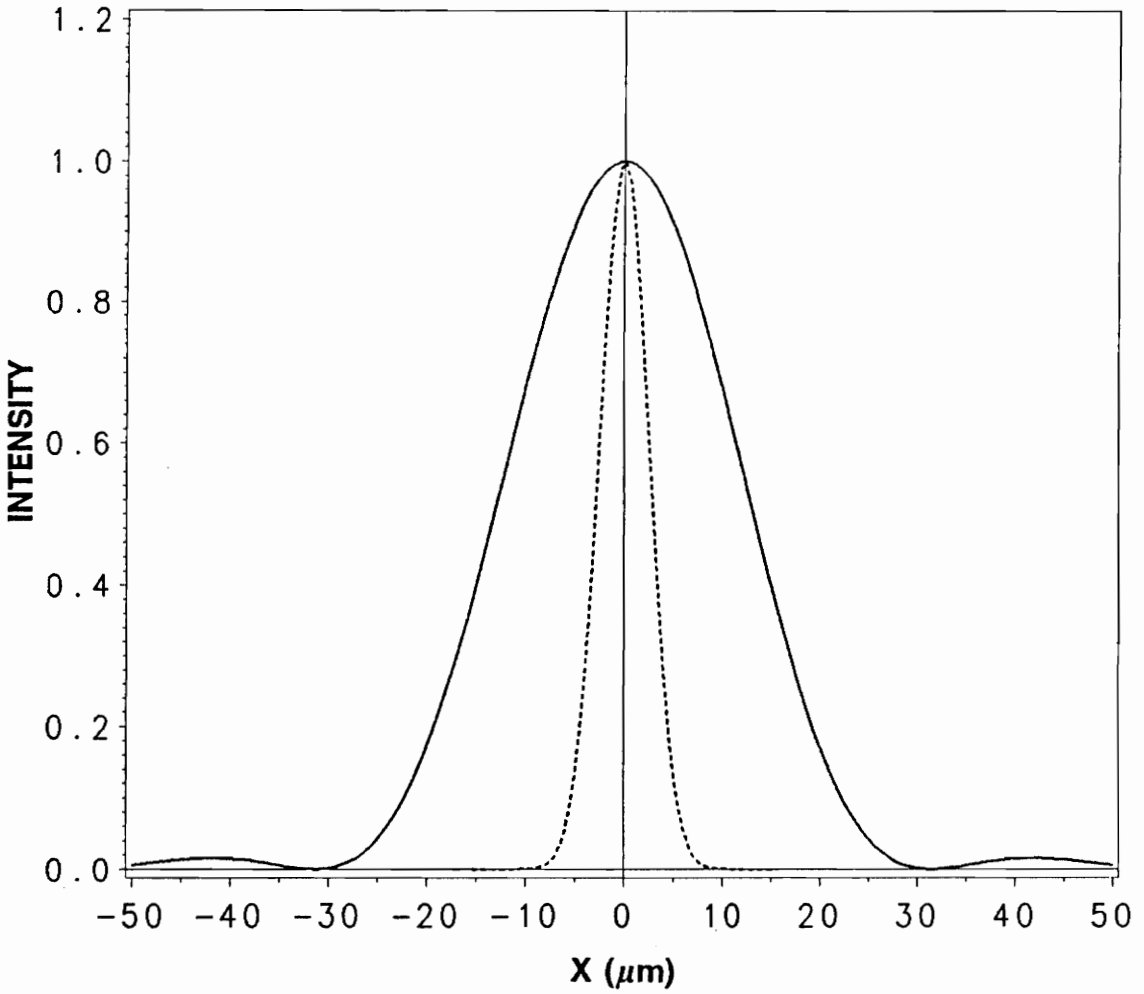

Figure 31. Point spread function of the holographic system: (when the maximum expected EBSLM spatial resolution limit of 20 lp/mm (solid line) and the focused scanning beam size (dotted line) are the primary factors contributing to PSF broadening).

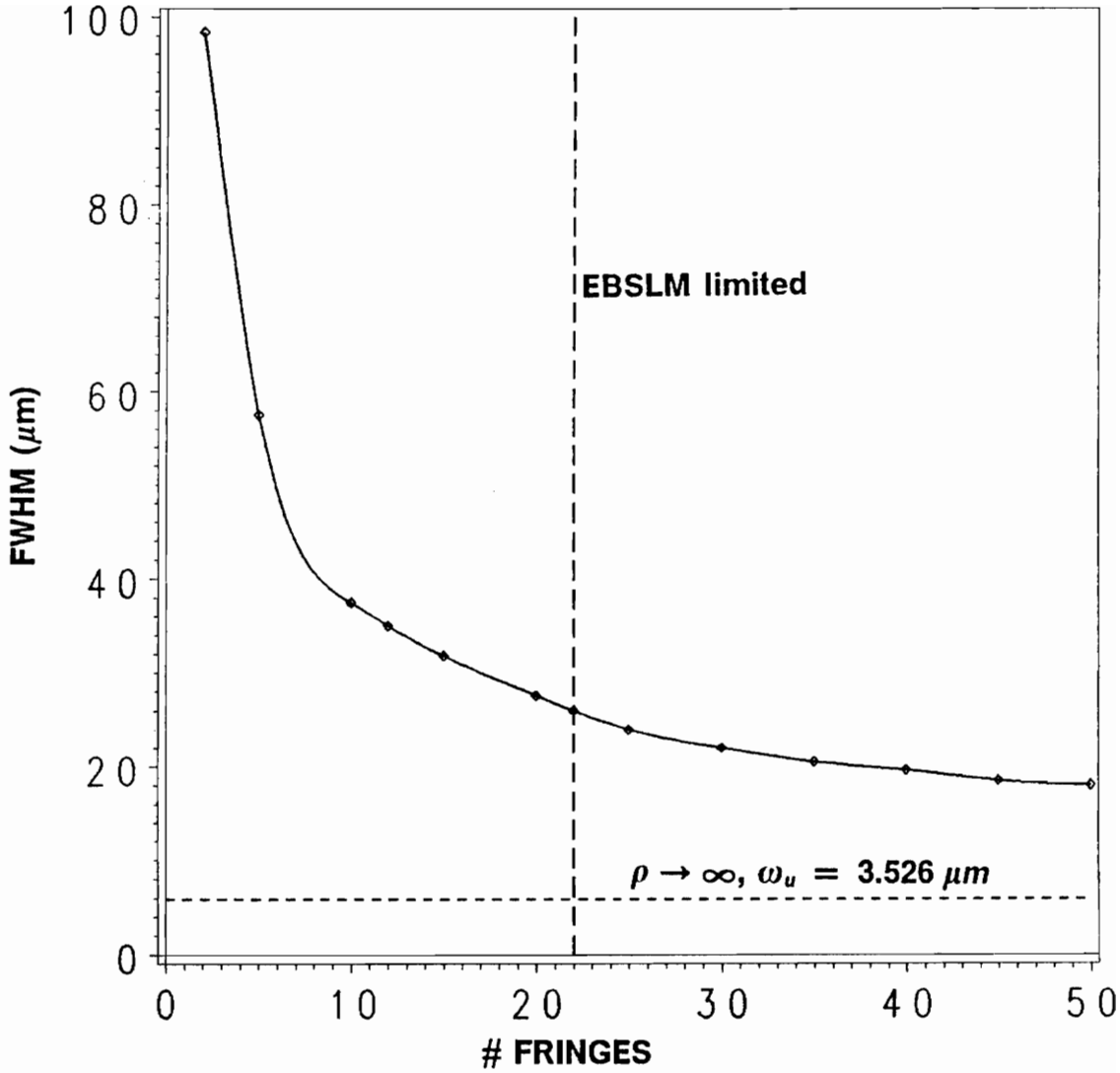

Figure 32. FWHM of the overall PSF: (as a function of the number of fringes used in the reconstruction process).

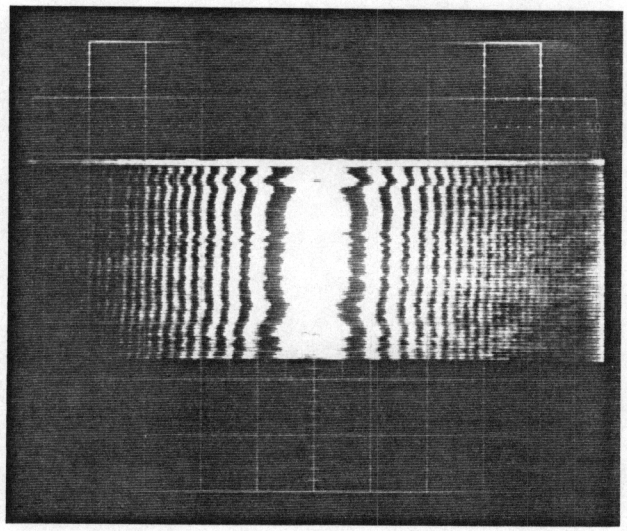

Figure 33. Hologram recorded for a 50 micrometer slit.

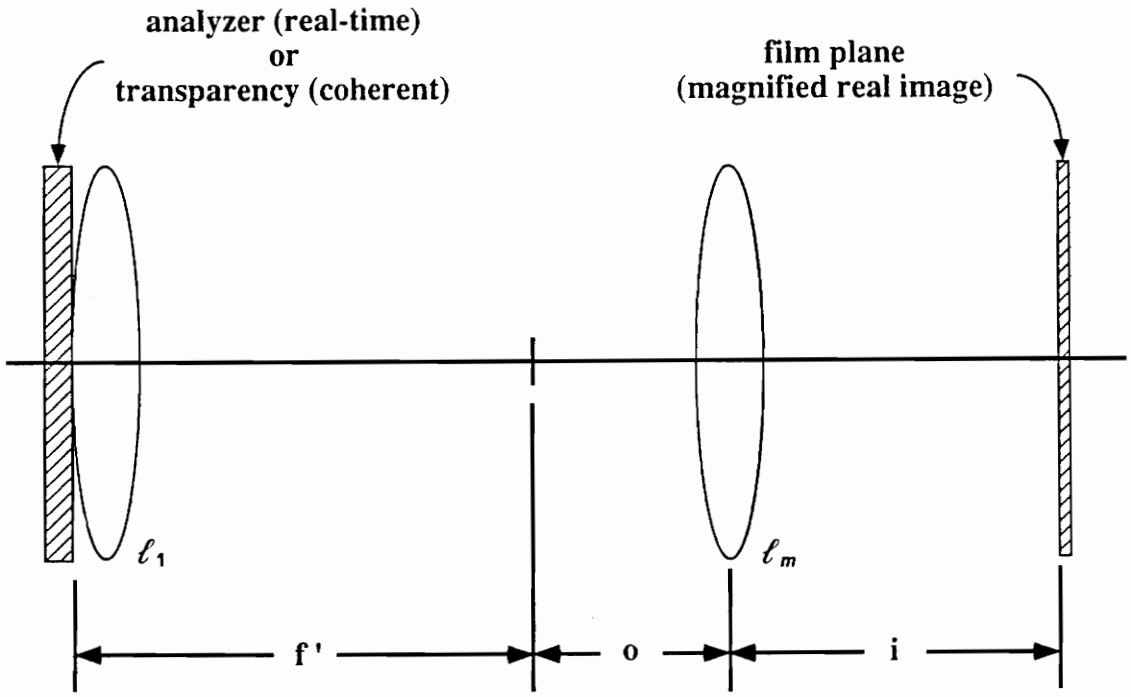

Figure 34. Lens configuration used in the reconstruction process: (implemented to reduce the distance from the hologram at which the real image is viewed).

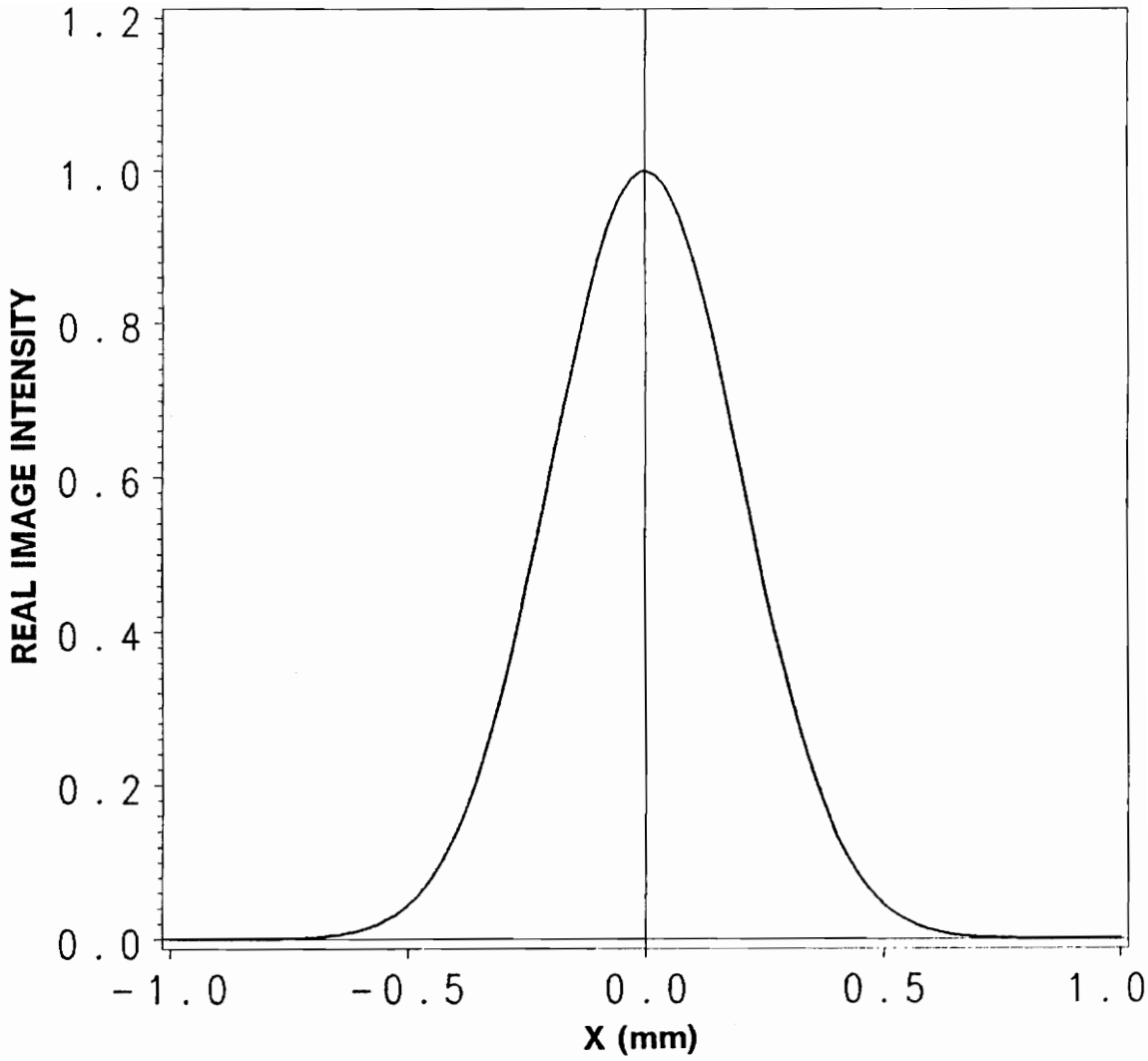

Figure 35. Simulation of the reconstructed slit image: (simulation based on a Gaussian PSF approximation).

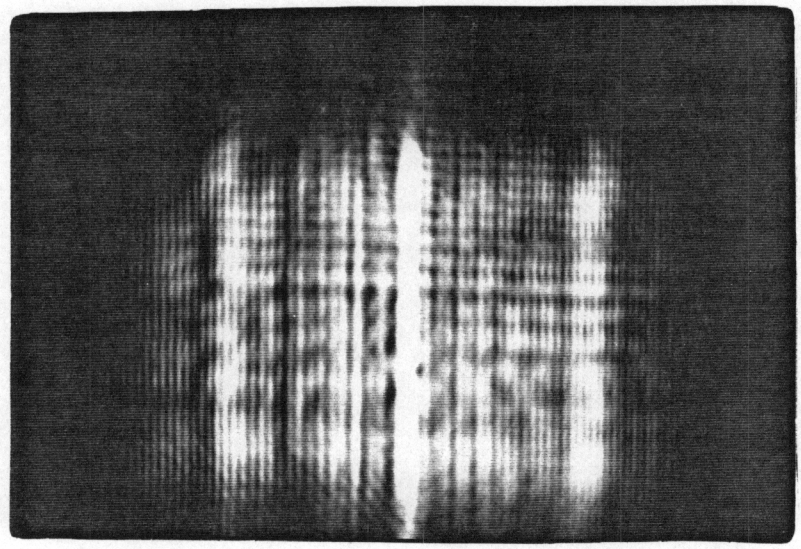

(a)

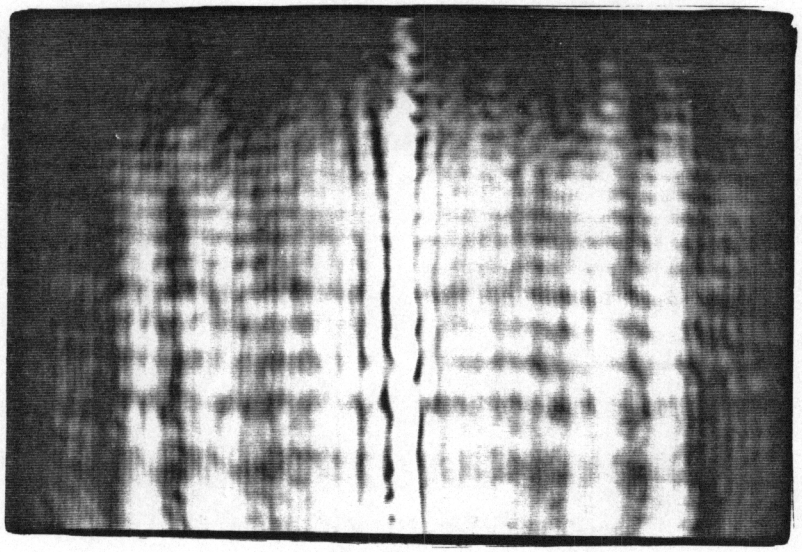

(b)

Figure 36. Reconstructed real slit images: produced; a) in real-time and, b) by coherent methods.

5.0 CONCLUSION

We have seen a detailed description, both theoretically and experimentally, of the principles and applications of scanning holography in the optical regime. In addition, the advantages which this method posesses over conventional incoherent holographic techniques have been presented. Specifically, the method is capable of producing carrier frequency holograms of three dimensional objects. The technique also allows the active and selective adjustment of background bias buildup for increased fringe contrast and suggests a practical method for the reduction of the information content to be recorded holographically.

In addition, a theoretical analysis and the first experimental results for determining the appropriateness of using an electron beam addressed spatial light modulator as a real-time holographic display device have been provided. Also investigated was the size and shape of the point spread function for the overall active optical scanning holographic imaging system based on both the EBSLM resolution and the number of fringes used in the reconstruction process. Furthermore, real-time holography using an EBSLM in conjunction with the scanning holographic recording technique was performed and the results were found to be consistent with corresponding coherent reconstruction methods. The spatial resolution of the EBSLM was also investigated.

Our findings indicate that indeed the EBSLM affords the advantage of coherent real-time display of holographic images. This is possible since the holographic information recorded by the heterodyne scanning technique manifests itself as a modulated electrical signal. Thus, all processing of the scanned holographic information is electronic, eliminating the need for time consuming photographic processing. However, due primarily to low spatial resolution (about 7.4 lp/mm), only holograms of simple objects are suitable for display and subsequent reconstruction using the EBSLM. This limitation is further compounded by the fact that scanned holographic data does not usually conform to video standards, thus requiring that intermediate display techniques employing a storage oscilloscope be used, which in turn reduce the number of available grey levels in the displayed hologram to approximately two. These limitations will likely be alleviated to some degree by eliminating the intermediate display steps and by providing a direct, electronic interface between the scanned data and the EBSLM controller. In fact, continuing work on this project is presently centered on designing such an electronic interface while also investigating techniques for stabilizing the interferometer configuration of Figure 3 using fiber optic technology. Advances in these areas should allow holograms of more elaborate objects can be recorded and studied.

Finally, it should be mentioned that among the potential applications of the scanning holographic technique is the generation of holograms of large scale objects, without the need for large optical elements, for example. Other potential applications could include holographic microscopy, particle sizing and velocimetry.

5.1 Present Research Directions and Goals

1. Development of a fiber optic based acousto-optic modulator [30] for implementation in the two-pupil scanning image processor of Figure 4.

2. Incorporation of fiber-optic technology [31] into the two-pupil scanning image processor as a means of actively eliminating distortion in recorded holograms due to spurious external disturbances.

3. Direct electronic synchronization of the scanned holographic signal and the EBSLM so that the intermediate display process discussed in section 4.1.1 may be eliminated.

4. Determination of the bandwidth requirements for a medium (e.g.: free space, optical fiber or coaxial cable) over which scanned holographic information is transmitted, in terms of: a) the scanned object's spatial information content, b) the x and y scanning frequencies of the heterodyne scanning image processor, and c) the temporal carrier frequency f_o shown in Figure 4.

5. The investigation of alternate pupil functions U_1 and V_1 such that the defocused two-pupil scanning image processing technique can be used to perform image processing functions in addition to the generation of optical holograms.

5.2 Summary of Original Contributions

1. Experimentally verified the principles of scanning holography in the optical regime first proposed by Poon [4] in 1985.

2. Extended Poon's original theory to include a Gaussian beam analysis (a practical consideration) and as a result, described the longitudinal distortion introduced into a reconstructed object when the holographic magnification is other than unity - a result not evident without performing the Gaussian beam analysis.

3. Described a method of actively reducing the bias buildup encountered in conventional incoherent holography.

4. Demonstrated a method of reducing the recorded holographic information content (an important consideration for displaying holographic information on practical spatial light modulators).

5. Demonstrated, for the first time, the real-time reconstruction of optically scanned holograms using the first commercially available (outside of Japan) prototype of a room temperature operated EBSLM.

5. Described a convenient method of generating carrier frequency holograms of incoherent 3-D surfaces.

REFERENCES

References set in **bold** face type indicate articles written in conjuction with the preparation of this dissertation which have either been published or submitted for publication.

1. R.K. Mueller: "Acoustic Holography," Proc. IEEE, Vol. 59, No. 9, pp. 1319-1334, September 1971.

2. N.H. Farhat and W.R. Guard: "Millimeter Wave Holographic Imaging of Concealed Weapons," Proc. IEEE, pp. 1383-1385, September 1971.

3. R.W. Larson, J.S. Zelenka and E.L. Johansen: "A Microwave Hologram Radar System," IEEE Transactions of Aerospace and Electronic Systems, Vol. AES-8, No. 2, pp. 202-217, March 1972.

4. T.-C. Poon: "Scanning Holography and Two-Dimensional Image Processing by Acousto-Optic Two-Pupil Synthesis," J. Opt. Soc. Am. A, Vol. 2, No. 4, pp. 521-527, April 1985.

5. **B.D. Duncan and T.-C. Poon: "Gaussian Beam Analysis of Optical Scanning Holography," (Submitted to) J. Opt. Soc. Am. A.**

6. A.W. Lohmann and W.T. Rhodes: "Two-Pupil Synthesis of Optical Transfer Functions," Applied Optics, Vol. 17, No. 7, pp. 1141-1151, 1 April 1978.

7. T.-C. Poon and A. Korpel: "Optical Transfer Function of an Acousto-Optic Heterodyning Image Processor," Optics Letters, Vol. 4, pp. 317-319, 1979.

8. **T.-C. Poon, B.D. Duncan, M.H. Wu, K. Shinoda and Y. Suzuki: "Real-Time Optical Holography Using a Spatial Light Modulator," Japanese Journal of Applied Physics, Vol. 29, No. 10, pp. L1840-L1842, October 1990.**

9. Product information sheet for EBSLM model X3636, provided by Hamamatsu Photonics K.K., Japan, and Hamamatsu Corp., Bridgewater, NJ, 1989.

10. **B.D. Duncan, T.-C. Poon, M.H. Wu, K. Shinoda and Y. Suzuki: "Real-Time Reconstruction of Scanned Optical Holograms Using an Electron Beam Addressed Spatial Light Modulator," (submitted to) Journal of Modern Optics.**

11. L. Mertz and N.O. Young: Proceedings of the ICO Conference on Optical Instruments, Chapman and Hall, London, p.305, 1961.

12. G.W. Stroke and R.C. Restrick III: "Holography with Spatially Noncoherent Light," Applied Physics Letters, Vol. 7, No. 9, pp. 229-231, 1 Novemver 1965.

13. A.W. Lohmann: "Wavefront Reconstruction for Incoherent Objects," Journal of the Optical Society of America, Vol. 55, pp. 1555-1556, November 1965.

14. H.R. Worthington, Jr.: "Production of Holograms with Incoherent Illumination," Journal of the Optical Society of America, Vol. 56, No. 10, pp. 1397-1398, October 1966.

15. G. Cochran: "New Method of Making Fresnel Transforms with Incoherent Light," Journal of the Optical Society of America, Vol. 56, /no. 11, pp. 1513-1517, November 1966.

16. A. Kozma and N. Massey: "Bias Level Reduction of Incoherent Holograms," Applied Optics, Vol. 8, No.2, pp. 393-397, February 1969.

17. C.B. Burckhardt and E.T. Doherty: "Formation of Carrier Frequency Holograms with an On-Axis Reference Beam," Applied Optics, Vol. 7, No. 6, pp. 1191-1192, June 1968.

18. W. Lukosz: "Properties of Linear Low-Pass Filters for Nonnegative Signals," J. Opt. Soc. Am., Vol. 52, pp. 827-829, 1962.

19. D. Goerlitz and F. Lanzl: "Methods of Zero-Order Non-Coherent Filtering," Opt. Comm., Vol. 20, pp. 68-72, 1977.

20. A.W. Lohmann: "Incoherent Optical Processing of Complex Data," Applied Optics, Vol. 16, pp. 261-263, 1977.

21. W. Stoner: "Incoherent Optical P Via Spatially Offset Pupil Masks," Applied Optics, Vol. 17, pp. 2454-2466., 1978.

22. W.T. Rhodes: "Bipolar Pointspread Function Synthesis by Phase Switching," Applied Optics, Vol. 16, pp. 265-267, 1977.

23. L.H. Lin: "A Method of Hologram Information Reduction by Spatial Frequency Sampling," Applied Optics, Vol. 7, No. 3, pp. 545-548, 1968.

24. L.H. Enloe, W.C. Jakes and C.B. Rubinstein: "Hologram Heterodyne Scanners," Bell Sys. Tech. J., pp. 1876-1872, 1968.

25. J.W. Goodman: *Introduction to Fourier Optics*, McGraw-Hill, New York, 1968.

26. T.-C. Poon: "Method of Two-Dimensional Bipolar Incoherent Image Processing by Acousto-Optic Two-Pupil Synthesis," Optics Letters, Vol. 10, No. 5, pp. 197-199, 1985.

27. T.-C.Poon, J. Park, and G. Indebetouw: "Optical Realization of Textural Edge Extraction," Opt. Comm., Vol. 65, No. 1, pp. 1-6, 1988.

28. P.P. Banerjee and T.-C. Poon: *Principles of Applied Optics*, Aksen Associates, Boston, MA, 1991.

29. F.T.S. Yu: *Optical Information Processing*, John Wiley & Sons, New York, NY, 1983.

30. B.Y. Kim, J.N. Blake, H.E. Engan, and H.J. Shaw: "All-Fiber Acousto-Optic Frequency Shifter," Optics Letters, Vol. 11, No. 6, pp. 389-391, June 1986.

31. D.A. Jackson, R.G. Priest, A. Dandridge and A.B. Tveten: "Elimination of Drift in a Single-Mode Optical Fiber Interferometer Using a Piezoelectrically Stretched Coiled Fiber," Applied Optics,

32. K. Shinoda and Y. Suzuki: "Electron Beam Addressed Spatial Light Modulator," SPIE Vol. 613 *Nonlinear Optics and Applications*, pp. 158-164, 1986.

33. T.-C. Poon: " Optical Heterodyne Scanning Holography," paper Thdd6, 1989 OSA Annual Meeting.

34. *Handbook of Mathematical Functions,* M. Abramowitz and I. Stegun (eds.), Dover Publications, New York, 1970.

Vita

Bradley D. Duncan was born in Bristol, Tennessee, on June 4, 1963 and attended Abingdon High School in Abingdon, Virginia. He received the B.S., M.S. and Ph.D degrees in Electrical Engineering From Virginia Polytechnic Institute and State University in June (1986), May (1988), and June (1991), respectively. His research interests include holography, scanning and non-linear image processing, waveguide analysis, fiber optic sensor techniques and optical fiber sensor system design.

Mr. Duncan is a member of the IEEE Lasers and Electro-Optics Society and the Optical Society of America. His personal interests include scuba diving, motorcycling, camping, hiking and other outdoor activities as well as involvement in community service projects.